Block Copolymer Self-assembly and Templating Strategies

By

Wubin Bai

B.S., Physics (2011)
University of Science and Technology of China

Submitted to the Department of Materials Science and Engineering in
Partial Fulfillment of the Requirement for the Degree of

Doctor of Philosophy in Materials Science and Engineering

at the
Massachusetts Institute of Technology

June 2016

Signature of Author……………………………………………………………………………...
Department of Materials Science and Engineering
May 2, 2016

Certified by……………………………………………………………………………………….
Caroline A. Ross
Professor of Materials Science and Engineering
Thesis Supervisor

Accepted by………………………………………………………………………………………
Donald Sadoway
Professor of Materials Chemistry
Chair, Department Committee on Graduate Student

Block Copolymer Self-assembly and Templating Strategies

By

Wubin Bai

Submitted to the Department of Materials Science and Engineering on
May 2, 2016 in Partial Fulfillment of the Requirement for the Degree of
Doctor of Philosophy in Materials Science and Engineering

Abstract

Block copolymers microphase separate to form periodic patterns with period of a few nm and above without the need for lithographic guidance. These self-assembled nanostructures have a variety of bulk geometries (alternating lamellae, gyroids, cylinder or sphere arrays, tiling patterns, core-shell structures) depending on the molecular architecture of the polymer and the volume fraction of its blocks. And in thin films, surface interaction and commensurability effect influence the self-assembly and result in more diverse morphologies including hexagonal-packed perforated lamellae, square array of holes. The progress of self-assembly can be tracked in situ using Grazing Incidence Small Angle X-ray Scattering, and the annealed morphology can be revealed in 3D using TEM tomography.

Moreover, non-bulk morphologies can be produced, the ordering of the microdomains can be improved and their locations directed using various templates and processing strategies. The blocks can themselves constitute a functional material, such as a photonic crystal, or they can be used as a mask to pattern other functional materials, functionalized directly by various chemical approaches, or used as a scaffold to assemble nanoparticles or other nanostructures. Block copolymers therefore offer tremendous flexibility in creating nanostructured materials with a range of applications in microelectronics, photovoltaics, filtration membranes and other devices.

Thesis Supervisor: Caroline A. Ross

Title: Professor of Materials Science and Engineering

TABLE OF CONTENTS

6 Conclusions and Future Works

LIST OF FIGURES

1. Introduction

2. Functional nanostructured materials based on self-assembly of block copolymers

3. Thin Film Morphologies of Bulk-Gyroid Polystyrene-block-Polydimethylsiloxane under Solvent Vapor Annealing

4. In Situ Characterization of the Self-assembly of a Polystyrene-Polydimethylsiloxane Block Copolymer during Solvent Vapor Annealing

5. Perpendicular Block Copolymer Microdomains in High Aspect-Ratio Templates

Acknowledgement

Thank you, our mentor Professor Caroline Ross for allowing me to be part of the journey with you. Your vision and inspiration make me excited about what I am doing everyday. You made every challenge in this journey a joyful adventure and a great opportunity for your students to grow. You introduced me to the wonderful community and gave me the chance to work with world-class researchers. I love doing research but I never thought I could be doing research at MIT and learning important life skills by doing or by trying. I am grateful for every interaction with teachers, labmates, collaborators, classmates, teammates, and friends both inside and outside MIT.

I would like to express my thankfulness to my other two thesis committees Professor Alfredo Alexander-Katz and Professor Niels Holten-Andersen, who have been supporting and guiding me in my PhD study. Thank you very much for opening the opportunity for collaborations, discussion in research ideas, and sharing the passion and wisdom about science and life! I truly appreciate the collaborations with Dr. Kevin Yager at Brookhaven National Lab, who hosted my every single visit to the synchrotron, one of the world most powerful research facilities. Your sharp mind and strong enthusiasm in science inspire me in designing experiments and solving challenging problems.

Thank you, all the members in Professor Caroline Ross's group, for making Ross group such dynamic, collaborative and friendly place to explore interesting scientific questions. Karim Aissou, Kevin Gotrik, Adam Hannon, thank you for sharing your research experience and teaching me techniques and skills when I just joined the group. Karim Raafat Gadelrab, Christine Kathrein, Hyung Wan Do, Li-Chen Cheng, Kun-Hua Tu, Saman Safari Dinachali, Yi Ding, Thomas Lam, Hong Kyoon Choi, Jinshuo Zhang, Keehong Lee, Melissa Kreider, Nicolas Aimon, Dong Hun Kim, Astera Tang, Shuchi Ojha, Chen Zhang, Enno Lage, Pin Ho, Andy Quindeau, Eduardo Martin, Shuai Ning, I feel fortunate to have chance standing with you shoulder to shoulder. Thank you for bringing your incredible talents and maximum efforts into the projects and events organizing. Tim Savas, James Daley, Mark Mondol, Charlie Settens, Kurt Broderick, Patrick Boisvert, Shiahn Chen, Yong Zhang, Charlotte Stewart-Sloan, Mike Tarkanian, Ike Feitler, Alan Schwartzman, and Geetha Berera, thank you for giving me research facility trainings and helping me get through challenges. Thank you, Gabrielle, for your heartwarming care and tremendous help on our life and research.

It is my privilege to collaborate with famous pioneers from different fields. Professor Apostolos Avgeropoulos, George Liontos , Konstantinos Ntetsikas from University of Ioannina, Greece, Professor Ian Manners, Jessica Gwyther from University of Bristol, UK, thank you for keeping providing new synthesized materials for us to explore. Professor Alexander Böker, Dr. Larisa Tsarkova from RWTH Aachen University, Germany, Dr. J. Alexander Liddle from NIST, Professor

Karl Berggren from EECS MIT, Dr. Charles Black from BNL, Professor Carl Thompson, thank you for putting tremendous efforts in exploring new ideas and raising our work to a higher level. And I also would like to thank my undergrad advisor, Professor Tzay-Ming Hong, and Professor Shih-Lin Chang, who give me guidance, support and encouragement in my career development.

I love you my family. Mom and dad, thank you for everything you do for your boy, thank you for supporting me with unconditional love and care. You let me do what I do and always encourage me to be better. You always set a great example for me in my career and my life. Xiaochen, thank you for always being there for me. The time with you is and will always be the best moments of my life.

Wubin Bai

Chapter 1
Introduction

1.1 Overview and Contents

Synthesis of the nanoscale architectures with controlled chemical composition is essential in nanotechnology.[1] Integrated fabrication is moving towards devices with more computational power for less energy consumption.[2] Memory storage media is not only focusing on scaling down but also the design of device architecture, physical mechanism, and novel materials.[3–5] Micro/Nanoelectromechanical systems (MEMS or NEMS), and Biosensors require nanostructures with desired mechanical or biological properties.[6,7] Battery cells, photovoltaics, photonic crystals and filtration membranes also demand 3-dimensional nanostructures with controlled chemistry.[8,9] Nanostructure fabrication strategies therefore need to become more diverse to fit these different technologies.[10,11] Among those fabrication routes, block copolymer (BCP) self-assembly can form periodic nanostructures spontaneously with low cost and high efficiency,[12,13] and directed self-assembly of BCPs can produce device-oriented nanostructures with feature size from a few nanometers to hundreds of nm.[14]

This thesis focuses on fundamental understanding of the BCP self-assembly behavior and exploring templating strategies in order to fabricate device-oriented nanostructures. Chapter 1 briefly introduces thermodynamics of block copolymer and several nanofabrication techniques that are widely used. Chapter 2 generally reviews block copolymer self-assembly and its use for fabrication of functional nanostructures. Chapter 3 focuses on a Si-containing BCP thin film self-assembly using solvent vapor annealing and using it for pattern transfer into other functional materials such as metals. Chapter 4 discusses an in situ observation of the solvent vapor annealing and structural orientation control associated with annealing process. Chapter 5 shows the templating strategies in order to fabricate device-oriented nanostructure. Chapter 6 concludes the thesis and suggests future works.

1.2 Block Copolymer Thermodynamics

Block copolymers are macromolecules in which two or more chemically distinct repeat units are joined together in covalent bond. For example, a polystyrene-*block*-polymethylmethacylate (PS-*b*-PMMA) BCP consists of a PS chain covalently bonded to a PMMA chain. If the blocks are immiscible, the BCP can self assemble into periodic nanostructures with dimensions ranging from a few nm to several 100 nm.[13,15–21] The microphase-separated structure consists of "microdomains" of each block whose geometry depends on the volume fraction of the block and whose periodicity depends on the length of the polymer chain.[12,22] The periodicity of the structure can range from a few nm to over 100 nm. A rich variety of nanostructures can be self-assembled based on the intrinsic properties of the blocks and the microdomain geometry, which is influenced by the polymer architecture, the annealing process (e.g. annealing by exposure to a solvent vapor environment or to an elevated temperature), and constraints such as those imposed by a patterned substrate.[23–25] BCPs with two (e.g. diblock copolymers, **Figure 1.1**, or triblock copolymers) or three (e.g. triblock terpolymers) chemically distinct blocks are most commonly used, but incorporating further blocks and various architectures such as linear, star, cyclic or brush copolymers brings more diversity to both the properties and the morphology of the resulting self-assembled structure.[26,27]

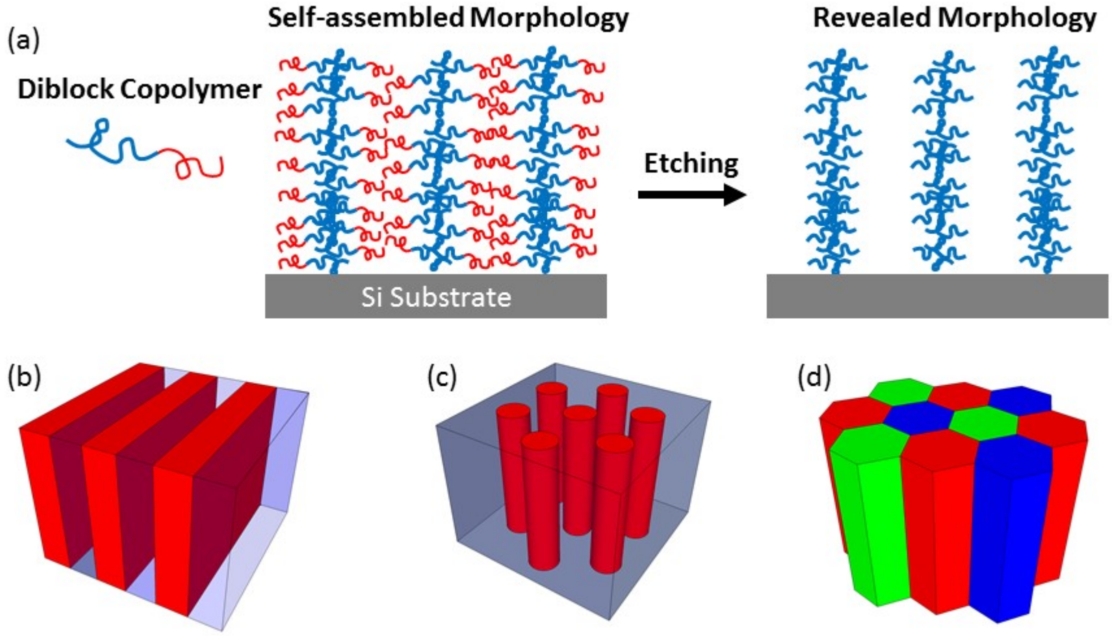

Figure 1.1. Schematics of Block Copolymer self-assembly. (a) Self-assembled morphology of a diblock copolymer, and the morphology revealed after etching one block. (b)-(d) Representative structures from block copolymer self-assembly. (b) lamellae; (c) cylinders, both from a diblock copolymer; (d) Archimedean tiling from a star terpolymer.

The phase behavior of a linear-shape diblock copolymer is governed by three experimentally controllable factors: the degree of polymerization N, the volume fraction of one block f, and the Flory-Huggins interaction parameter χ.[13] N and f are regulated through the polymerization stoichiometry and influence the translational and configurational entropy. The magnitude of χ is determined by the selection of chemically distinct monomers, contribute to the enthalpic part, and is dependent on the temperature $\chi \approx \alpha T^{-1} + \beta$, where $\alpha > 0$ and β are constants for given values of f. At equilibrium, a dense collection of monodisperse diblock copolymer chains will be arranged in minimum free energy configurations. Increasing the interaction parameter χ (i.e. lowering the temperature) favors a reduction in contacts of distinct blocks. If N is sufficiently large, this may be accomplished with some loss of translational and configurational entropy by local compositional ordering (Figure 1.1). Such local segregation is referred to as *microphase separation*, and the local segregated domains are referred to as *microdomains*. Alternatively, if either χ or N is decreased enough, the entropic factors will dominate, leading to a compositionally disordered phase. Since the entropic and enthalpic contributions to the free energy density scale as N^{-1} and χ, respectively, it is the product χN that determines the linear-shape diblock copolymer phase state. Depending on the magnitude of χN, the microphase separation can be *weak segregation limit* ($\chi N \sim 10$), or strong segregation limit ($\chi N \gg 10$).[13] The phase diagram of a typical linear-shape diblock copolymer can be described by the "incompatibility degree" χN and the one independent composition variable (f_A in Figure 1.2a), and consists of structures like spheres, cylinders, lamellae and gyroid. More details of BCP thermodynamics can be found in Ref. 13.

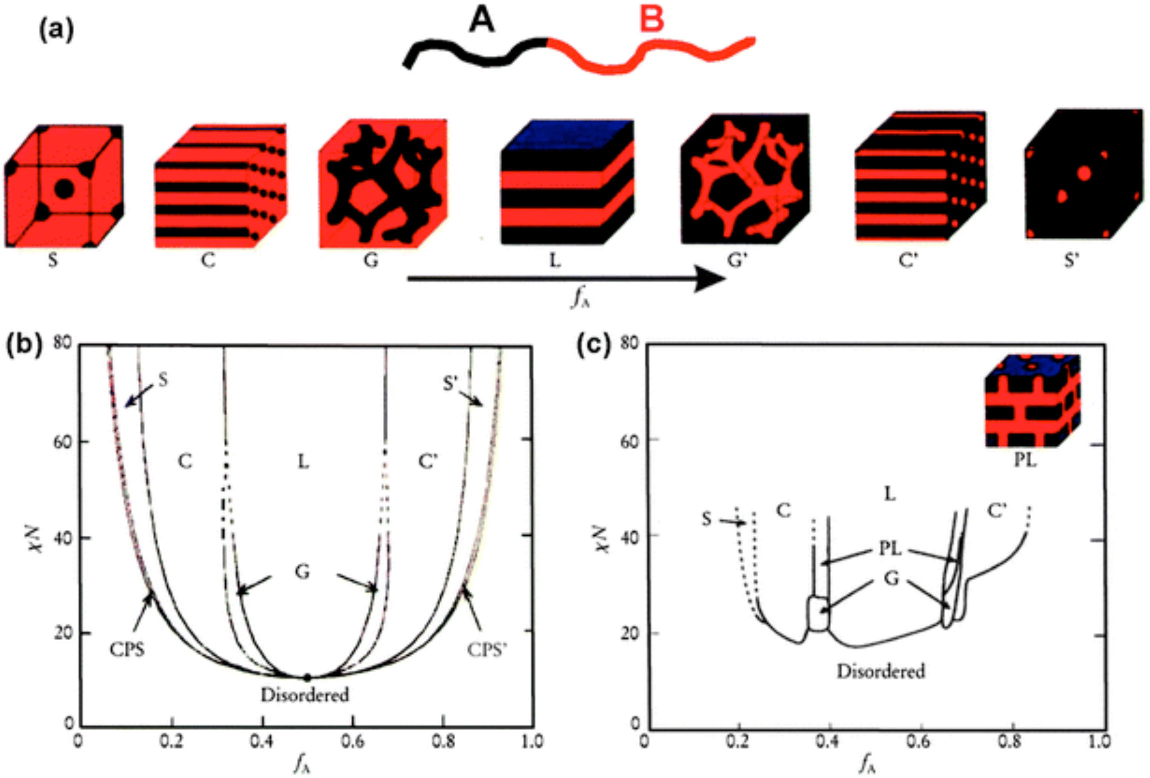

Figure 1.2. Bulk morphology and Phase diagram of diblock copolymer. (a) Equilibrium morphologies of linear-shape diblock copolymers in bulk: S and S'

=body-centered-cubic spheres, C and C' =hexagonally packed cylinders, G and G' =bi-continuous gyroids, and L= lamellae. (b) Theoretical phase diagram of linear-shape diblocks predicted by the self-consistent mean field theory, depending on volume fraction (*f*) of the blocks and the segregation parameter, $\boldsymbol{\chi N}$, where $\boldsymbol{\chi}$ is the Flory-Huggins segment-segment interaction energy and N is the degree of polymerization; CPS and CPS' =closely packed spheres. (c) Experimental phase portrait of polyisoprene-*block*-polystyrene copolymers, in which f_A represents the volume fraction of polyisoprene, PL= perforated lamellae. Reproduced with permission from AIP, Ref. 12.

1.3 Nanolithography

Many applications are based on thin films of BCPs, and one of the most widely studied applications of thin film BCPs is in nanoscale lithography, where one block is removed by etching and the other is used as a mask to define features in a microelectronic device (Figure 1.1). More advanced BCP nanolithography techniques are realized based on combining BCP self-assembly with other widely-used lithography methods. Some of the lithography methods were briefly introduced here.

1.3.1 Photon-based Lithography

Photon-based lithography uses photon to transfer the space profile of photon intensity into a physical profile of a photoresist.[28,29] Photon-induced chemistry changes in the photoresist result in a solubility change of the resist when immersed in a specific solution which is called a developer, so that the developer can dissolve the region that was exposed to photons (Positive Tone Photoresist) or the unexposed regions (Negative Tone Photoresist) depending on the property of the photoresist. The basic steps in photolithography are illustrated in figure 1.3: (i) Exposure; (ii) Development; (iii) Etching.

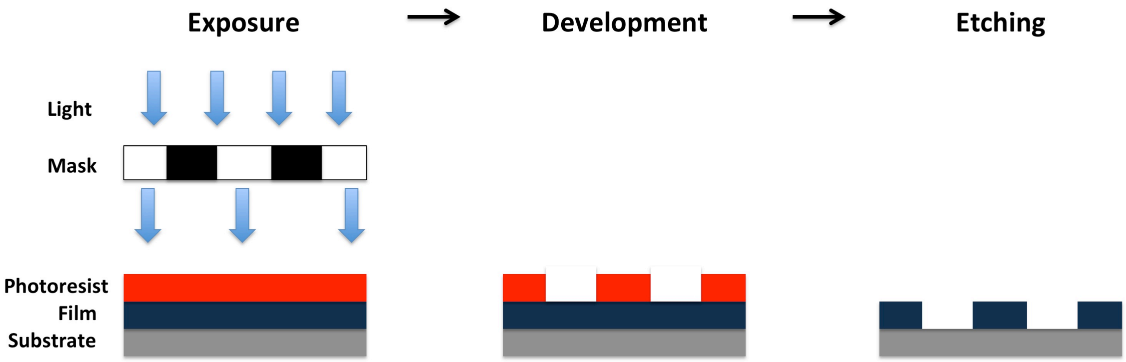

Figure 1.3. Schematic illustration of main steps of photolithography. (i) Exposure; (ii) Development; (iii) Etching.

In the exposure step (figure 1), the space profile of light intensity can be created by inserting a photomask between the light source and the sample. The photomask can be in physical contact with sample (Contact Printing), which results in high resolution, but damage of the mask and defects in the pattern can be induced by trapped fragments between the resist and the mask. To avoid this damage of the mask and the pattern, usually a small gap is kept between the mask and the sample (Proximity Printing), or projection lenses are inserted to both avoid the mask damage and achieve high resolution and uniformity (Projection Printing).

Interference lithography is a type of photolithography without using mask. In interference lithography, the space profile of light intensity is created by the interference between two or more coherent light waves.[30-32] Typically, a coherent laser beam passes through a spatial filter and interferes with a second coherent beam which is reflected from a mirror (Lloyd's Mirror). A standing wave pattern is thus generated at which two beams intersect and record a grating image in the photoresist. The periodicity of the exposed grating can be tuned usually from 100 nm to 1500 nm by varying the wavelength of light (λ) and the half angle between the two beams (θ), as the equation: $P = \lambda/(2\sin(\theta))$. More details on Interference Lithography can be found in Ref. 33.

There are many factors to influence the resolution of patterned features.[34] Among those factors, the wavelength of the light used has a critical effect because diffraction limits resolution. Therefore, the wavelengths of the light continue to decrease from ultraviolet (UV) to extreme UV or X-ray in order to fabricate denser integrated circuits in semiconductor industry.

1.3.2 Electron/Ion-based Lithography

Electron-beam or Ion-beam lithography can fabricate customized pattern with resolution as small as a few nm, which is far beyond the resolution of traditional photolithography. In electron-beam lithography, a resist such as PMMA is used which is sensitive to electron. And cascades of secondary electrons cross-link resist or cause chain scission.[35–37] Similarly, ion-beam lithography uses accelerated ion beam to expose the resist on the substrate. In ion sculpting, the physical bombardment from the heavy ion removes materials from the film creating nanostructure.[38] Furthermore, ion-beam lithography can also be employed for depositing materials such as carbon, platinum, and tungsten.

1.3.3 Imprint and Scanning Probe Lithography

Imprint lithography utilizes a stamp to imprint a solution of molecules (ink) onto a substrate for pattern transferring.[39–41] The stamp or mold can be soft material (such as cross-linked PDMS) or hard material (such as SiO_2). Heating or UV curing may be adopted into imprinting lithography in order to facilitate the viscosity transition of the patterned film after the mold is applied. A schematic of the mechanism is illustrated in figure 1.2. Using a mold enables the large area patterns.

Scanning probe lithography uses the sharp probe in atomic force microscope to heat, scratch, oxidize or transfer substances to the surface of a substrate in order to produce nanostructures. Among these techniques, dip-pen nanolithography is widely used to create patterns directly on a range of substances with a variety of inks.[42,43]

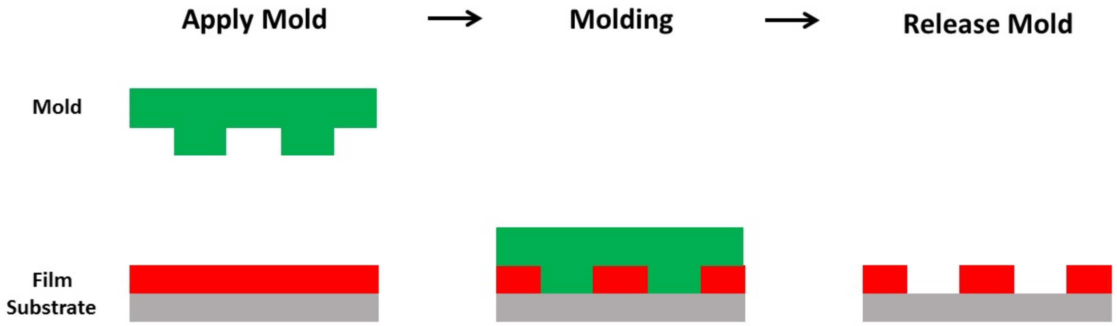

Figure 1.4. Schematic illustration of main steps of imprinting lithography. (i) Apply Mold; (ii) Molding; (iii) Release Mold.

1.3.4 Self-Assembly Lithography

Self-assembly is a process in which structure formation is driven by internal interaction among the components themselves within the system.[44–47] Meanwhile communication with environment also provides influence on the self-assembled structure. Self-assembly phenomena are found at all scales from the universe to a single atom. In nanolithography where interests are currently focused towards shrinking fabricated feature sizes, self-assembly is found particularly useful. In nanoscale fabrication, the idea of "building small hands in order to build small things" finds its limitation, as "smaller hands" become difficult to build. Following the mechanism of how nature multiplies herself, the idea of "structure builds itself" or self-assembly is attractive to explore.

Among those self-assembled systems which includes colloids, lipid bilayers, crystals, phase-separated polymers, and self-assembled monolayers, self-assembly of block copolymer became a classical system to study self-assembly mechanism and a promising material in nanostructure fabrication. A block copolymer is a polymer that covalently unites two or more different monomers, and its molecular architecture can be varied from linear, star-shape, or brush-shape, etc. If the blocks in the block copolymer are immiscible with each other, the block copolymer material tends to phase separate into microdomains to form periodic self-assembled structure. More details on BCP nanostructure fabrication and its application are explained in Chapter 2.

In this thesis work, a Si-containing BCP, polystyrene-*block*-polydimethylsiloxane (PS-*b*-PDMS), is used to explore the self-assembly behavior. PS-*b*-PDMS is useful for nanolithography applications due to the high etch selectivity between the PS and PDMS blocks,[48–50] the etch resistance of the PDMS block, and the high χ parameter ($\chi_{\text{PS-PDMS}} \sim$ 0.14-0.27 at room temperature).[48,51] Self-consistent mean field theory simulation is used to predict the phase behavior of PS-*b*-PDMS self-assembly under different processing conditions or at different templating environment.

1.4 Conclusion

Block copolymer is a classical model to study the mechanism of self-assembly and also a promising material in application of nanolithography, in which other lithography methods could be integrated together with block copolymer lithography. But still, many challenges are remained to explore. Understanding the mechanism of self-assembly both experimentally and theoretically is essential to control the self-assembled nanostructure and lower its defects. Directed self-assembly of BCP is a key to produce device-oriented nanostructure, while templating strategies are still in the necessity of diversification both from fundamental mechanism and from advanced characterization. This thesis is trying to address those challenges by exploring the thin film behavior of a Si-containing BCP, the progress of its self-assembly using in situ observation method, and its templating effect using photon or electron beam patterned substrates or using electric field.

Reference

(1) *Handbook of Nanostructured Materials and Nanotechnology, Five-Volume Set*; Academic Press, 1999.

(2) Mallik, A.; Ryckaert, J.; Mercha, A.; Verkest, D.; Ronse, K.; Thean, A. Maintaining Moore's Law: Enabling Cost-Friendly Dimensional Scaling. In *SPIE Advanced Lithography*; Wood, O. R., Panning, E. M., Eds.; International Society for Optics and Photonics, 2015; p 94221N.

(3) Mun, B. H.; You, B. K.; Yang, S. R.; Yoo, H. G.; Kim, J. M.; Park, W. I.; Yin, Y.; Byun, M.; Jung, Y. S.; Lee, K. J. Flexible One Diode-One Phase Change Memory Array Enabled by Block Copolymer Self-Assembly. *ACS Nano* **2015**, *9* (4), 4120–4128.

(4) Wong, H.-S. P.; Raoux, S.; Kim, S.; Liang, J.; Reifenberg, J. P.; Rajendran, B.; Asheghi, M.; Goodson, K. E. Phase Change Memory. *Proc. IEEE* **2010**, *98* (12), 2201–2227.

(5) Wong, H.-S. P.; Lee, H.-Y.; Yu, S.; Chen, Y.-S.; Wu, Y.; Chen, P.-S.; Lee, B.; Chen, F. T.; Tsai, M.-J. Metal–Oxide RRAM. *Proc. IEEE* **2012**, *100* (6), 1951–1970.

(6) Rebeiz, G. M. *RF MEMS: Theory, Design, and Technology*; John Wiley & Sons, 2004.

(7) Kirsch, J.; Siltanen, C.; Zhou, Q.; Revzin, A.; Simonian, A. Biosensor Technology: Recent Advances in Threat Agent Detection and Medicine. *Chem. Soc. Rev.* **2013**, *42* (22), 8733–8768.

(8) Goodenough, J. B.; Park, K.-S. The Li-Ion Rechargeable Battery: A Perspective. *J. Am. Chem. Soc.* **2013**, *135* (4), 1167–1176.

(9) Fahrenbruch, A.; Bube, R. *Fundamentals Of Solar Cells: Photovoltaic Solar Energy Conversion*; Elsevier, 2012.

(10) Xia, Y.; Rogers, J. A.; Paul, K. E.; Whitesides, G. M. Unconventional Methods for Fabricating and Patterning Nanostructures. *Chem. Rev.* **1999**, *99* (7), 1823–1848.

(11) Liddle, J. A.; Gallatin, G. M. Nanomanufacturing: A Perspective. *ACS Nano* **2016**.

(12) Bates, F. S.; Fredrickson, G. H. Block Copolymers—Designer Soft Materials. *Phys. Today* **1999**, *52* (2), 32.

(13) Bates, F. S.; Fredrickson, G. H. Block Copolymer Thermodynamics: Theory and

Experiment. *Annu. Rev. Phys. Chem.* **1990**, *41*, 525–557.

(14) Darling, S. B. Directing the Self-Assembly of Block Copolymers. *Prog. Polym. Sci.* **2007**, *32* (10), 1152–1204.

(15) Fasolka, M. J.; Mayes, A. M. BLOCK COPOLYMER THIN FILMS: Physics and Applications1. **2003**.

(16) Segalman, R. a. Patterning with Block Copolymer Thin Films. *Mater. Sci. Eng. R Reports* **2005**, *48* (6), 191–226.

(17) Park, C.; Yoon, J.; Thomas, E. L. Enabling Nanotechnology with Self Assembled Block Copolymer Patterns. *Polymer (Guildf).* **2003**, *44* (22), 6725–6760.

(18) Cheng, J. Y.; Ross, C. A.; Smith, H. I.; Thomas, E. L. Templated Self-Assembly of Block Copolymers: Top-Down Helps Bottom-Up. *Adv. Mater.* **2006**, *18* (19), 2505–2521.

(19) Bang, J.; Jeong, U.; Ryu, D. Y.; Russell, T. P.; Hawker, C. J. Block Copolymer Nanolithography: Translation of Molecular Level Control to Nanoscale Patterns. *Adv. Mater.* **2009**, *21* (47), 4769–4792.

(20) Ross, C. A.; Berggren, K. K.; Cheng, J. Y.; Jung, Y. S.; Chang, J.-B. Three-Dimensional Nanofabrication by Block Copolymer Self-Assembly. *Adv. Mater.* **2014**, *26* (25), 4386–4396.

(21) Nunns, A.; Gwyther, J.; Manners, I. Inorganic Block Copolymer Lithography. *Polymer (Guildf).* **2013**, *54* (4), 1269–1284.

(22) Hillmyer, M. Block Copolymer Synthesis. *Curr. Opin. Solid State Mater. Sci.* **1999**, *4* (6), 559–564.

(23) Chavis, M. A.; Smilgies, D.-M.; Wiesner, U. B.; Ober, C. K. Widely Tunable Morphologies in Block Copolymer Thin Films Through Solvent Vapor Annealing Using Mixtures of Selective Solvents. *Adv. Funct. Mater.* **2015**, *25* (20), 3057–3065.

(24) Tavakkoli K G, A.; Hannon, A. F.; Gotrik, K. W.; Alexander-Katz, A.; Ross, C. A.; Berggren, K. K. Rectangular Symmetry Morphologies in a Topographically Templated Block Copolymer. *Adv. Mater.* **2012**, *24* (31), 4249–4254.

(25) Sinturel, C.; Vayer, M.; Morris, M.; Hillmyer, M. A. Solvent Vapor Annealing of Block Polymer Thin Films. *Macromolecules* **2013**, *46* (14), 5399–5415.

(26) Bates, F. S.; Hillmyer, M. A.; Lodge, T. P.; Bates, C. M.; Delaney, K. T.; Fredrickson, G. H. Multiblock Polymers: Panacea or Pandora's Box? *Science* **2012**, *336* (6080), 434–440.

(27) Börner, H. G.; Beers, K.; Matyjaszewski, K.; Sheiko, S. S.; Möller, M. Synthesis of Molecular Brushes with Block Copolymer Side Chains Using Atom Transfer Radical Polymerization. *Macromolecules* **2001**, *34* (13), 4375–4383.

(28) Willson, C. G.; Dammel, R. R.; Reiser, A. Photoresist Materials: A Historical Perspective. In *Microlithography '97*; Tarascon-Auriol, R. G., Ed.; International Society for Optics and Photonics, 1997; pp 28–41.

(29) Seisyan, R. P. Nanolithography in Microelectronics: A Review. *Tech. Phys.* **2011**, *56* (8), 1061–1073.

(30) Savas, T. a; Shah, S. N.; Schattenburg, M. L.; Carter, J. M.; Smith, H. I. Achromatic Interferometric Lithography for 100-Nm-Period Gratings and Grids. *J. Vac. Sci. Technol. B (The 38th Int. Symp. electron, ion, Phot. beams)* **1995**, *13* (6), 2732–2735.

(31) Savas, T. A. Large-Area Achromatic Interferometric Lithography for 100 Nm Period Gratings and Grids. *J. Vac. Sci. Technol. B Microelectron. Nanom. Struct.* **1996**, *14* (6), 4167.

(32) Savas, T. A.; Farhoud, M.; Smith, H. I.; Hwang, M.; Ross, C. A. Properties of Large-Area Nanomagnet Arrays with 100 Nm Period Made by Interferometric Lithography. *J. Appl. Phys.* **1999**, *85* (8), 6160.

(33) Lu, C.; Lipson, R. H. Interference Lithography: A Powerful Tool for Fabricating Periodic Structures. *Laser Photon. Rev.* **2009**, *4* (4), 568–580.

(34) Harriott, L. R. Limits of Lithography. *Proc. IEEE* **2001**, *89* (3), 366–374.

(35) WATT, F.; BETTIOL, A. A.; VAN KAN, J. A.; TEO, E. J.; BREESE, M. B. H. ION BEAM LITHOGRAPHY AND NANOFABRICATION: A REVIEW. *Int. J. Nanosci.* **2005**, *04* (03), 269–286.

(36) Pease, R. F. W. Electron Beam Lithography. *Contemp. Phys.* **2006**, *22* (3), 265–290.

(37) Tseng, A. A.; Chen, C. D.; Ma, K. J. Electron Beam Lithography in Nanoscale Fabrication: Recent Development. *IEEE Trans. Electron. Packag. Manuf.* **2003**, *26* (2), 141–149.

(38) Li, J.; Stein, D.; McMullan, C.; Branton, D.; Aziz, M. J.; Golovchenko, J. A. Ion-Beam Sculpting at Nanometre Length Scales. *Nature* **2001**, *412* (6843), 166–169.

(39) Chou, S. Y.; Krauss, P. R.; Renstrom, P. J. Imprint of Sub-25 Nm Vias and Trenches in Polymers. *Appl. Phys. Lett.* **1995**, *67* (21), 3114.

(40) Resnick, D. J.; Sreenivasan, S. V.; Willson, C. G. Step & Flash Imprint Lithography. *Mater. Today* **2005**, *8* (2), 34–42.

(41) Rogers, J. A.; Nuzzo, R. G. Recent Progress in Soft Lithography. *Mater. Today* **2005**, *8* (2), 50–56.

(42) Ginger, D. S.; Zhang, H.; Mirkin, C. A. The Evolution of Dip-Pen Nanolithography. *Angew. Chem. Int. Ed. Engl.* **2004**, *43* (1), 30–45.

(43) Piner, R. D. "Dip-Pen" Nanolithography. *Science (80-.).* **1999**, *283* (5402), 661–663.

(44) Hawker, C. J.; Russell, T. P. Block Copolymer Lithography: Merging "Bottom-Up" with "Top-Down" Processes. *MRS Bull.* **2011**, *30* (12), 952–966.

(45) Black, C. T.; Ruiz, R.; Breyta, G.; Cheng, J. Y.; Colburn, M. E.; Guarini, K. W.; Kim, H.-C.; Zhang, Y. Polymer Self Assembly in Semiconductor Microelectronics.

IBM J. Res. Dev. **2007**, *51* (5), 605–633.

(46) Black, C. T. Polymer Self-Assembly as a Novel Extension to Optical Lithography. *ACS Nano* **2007**, *1* (3), 147–150.

(47) Yan, H.; Park, S. H.; Finkelstein, G.; Reif, J. H.; LaBean, T. H. DNA-Templated Self-Assembly of Protein Arrays and Highly Conductive Nanowires. *Science* **2003**, *301* (5641), 1882–1884.

(48) Nose, T. Coexistence Curves of Polystyrene/ Poly(dirnethylsiloxane) Blends. *Polymer (Guildf).* **1995**, *36* (11), 2243–2248.

(49) Jung, Y. S.; Ross, C. A. Orientation-Controlled Self-Assembled Nanolithography Using a Polystyrene-Polydimethylsiloxane Block Copolymer. *Nano Lett.* **2007**, *7* (7), 2046–2050.

(50) Son, J. G.; Gotrik, K. W.; Ross, C. A. High-Aspect-Ratio Perpendicular Orientation of PS- B -PDMS Thin Films under Solvent Annealing. *ACS Macro Lett.* **2012**, *1* (11), 1279–1284.

(51) Kennemur, J. G.; Yao, L.; Bates, F. S.; Hillmyer, M. A. Sub-5 Nm Domains in Ordered Poly(cyclohexylethylene)- Block -Poly(methyl Methacrylate) Block Polymers for Lithography. *Macromolecules* **2014**, *47* (4), 1411–1418.

Chapter 2: Functional nanostructured materials based on self-assembly of block copolymers

2.1 Abstract

In this chapter, we review the self-assembly of block copolymer in thin films and in bulk and discuss the self-assembly strategies to fabricate functional nanostructures. Block copolymers microphase separate to form periodic patterns with period of a few nm and above without the need for lithographic guidance. These self-assembled nanostructures have a variety of bulk geometries (alternating lamellae, gyroids, arrays of cylinders or spheres, tiling patterns, core-shell structures) depending on the molecular architecture of the polymer and the volume fraction of its blocks. Moreover, non-bulk morphologies can be produced, the ordering of the microdomains can be improved and their locations directed using various templates and processing strategies. The blocks can themselves constitute a functional material, such as a photonic crystal, or they can be used as a mask to pattern other functional materials, functionalized directly by various chemical approaches, or used as a scaffold to assemble nanoparticles or other nanostructures. Block copolymers therefore offer tremendous flexibility in creating nanostructured materials with a range of applications in microelectronics, photovoltaics, filtration membranes and other devices. This work was published in Ref. [1]

2.2 Introduction

Block copolymers can be used in a wide range of applications,[2,3] constituting functional materials themselves by virtue of the properties of the blocks, or by selectively etching[4,5] one block to form masks or templates for the synthesis of functional materials. BCPs can include organic coil-like blocks, liquid crystalline blocks, Si- or metal-containing blocks, biological blocks, and/or conductive blocks providing a multitude of properties.[6–9] The BCP nanostructure can be altered by several chemical methods such as sequential infiltration synthesis (SIS) which introduces metals or oxides from a precursor as in chemical vapor deposition;[10,11] by salt complexation;[12,13] or by nanoparticle incorporation.[14,15]

In this review, we will first discuss the applications of thin film BCPs in lithography and other fields where a two-dimensional nanopatterned structure is required. We will then discuss three-dimensional BCP assemblies. We show that BCP nanostructures have applications in fabrication of integrated circuits,[16,17] magnetic storage media,[18–20] sensors,[21–24] photonic crystals,[25–27] photovoltaics[28–30] and separation membranes,[31,32] as well as for making 3-dimensional nanostructures.[33]

2.3 Block Copolymers for Nanolithography

In nanolithography, a film of a BCP is prepared on a substrate and one of the blocks is removed. The remaining structure serves as a mask for pattern transfer into a metal, dielectric or other material. This can be carried out using the microdomain pattern made from an untemplated block copolymer film, producing a dense array of dots, holes or lines. However, the greatest efforts have been expended in developing BCP nanolithography for nanoscale electronic devices, where precise registration and reproducibility of the self-assembled nanostructures and low defect levels are essential. Conventional 193 nm wavelength photolithography feature sizes are limited by diffraction, although sub-lithographic feature sizes may be obtained by complex double or quadruple patterning processes. However, 193 nm lithography is unlikely to produce features below about 20 nm dimensions, and directed self-assembly (DSA) of block copolymers has become a candidate planar process for semiconductor device nanofabrication, according to the International Technology Roadmap for Semiconductors.

The period of the microphase-separated BCP structure is governed by the polymer chain length and hence the degree of polymerization, N (the number of monomers constituting the chain) but the driving force for self-assembly is governed by the product χN where χ is the Flory-Huggins interaction parameter quantifying the incompatibility between the blocks. Therefore, high χ is desirable to obtain features with small period from BCPs with low N. BCPs which yield feature period below 10 nm can microphase-separate at room temperature if χ is high enough,[34–36] or by design of the macromolecular architecture (such as brush BCPs). This makes BCP lithography an attractive path to continued device miniaturization.

BCP thin films can be spin-coated from solution like a resist layer, annealed using a hotplate at moderate temperatures or by placing them in a solvent vapor, and etched by reactive ion etching, making them compatible with conventional semiconductor fabrication technology.[37–39] Diblock copolymer films on unpatterned substrates form periodic morphologies after annealing consisting of closepacked spheres, in-plane or out-of-plane-oriented cylinders or lamellae, perforated lamellae, or gyroids, by controlling the block volume fraction[40] and the annealing process.[11,13,41–45] More diverse morphologies can be produced from triBCPs (or multi-BCPs),[14,46,47] mixtures of diBCPs,[48] or multi-BCPs blended with homopolymer.[18,46] For example, square arrays were achieved by using triblock terpolymer/homopolymer blends,[18,49] Archimedean tiling patterns were produced from a 3-miktoarm star terpolymer (a star-shaped polymer where 3 different polymer arms emanate from a core),[46] and blended morphologies between spheres and perforated lamellae were demonstrated by blending a Si-containing BCP with an iron-containing BCP.[48] Examples of thin film BCP morphologies are given in **Figure 2.1.**

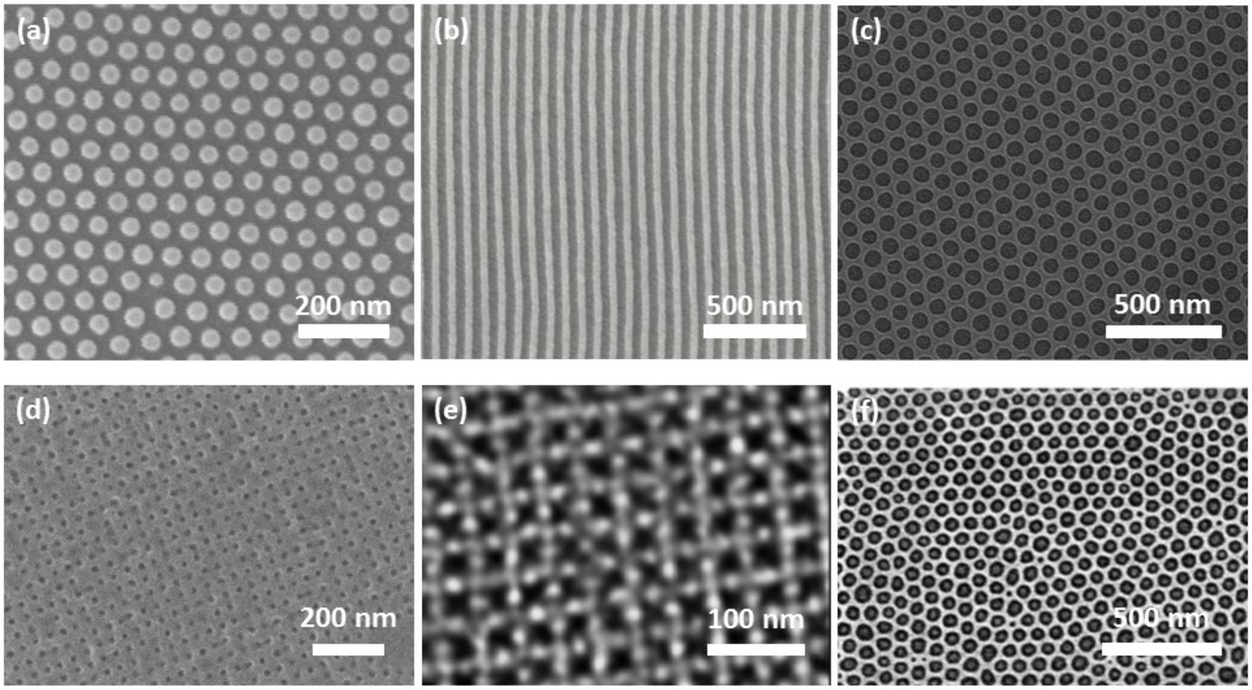

***Figure 2.1. Representative SEMs of thin film self-assembled block copolymer structures**. (a) Monolayer of spheres; (b) cylinders; (c) perforated lamellae; (a), (b), (c) are from a bulk gyroid-forming polystyrene-block-polydimethylsiloxane (PS-b-PDMS) with molecular weight 75.5 kg/mol, and volume fraction f_{PDMS}=0.415; (a), (b) (c) Reproduced with permission.[41] Copyright 2014, ACS Publications; (d) Square array of holes, from a linear triblock terpolymer polyisoprene-b-polystyrene-b-polyferrocenylsilane (PI-b-PS-b-PFS) with volume fractions of 25%, 65%, and 10%, respectively, and total molecular weight 82 kg/mol, blended with Polystyrene homopolymer; Reproduced with permission.[47] Copyright 2012 ACS Publications; (e) Archimedeam tiling pattern, from a 3-miktoarm star terpolymer (polyisoprene-arm-polystyrene-arm-*

polyferrocenylethylmethylsilane with volume fractions of 39%, 35%, 26%, respectively, and total molecular weight 66 kg/mol) blended with polystyrene homopolymer; Reproduced with permission.[46] *Copyright 2013, ACS Publications; (f) Hierarchical nanostructure, from blend of a polydimethylsiloxane-b-polystyrene (PDMS-PS, M_W=45.5 kg/mol, f_{PDMS}=33.7%) and a polystyrene-b-polyferrocenyldimethylsilane (PS-PFS, M_W=35 kg/mol, f_{PFS}=11.5%). Reproduced with permission.*[48] *Copyright 2013, Nature Publishing Group.*

The microdomain patterns formed in thin films of BCPs possess short-range order but lack long-range order, as seen in some of the images of Figure 2. A top-down method can be employed to guide BCP self-assembly, providing registration and alignment with features in the substrate, and minimizing the defectivity. Graphoepitaxy and chemoepitaxy are the two main templating strategies for DSA[50–55] using confinement-induced structural frustration and interfacial interactions respectively to control BCP self-assembly. This can produce well-ordered periodic arrays as well as aperiodic structures not found in bulk.[56–60] Topographical templates include small posts fabricated by electron-beam lithography, functionalized to be attractive to one block,[61] or trenches fabricated by photolithography or interference lithography;[62–65] whereas chemoepitaxy templates consist of chemically distinct regions of the substrate that are attractive to one or other block, such as stripes, bends, dots and other features [66–68]. In both graphoepitaxy and chemoepitaxy, pattern multiplication has been demonstrated, i.e. the density of templating features can be less than the final density of the BCP pattern.[51,66,78] To optimize the templates in order to produce desired self-assembled BCP geometries, inverse design algorithms combined with self-consistent field theory (SCFT) simulations have been developed, in which SCFT can predict the BCP morphologies at conditions of film thickness, topographic confinements, and surface energy.[16,69–72]

Figure 2.2 shows examples of BCP films templated by graphoepitaxy (Fig. 2.3a-e,g,h) and chemoepitaxy (Fig. 2.3f). Scaleup of these processes to wafer level using templates made by photolithography has been demonstrated.[73–75]

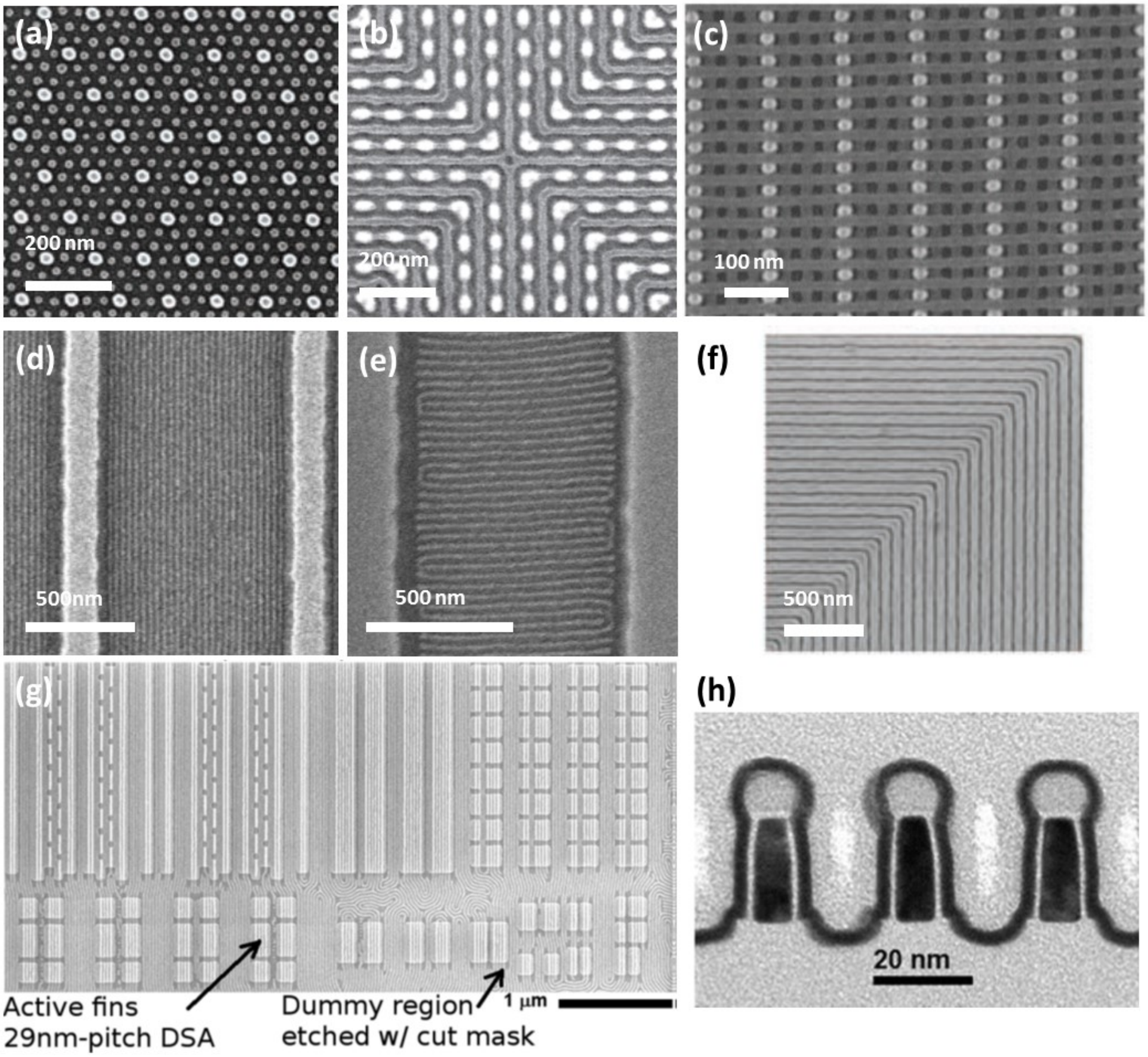

Figure 2.2. Directed self-assembly of BCPs. *(a) SEM of ordered BCP spheres formed within a sparse 2D lattice of HSQ posts (brighter dots). The substrate and post surfaces were functionalized with a PS brush layer; Reproduced with permission.*[51] *Copyright 2008, AAAS. (b) By using an array of dashes oriented in the x- and y- directions, nested-elbow structures form with a cross-point junction in the center; Reproduced with permission.*[76] *Copyright 2010, Nature Publishing Group; (c) SEM of an etched 3D bilayer structure on a substrate. The bright dots and the light gray linear features represent HSQ and oxidized-PDMS, respectively; Reproduced with permission.*[61] *Copyright 2012, AAAS; (d) SEM of parallel cylinders on a trenched substrate with narrow mesas (width* W_{mesa}*=125 nm and* W_{trench}*= 875 nm) annealed under a high vapor pressure of toluene. (e) SEM of perpendicular cylidners in a wide mesa pattern (*W_{mesa}*=270 nm and* W_{trench}*=730 nm) at a lower vapor pressure. (d), (e) reproduced with permission.*[77] *Copyright*

2007, ACS Publications (f) Top-down SEM of 90^o-angled lamellae from chemoepitaxy of a ternary PS-b-PMMA/PS/PMMA blend. Reproduced with permission.[78] Copyright 2005, AAAS (g) Directed self-assembly of lamellar phase PS-b-PMMA BCP to form line-space circuit patterns in order to fabricate Si fin features; (h) A transmission electron microscope image of 29 nm pitch silicon on insulator fins formed by BCP directed self-assembly. (g), (h) reproduced with permission.[63] Copyright 2014, ACS Publications.

As mentioned above, a high χ is desirable to obtain microdomains with small period. However, high-χ BCPs usually exhibit large differences in surface energy between the blocks, leading to the formation of a layer of the lower surface energy block at the air interface, and favoring in-plane orientation of lamellar or cylindrical microdomains. Perpendicularly-oriented microdomains provide higher aspect ratio features that facilitate pattern transfer, and can be promoted by a neutral coating,[79,80] a comb-like polymer architecture,[81] and processing under external conditions including electric field,[82–84] magnetic field,[85] temperature gradient,[86–88] solvent gradient,[80,89,90] shear,[91,92,93] zone casting,[94] Electrohydrodynamic Jet Printing[95] or electrospray deposition[96]. **Figure 2.3** shows examples of the alignment of BCP microdomains perpendicular to the substrate.

In contrast to the precise and intricate structures formed by DSA, some applications only require short-range-ordered nanostructures with or without a common orientation. This is straightforward to accomplish by BCP thin film self-assembly. Examples include porous dielectrics[97,98] such as the IBM Airgap,[99] filtration membranes or water desalination membranes,[100] some photovoltaic membranes,[101,102] and electrodes for batteries.[103,104]

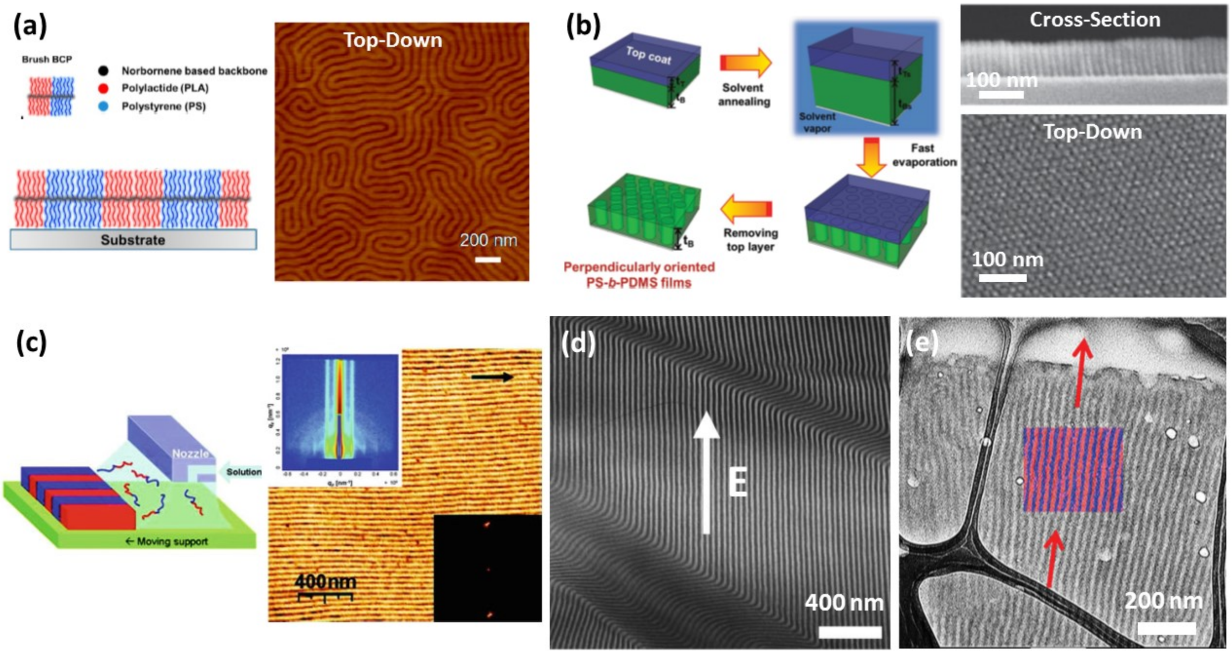

***Figure 2.3. Controlling the orientation of microdomains**. (a) Lamellar microdomains oriented perpendicular to the substrate from the self-assembly of a brush BCP, Left: schematic, Right: AFM; Reproduced with permission.*[81] *Copyright 2013, ACS Publications; (b) The solvent annealing process of block copolymer thin films with a top coat layer to produce a perpendicular orientation of the microdomains. Top coats were carefully chosen for solvent permeability during solvent annealing and were simply removed with a non-solvent for both blocks of the BCP. Left: schematic, Right: SEM of cross-section and top-down view; Reproduced with permission.*[80] *Copyright 2014, Wiley-VCH; (c) Zone casting method to direct the self-assembly of BCPs; Left: semicrystalline lamellar poly(octadecyl methacrylate)-b-Poly(t-butyl acrylate)-b-Poly(octadecyl methacrylate) (PODMA-b-PtBA-b-PODMA) system above and below melting point. Right: AFM images and GISAXS patterns of aligned microdomains. Arrow indicates casting direction. Reproduced with permission.*[94] *Copyright 2011, ACS Publications; (d) Electric-field-induced alignment of block copolymer microdomains. TEM image of lamellar-forming polystyrene-block-polyisoprene (SI) BCP morphology after electric-field alignment. Reproduced with permission.*[105] *Copyright 2002, APS; (e) The electrospray process of polystyrene-b-polybutadiene-b-polystyrene (SBS) triBCP. Small droplets containing SBS are generated from a charged atomizer and transported onto heated substrate. Arriving SBS particles equilibrate with the substrate and adopt out-of-plane morphology dictated by the strong evaporation of solvent. Crosslinking of PB*

occurs simultaneously with ordering as the film undergoes thermal annealing, preserving the vertical alignment of the film. Reproduced with permission.[96] *Copyright 2015, Wiley-VCH.*

2.4 Pattern transfer from 2D block copolymer films

In some applications the BCP film itself forms the functional material, such as a porous dielectric formed by etching a BCP film, but in many cases the BCP film is used as a sacrificial mask for patterning another material.[33,106–109] Monolayers of in-plane cylinders or spheres, perpendicular cylinders and lamellae, and perforated lamellae are particularly suitable for pattern transfer. Pattern transfer takes advantages of the methods developed for planar processing, including additive (e.g. liftoff) and subtractive (etching) methods. **Figure 2.4** shows how these processes were applied to pattern dots of Co using a polystyrene-*block*-polydimethylsiloxane (PS-*b*-PDMS) BCP.

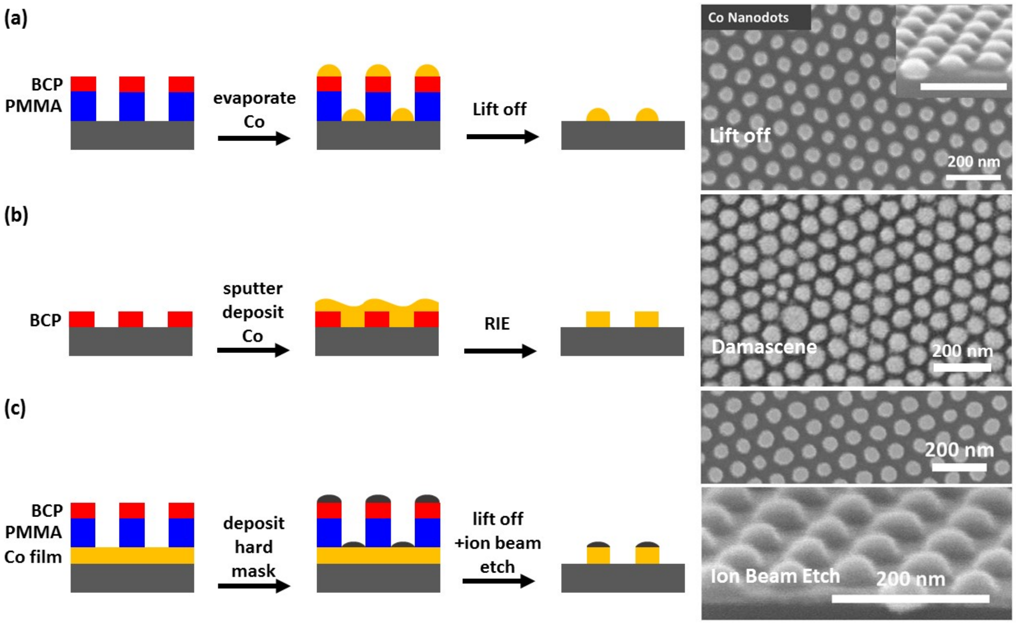

Figure 2.4. Pattern transfer from a BCP film*. (a) Left: Schematic of liftoff from a BCP mask using a sacrificial PMMA underlayer, Right: SEM of cobalt nanodots fabricated by lift-off process. Inset: tilted views illustrate edge tapering; (b) Left: Schematic of Damascene pattern transfer process from BCP to metal nanostructure. Right: SEM of cobalt nanodots transferred from a PS-b-PDMS perforated lamellar structure; (c) Left: Schematic of subtractive pattern transfer process from BCP self-assembled mask by ion-beam etch process. Right: Plan view and cross-sectional SEM showing the cobalt nanodots transferred from a*

perforated lamellar pattern using a hard mask of tungsten. Reproduced with permission.[108] *Copyright 2015, IOPscience*

Etching an underlying material through a BCP mask allows pattern transfer into many materials including multilayers or epitaxial structures that cannot be grown on top of the BCP mask.[108,110,111] The success of the etching process depends on the etch contrast between the BCP mask and the material, the aspect ratio of the mask, the relative thicknesses of the layers, and available etch chemistries for the material. Reactive ion etching or ion-beam etching are typically used, and the BCP pattern may first be transferred into a hard mask such as a heavy metal (Ta, W, etc.) or hard carbon which has greater durability than the BCP film during the etch of the functional material.

Additive patterning has also been widely applied including electrodeposition, lift-off and damascene processes.[18,112] Lift-off involves depositing the functional material onto a soluble BCP pattern with vertical or undercut pores using a collimated vapor deposition process such as evaporation to produce well-defined edge morphologies of the deposited material. Dissolving the BCP pattern removes the material on top of it, leaving only the material that was deposited on the substrate at the bottom of the pores. The solubility of the BCP can be improved, and the pore aspect ratio and sidewall undercut enhanced, by using a sacrificial layer such as PMMA inserted between the BCP film and the substrate, which is etched through to the substrate in the locations of the BCP pores. In a damascene process,[111] the functional material is deposited over BCP topographical features then etched back and planarized by, for example, reactive ion etching. Etching is stopped once it has reached the BCP features, leaving the functional material within the pores of the BCP film. The remaining BCP can then be selectively removed.[113]

2.5 Block copolymer-based routes to 3D nanostructured materials

So far we have discussed 2D or planar processing where a layer of BCP microdomains is used to pattern a film or surface. BCPs can also produce 3D structures which can be built up from 2D layers, or which can be formed in one step from thick film or bulk BCPs with multiple layers of microdomains.

One class of synthetic routes involves building a 3D functional material from stacks of 2D layers or by repeatedly templating one BCP on another.[33]

Independent BCP layers can be stacked by separating them, for example using a graphene or silicon layer in between the layers.[114,115] The orientation of microdomains in different layers can be controlled independently by shear alignment induced by a laser pulse, solvent incorporation, a thermal gradient, or direct mechanical shear. This has been used to make lattice structures with arbitrary symmetries from a cylinder-forming BCP.[116,117] Sequential self-assembly processes use the etched self-assembled BCP microdomains of a lower layer as a new template for an upper layer of the same or different BCP, which can result in a wide range of novel 3D nanostructures.[118] The orientation of one layer of cylinders on another one can be controlled by the substrate chemistry and topography.[119] Meshed structures consisting of two layers of cylinders at an angle to each other can also be made in one step by suitable templating.[71,120] **Figure 2.5** shows examples of these structures.

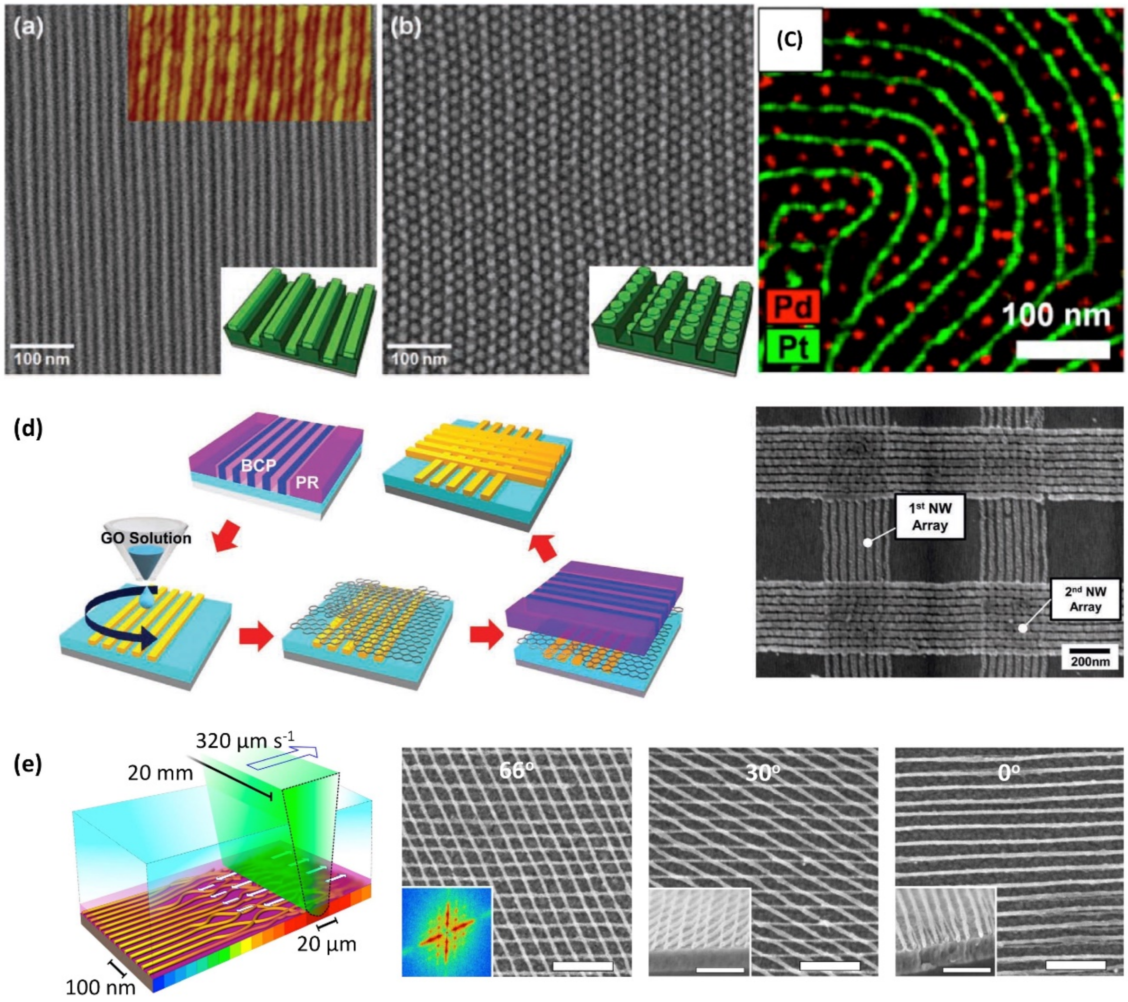

Figure 2.5. Sequential Self-assembly Processes. *(a) Hierarchical line-on-line structures made from 16 kg mol*$^{-1}$ *PS-b-PDMS line patterns on 45 kg mol*$^{-1}$ *line*

patterns. (b) Self-assembly of 16 kg mol^{-1} PS-PDMS dot patterns on 45 kg mol^{-1} PS-b-PDMS line patterns forming a dots-on-line structure. (a), (b) reproduced with permission.[118] *Copyright 2011, Wiley-VCH; (c) Multicomponent nanopatterning and elemental mapping of Pt nanowire-Pd nanodot array made using sequential BCP self-assembly. Reproduced with permission.*[121] *Copyright 2013, ACS Publications; (d) Left: Schematic showing independent control of a double layer of BCP microdomains by inserting a graphene layer in between the BCP layers. Right: Al nanowire crossbar array made from double layers of orthogonally directed self-assembly; Reproduced with permission.*[114] *Copyright 2013, Wiley-VCH; (e) Soft-shear laser zone annealing (SS-LZA). SS-LZA is used to produce aligned BCP templates for nanowire synthesis. Experimental schematic: a focused laser line is absorbed by a layer of germanium underlying a BCP film, inducing local heating and high thermal gradients. At the same time the thermal expansion of an overlaid PDMS sheet shears and aligns the BCP. Reproduced with permission.*[117] *Scale bars 200 nm. Copyright 2015, Nature Publishing Group.*

3D BCP structures can be obtained from bulk BCPs or from films thick enough to show periodic structures in the out of plane direction. BCPs confined in pores with cylindrical or spherical shape show a diversity of non-bulk 3D structures,[57,122–124] for example helical, toroidal or concentric cylindrical morphologies.[123]

Converting these 3D morphologies into functional materials can be done by a variety of methods. One block can be replaced by another material, for example by etching it and backfilling by electrodeposition,[116,125] or by selectively depositing material by SIS[10] or chemical reduction. SIS uses precursors such as those used in chemical vapor deposition: $TiCl_4$, $AlCl_3$, $Al(CH_3)_3$, etc.[126] Chemical reduction of precursors took place in the poly(ethylene oxide) microdomains of a cylinder-forming polystyrene-*block*-poly(ethylene oxide) (PS-*b*-PEO) BCP, which tuned the material chemistry of the resulting self-assembled nanostructure and changed the microdomain orientation.[12] Nanoparticles such as Au can be formed within poly-4-vinylpyridine blocks by reduction of salts.[127] Alternatively nanoparticles can be synthesized separately and blended with the BCP during casting to produce a co-assembled structure.[27,28,128] The nanoparticles can be located within the microdomains or at the interfaces. As an example a blend of Au nanoparticles capped with 1-dodecanethiol and a cylinder-forming polystyrene-*block*-poly-4-vinylpyridine (PS-*b*-P4VP) BCP hydrogen-bonded to 3-pentadecylphenol was annealed under chloroform vapor and produced hexagonally packed 3D structures in which the Au nanoparticles were selectively located at the interstitial sites in the P4VP matrix.[129]

2.6 Functional materials made from BCPs

Nanostructured films made by pattern transfer from a BCP layer using planar processing have exhibited a wide range of interesting and useful properties.[130] Some examples of these structures are given in **Fig. 2.6.** For example, considerable effort has been applied to patterning of magnetic films for patterned media applications. The magnetic anisotropy, magnetic domain structure and reversal process are dominated by the shape and size of the features as well as the material properties. Arrays of magnetic dots, rings or pores have been made from various magnetic alloys. [33,131–133] A recent study compared the properties of Co dots made by additive and subtractive methods using the same BCP, determining that etching produced the smallest switching field distribution.[108] Bit patterned media with area density beyond 1.5 teradot/inch^2 was achieved by pattern transfer from an ordered BCP.[133]

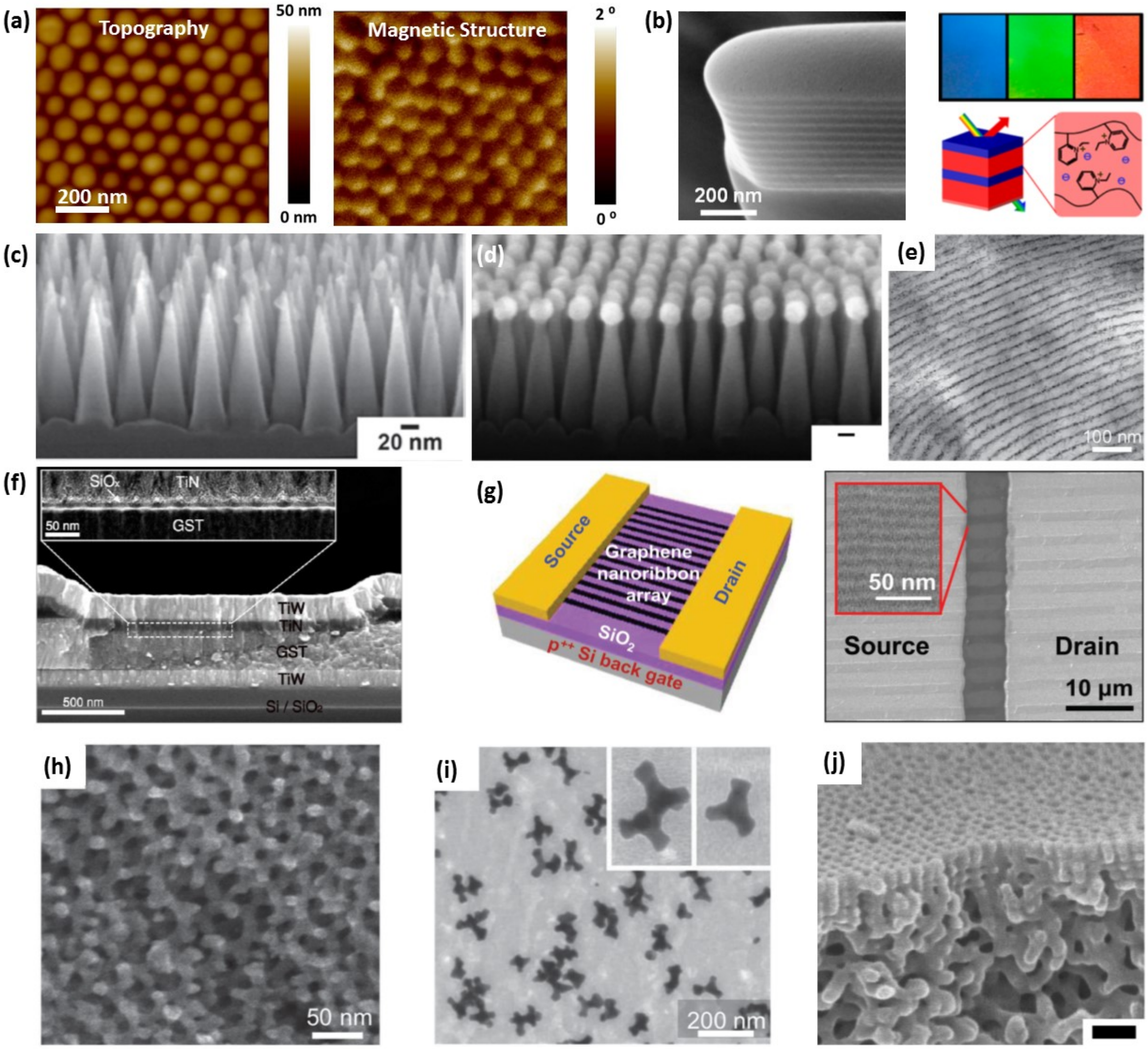

Figure 2.6. Functional materials made using block copolymers. *(a) Left: The surface topography of ion-beam etched cobalt nanodots imaged by scanning probe microscopy, Right: The corresponding magnetic structure of the patterned nanodots showing in-plane magnetization; Reproduced with permission.*[108] *Copyright 2015, IOPscience; (b) Left: Cross-Sectional SEM (52*^{o} *tilt) of a focused ion beam milled dry PS-b-QP2VP lamellar film. To enhance the layer contrast, the films were exposed to iodine vapor for a selective staining of the QP2VP layers, resulting in brighter layers. Right: Schematic representation of the mechanism for color change in a PS-b-QP2VP photonic lamellar gel by a direct exchange of counterions leading to swelling. Reproduced with permission.*[134] *Copyright 2012, ACS Publications; (c) Side-view SEM of a silicon superhydrophobic surface textured with nanocones; Reproduced with permission.*[135] *Copyright 2014, Wiley-VCH; (d) Side-view SEM of silicon nanotextured surface that exhibits antireflective properties; Reproduced with permission.*[136] *Copyright 2015, Nature Publishing*

Group; (e) Co-assembly: TEM image of CdSe nanorods co-assembled with PS-b-P4VP /(pentadecylphenol (PDP))$_1$ *film. Reprinted with permission.*[137] *Copyright 2012, American Chemical Society. (f) Cross-sectional SEM images of a phase-change memory device. The inset shows a TEM image of the interface between TiN and GeSbTe, where the self-assembled nanostructures are incorporated; Reproduced with permission.*[138] *Copyright 2013, ACS Publications; (g) Schematic of a FET based on graphene nanoribbon arrays patterned by BCP lithography and the corresponding SEM image. Reproduced with permission.*[139] *Copyright 2013, Wiley-VCH; (h) Chiral plasmonic structure made from Au templated in a gyroid triblock terpolymer. Reproduced with permission.*[125] *Copyright 2011, Wiley-VCH. (i) Branched Au plasmonic structures from seeded electrodeposition in a gyroid BCP. The inset shows an enlarged area. Reproduced with permission.*[140] *Copyright 2013, Wiley-VCH. (j) filtration membrane, cross-section near the surface showing ordered pores extending for about 100 nm vertically into the film above a disordered porous network. Reproduced with permission.*[141] *Copyright 2011, ACS Publications.*

Several microelectronic devices such as nanowire transistors,[142] capacitors,[143] phase change memories, [138,144] resistive memories,[145] or triboelectric generators[146] have been made using BCPs. Sub-10 nm wide graphene nanoribbon array field-effect transistors were fabricated by using PS-*b*-PDMS as a etch mask.[139] In phase-change memory, an insulating silica nanostructure produced from the self-assembly of PS-*b*-PDMS, incorporated between the phase change material and the heater electrode reduced the switching volume of the phase change material in order to resolve the chronic issue of power consumption.[138]

Bulk BCP structures such as gyroids,[147] lamellae or cylinders are attractive in applications such as batteries, photovaltics and photonics. In the field of photonics, reflective iridescent colors can be produced from optical microstructures with periodic microdomains of alternating refractive index.[26,27] Well-ordered BCP microdomain arrays can produce photonic bandgaps spanning the entire visible spectrum and with large tunability by swelling. [37,38,39,134,148] As shown in **Fig 2.6b**, the tunable BCP photonic gels were well-ordered self-assembled lamellae of polystyrene-*block*-poly(2-vinylpyridine) with the P2VP layers quaternized (PS-*b*-QP2VP). The total dry film thickness is 1 μm, which is around 20 times the PS-*b*-QP2VP periodicity. The swelling of the PS-b-QP2VP lamellae induced by exposure to aqueous solvent vapor showed full-color tunability.[134]

Superhydrophobic surfaces have self-cleaning, antireflection and anti-bacterial functions and can be produced from nanostructured films of block copolymers. For example, nano-cone textures transferred from sphere-forming PS-*b*-PMMA have shown advancing water contact angle exceeding 160°.[135] A moth eye nanostructure fabricated from the self-assembly of PS-*b*-PMMA has shown broadband antireflection properties.[163] Amphililic block copolymers have been used as building blocks for the preparation of micellar drug carriers. Typical BCPs for drug delivery include a poly(ethylene oxide) (PEO) block, because of its hydrophilicity that can form a tight shell entrapping the micellar drug core enabling transport at concentrations that can exceed the intrinsic water-solubility of the drug.[149] BCPs have also been used to make detectors for biomolecules[24] as well as for solvent vapors.[34]

Nanoporous membranes produced from BCP films can generate a high density of uniform pores with diameter from 10 nm to below 200 nm, and are treated as promising materials for tunable filtration with high permeability and selectivity.[150] Typical BCP filtration membranes preparation methods include spin casting or bulk casting and thinning with a doctor blade directly on a macroporous substrate; or an indirect method by first coating on a nonporous substrate and then transferring to a macroporous substrate. Nanoporous structures with graded pore sizes were demonstrated using PS-*b*-P4VP in a tetrahydrofuran and dimethylformamide solvent system.[151] A film made from a blend of PMMA homopolymer with cylinder-forming PS-*b*-PMMA with its microdomains oriented normal to the surface was floated onto a macroporous support to demonstrate virus filtration.[152] A simple nanoporous structure fabrication process used PS-*b*-PEO with oligomeric PEO (o-PEO) as the additive. After thermal annealing, the film was immersed in a protic solvent (e.g., water, methanol, or ethanol) to dissolve and remove the o-PEO while the PS is still in a frozen state, producing pores in the locations of the o-PEO.[151] Roll-to-roll cold zone annealing realized the mass production of thin films with vertically-oriented BCP microdomains which can be used as filtration membranes.[153]

Nanoparticle inclusion within BCPs can produce a well-ordered morphology in which the orientation and spatial arrangement of the nanoparticles, and thus their anisotropic physical properties, can be controlled.[27,28,132,154–156] For example, localized surface plasmon resonance and surface-enhanced raman scattering from nanorods with ordered arrangement and common orientation can be used for photonics or for sensing.[157,158] A self-assembled BCP nanostructure can be treated as a 3D template after one block is removed, and back-filling of nanoparticles such as those made of transition metal oxide particles can provide unique electronic, optical and catalytic properties, useful in applications such as solar cells and batteries.[104]

A final example we discuss is the fabrication of excitonic photovoltaics. In these structures the donor-acceptor interfaces are critical for photogeneration of charges and device performance. Conjugated BCPs such as poly(3-hexylthiophene)-block-poly(ethylene oxide) (P3HT-*b*-PEO),[159] poly(3-hexylthiophene)-block-poly((9,9-dioctylfluorene)-2,7-diyl-alt-[4,7-bix(thhiophen-5-yl)-2,1,3-benzothiadiazole]-2',2"-diyl) (P3HT-*b*-PFTBT),[101] or poly(3-hexylthiophene)-block-polylactide (P3HT-*b*-PLA) with C_{60} have all demonstrated efficient photoconversion and good device stability.[160] Early organic solar cells had a bilayer architecture where the acceptor material was deposited on top of the donor material, but this structure suffered from high excitonic losses. Subsequent organic solar cells intermixed the donor and acceptor material in a bulk heterojunction active layer, but the disordered interface morphology was still not optimized and the stability of the device was limited by macrophase separation. A conjugated donor-acceptor BCP can resolve these problems, allowing a stable active layer morphology to be optimized based on the block volume fraction and annealing process.[161]

2.7 Summary

We have seen that BCPs offer extensive opportunities for the fabrication of functional materials. This can take advantage of the bulk periodic morphology of the BCP, or of thin films or confined regions of the BCP in which non-bulk morphologies can form. Microdomains can be aligned by applying fields, shear, solvent evaporation, temperature gradients or substrate topography, and their positions can be precisely controlled by nanoscale graphoepitaxial or chemoepitaxial substrate features. BCPs may themselves be functional, for example they can include conjugated blocks for charge transfer, or they can be used as templates to produce other functional materials. Numerous methods exist for pattern transfer, including the incorporation of nanoparticles within one block, selective deposition in one block using infiltration or chemical reduction, etching of one block and backfilling, or using a film of the BCP as a mask for planar processes such as etching or liftoff. BCPs enable hierarchical synthesis where one material is templated by another to give a material with different length scales.

BCP-inspired functional materials are already in use or under development for a vast range of applications, including membranes, photovoltaics and nextgeneration lithography. Their role will certainly increase as BCP synthesis, processing and pattern transfer methods improve.

References

(1) Bai, W.; Ross, C. A. Functional Nanostructured Materials Based on Self-Assembly of Block Copolymers. *MRS Bull.* **2016**, *41* (February), 100–107.

(2) Schacher, F. H.; Rupar, P. A.; Manners, I. Functional Block Copolymers: Nanostructured Materials with Emerging Applications. *Angew. Chem. Int. Ed. Engl.* **2012**, *51* (32), 7898–7921.

(3) Yoo, H. G.; Byun, M.; Jeong, C. K.; Lee, K. J. Performance Enhancement of Electronic and Energy Devices via Block Copolymer Self-Assembly. *Adv. Mater.* **2015**, *27* (27), 3982–3998.

(4) Chang, S.-W.; Chuang, V. P.; Boles, S. T.; Ross, C. A.; Thompson, C. V. Densely Packed Arrays of Ultra-High-Aspect-Ratio Silicon Nanowires Fabricated Using Block-Copolymer Lithography and Metal-Assisted Etching. *Adv. Funct. Mater.* **2009**, *19* (15), 2495–2500.

(5) Choi, H. K.; Gwyther, J.; Manners, I.; Ross, C. a. Square Arrays of Holes and Dots Patterned from a Linear ABC Triblock Terpolymer. *ACS Nano* **2012**, *6* (9), 8342–8348.

(6) Kulbaba, K.; Manners, I. Polyferrocenylsilanes: Metal-Containing Polymers for Materials Science, Self-Assembly and Nanostructure Applications. *Macromol. Rapid Commun.* **2001**, *22* (10), 711–724.

(7) Zhou, Y.; Ahn, S.; Deshmukh, P.; Kasi, R. M. *Liquid Crystalline Block Copolymers*; Encyclopedia Of Polymer Science and Technology. John Wiley & Sons, Inc.: Hoboken, NJ, USA, 2013.

(8) OLSEN, B.; SEGALMAN, R. Self-Assembly of Rod–coil Block Copolymers. *Mater. Sci. Eng. R Reports* **2008**, *62* (2), 37–66.

(9) Ross, C. A.; Jung, Y. S.; Chuang, V. P.; Ilievski, F.; Yang, J. K. W.; Bita, I.; Thomas, E. L.; Smith, H. I.; Berggren, K. K.; Vancso, G. J.; Cheng, J. Y. Si-Containing Block Copolymers for Self-Assembled Nanolithography. *J. Vac. Sci. Technol. B Microelectron. Nanom. Struct.* **2008**, *26* (6), 2489–2494.

(10) Peng, Q.; Tseng, Y.-C.; Darling, S. B.; Elam, J. W. A Route to Nanoscopic Materials via Sequential Infiltration Synthesis on Block Copolymer Templates. *ACS Nano* **2011**, *5* (6), 4600–4606.

(11) Tseng, Y.-C.; Peng, Q.; Ocola, L. E.; Elam, J. W.; Darling, S. B. Enhanced Block Copolymer Lithography Using Sequential Infiltration Synthesis. *J. Phys. Chem. C* **2011**, *115* (36), 17725–17729.

(12) Kim, S. H.; Misner, M. J.; Yang, L.; Gang, O.; Ocko, B. M.; Russell, T. P.

Salt Complexation in Block Copolymer Thin Films. *Macromolecules* **2006**, *39* (24), 8473–8479.

(13) Wang, J.-Y.; Chen, W.; Russell, T. P. Ion-Complexation-Induced Changes in the Interaction Parameter and the Chain Conformation of PS- B -PMMA Copolymers. *Macromolecules* **2008**, *41* (13), 4904–4907.

(14) Zhao, Y.; Thorkelsson, K.; Mastroianni, A. J.; Schilling, T.; Luther, J. M.; Rancatore, B. J.; Matsunaga, K.; Jinnai, H.; Wu, Y.; Poulsen, D.; Fréchet, J. M. J.; Alivisatos, A. P.; Xu, T. Small-Molecule-Directed Nanoparticle Assembly towards Stimuli-Responsive Nanocomposites. *Nat. Mater.* **2009**, *8* (12), 979–985.

(15) Zhang, Q.; Xu, T.; Butterfield, D.; Misner, M. J.; Ryu, D. Y.; Emrick, T.; Russell, T. P. Controlled Placement of CdSe Nanoparticles in Diblock Copolymer Templates by Electrophoretic Deposition. *Nano Lett.* **2005**, *5* (2), 357–361.

(16) Yi, H.; Bao, X.-Y.; Tiberio, R.; Wong, H.-S. P. A General Design Strategy for Block Copolymer Directed Self-Assembly Patterning of Integrated Circuits Contact Holes Using an Alphabet Approach. *Nano Lett.* **2015**, *15* (2), 805–812.

(17) Black, C. T.; Ruiz, R.; Breyta, G.; Cheng, J. Y.; Colburn, M. E.; Guarini, K. W.; Kim, H.-C.; Zhang, Y. Polymer Self Assembly in Semiconductor Microelectronics. *IBM J. Res. Dev.* **2007**, *51* (5), 605–633.

(18) Xiao, S.; Yang, X.; Edwards, E. W.; La, Y.-H.; Nealey, P. F. Graphoepitaxy of Cylinder-Forming Block Copolymers for Use as Templates to Pattern Magnetic Metal Dot Arrays. *Nanotechnology* **2005**, *16*, S324–S329.

(19) Yang, X.; Wan, L.; Xiao, S.; Xu, Y.; Weller, D. K. Directed Block Copolymer Assembly versus Electron Beam Lithography for Bit-Patterned Media with Areal Density of 1 Terabit/inch(2) and Beyond. *ACS Nano* **2009**, *3* (7), 1844–1858.

(20) Cheng, J. Y.; Ross, C. A. *Block Copolymer Lithography for Magnetic Device Fabrication*; Tsui, O. K. C., Russell, T. P., Eds.; World Scientific, 2008.

(21) Jung, Y. S.; Jung, W.; Tuller, H. L.; Ross, C. A. Nanowire Conductive Polymer Gas Sensor Patterned Using Self-Assembled Block Copolymer Lithography. *Nano Lett.* **2008**, *8* (11), 3776–3780.

(22) Guenther, M.; Kuckling, D.; Corten, C.; Gerlach, G.; Sorber, J.; Suchaneck, G.; Arndt, K. Chemical Sensors Based on Multiresponsive Block Copolymer Hydrogels. *Sensors Actuators B Chem.* **2007**, *126* (1), 97–106.

(23) Bearzotti, A.; Bertolo, J. M.; Innocenzi, P.; Falcaro, P.; Traversa, E. Humidity Sensors Based on Mesoporous Silica Thin Films Synthesised by Block Copolymers. *J. Eur. Ceram. Soc.* **2004**, *24* (6), 1969–1972.

(24) Jeong, C. K.; Jin, H. M.; Ahn, J.-H.; Park, T. J.; Yoo, H. G.; Koo, M.; Choi, Y.-K.; Kim, S. O.; Lee, K. J. Biosensors: Electrical Biomolecule Detection Using Nanopatterned Silicon via Block Copolymer Lithography (Small 2/2014). *Small* **2014**, *10* (2), 213–213.

(25) Kang, Y.; Walish, J. J.; Gorishnyy, T.; Thomas, E. L. Broad-Wavelength-Range Chemically Tunable Block-Copolymer Photonic Gels. *Nat. Mater.* **2007**, *6* (12), 957–960.

(26) Urbas, A. M.; Maldovan, M.; DeRege, P.; Thomas, E. L. Bicontinuous Cubic Block Copolymer Photonic Crystals. *Adv. Mater.* **2002**, *14* (24), 1850–1853.

(27) Fink, Y.; Urbas, A. M.; Bawendi, M. G.; Joannopoulos, J. D.; Thomas, E. L. Block Copolymers as Photonic Bandgap Materials. *J. Light. Technol.* **1999**, *17* (11), 1963–1969.

(28) Zhang, Q.; Cirpan, A.; Russell, T. P.; Emrick, T. Donor−Acceptor Poly(thiophene- Block -Perylene Diimide) Copolymers: Synthesis and Solar Cell Fabrication. *Macromolecules* **2009**, *42* (4), 1079–1082.

(29) Tao, Y.; McCulloch, B.; Kim, S.; Segalman, R. A. The Relationship between Morphology and Performance of Donor–acceptor Rod–coil Block Copolymer Solar Cells. *Soft Matter* **2009**, *5* (21), 4219.

(30) Crossland, E. J. W.; Nedelcu, M.; Ducati, C.; Ludwigs, S.; Hillmyer, M. A.; Steiner, U.; Snaith, H. J. Block Copolymer Morphologies in Dye-Sensitized Solar Cells: Probing the Photovoltaic Structure-Function Relation. *Nano Lett.* **2009**, *9* (8), 2813–2819.

(31) Kurihara, M.; Kamachi, M.; Stille, J. K. Synthesis of Ionic Block Polymers for Desalination Membranes. *J. Polym. Sci. Polym. Chem. Ed.* **1973**, *11* (3), 587–610.

(32) Metz, S. J.; Potreck, J.; Mulder, M. H. V.; Wessling, M. Water Vapor and Gas Transport through a Poly(butylene Terephthalate) Poly(ethylene Oxide) Block Copolymer. *Desalination* **2002**, *148* (1-3), 303–307.

(33) Ross, C. A.; Berggren, K. K.; Cheng, J. Y.; Jung, Y. S.; Chang, J.-B. Three-Dimensional Nanofabrication by Block Copolymer Self-Assembly. *Adv. Mater.* **2014**, *26* (25), 4386–4396.

(34) Jung, Y. S.; Chang, J. B.; Verploegen, E.; Berggren, K. K.; Ross, C. A. A Path to Ultranarrow Patterns Using Self-Assembled Lithography. *Nano Lett.* **2010**, *10* (3), 1000–1005.

(35) Kennemur, J. G.; Yao, L.; Bates, F. S.; Hillmyer, M. A. Sub-5 Nm Domains in Ordered Poly(cyclohexylethylene)- Block -Poly(methyl Methacrylate) Block Polymers for Lithography. *Macromolecules* **2014**, *47* (4), 1411–1418.

(36) Sinturel, C.; Bates, F. S.; Hillmyer, M. A. High χ − Low N Block Polymers : How Far Can We Go ? *ACS Macro Lett.* **2015**.

(37) Black, C. T.; Guarini, K. W.; Milkove, K. R.; Baker, S. M.; Russell, T. P.;

Tuominen, M. T. Integration of Self-Assembled Diblock Copolymers for Semiconductor Capacitor Fabrication. *Appl. Phys. Lett.* **2001**, *79* (3), 409.

(38) Kim, H.-C.; Park, S.-M.; Hinsberg, W. D. Block Copolymer Based Nanostructures: Materials, Processes, and Applications to Electronics. *Chem. Rev.* **2010**, *110* (1), 146–177.

(39) Delgadillo, P. A. R. Implementation of a Chemo-Epitaxy Flow for Directed Self-Assembly on 300-Mm Wafer Processing Equipment. *J. Micro/Nanolithography, MEMS, MOEMS* **2012**, *11* (3), 031302.

(40) Bates, F. S.; Fredrickson, G. H. Block Copolymer Thermodynamics: Theory and Experiment. *Annu. Rev. Phys. Chem.* **1990**, *41*, 525–557.

(41) Bai, W.; Hannon, A. F.; Gotrik, K. W.; Choi, H. K.; Aissou, K.; Liontos, G.; Ntetsikas, K.; Alexander-Katz, A.; Avgeropoulos, A.; Ross, C. A. Thin Film Morphologies of Bulk-Gyroid Polystyrene- Block - Polydimethylsiloxane under Solvent Vapor Annealing. *Macromolecules* **2014**, *47* (17), 6000–6008.

(42) Jung, Y. S.; Ross, C. A. Solvent-Vapor-Induced Tunability of Self-Assembled Block Copolymer Patterns. *Adv. Mater.* **2009**, *21* (24), 2540–2545.

(43) Lodge, T. P.; Hanley, K. J.; Pudil, B.; Alahapperuma, V. Phase Behavior of Block Copolymers in a Neutral Solvent. *Macromolecules* **2003**, *36* (3), 816–822.

(44) Hanley, K. J.; Lodge, T. P.; Huang, C.-I. Phase Behavior of a Block Copolymer in Solvents of Varying Selectivity. *Macromolecules* **2000**, *33* (16), 5918–5931.

(45) Castelletto, V.; Hamley, I. W. Morphologies of Block Copolymer Melts. *Curr. Opin. Solid State Mater. Sci.* **2004**, *8* (6), 426–438.

(46) Aissou, K.; Choi, H. K.; Nunns, A.; Manners, I.; Ross, C. A. Ordered Nanoscale Archimedean Tilings of a Templated 3-Miktoarm Star Terpolymer. *Nano Lett.* **2013**, *13* (2), 835–839.

(47) Choi, H. K.; Gwyther, J.; Manners, I.; Ross, C. A. Square Arrays of Holes and Dots Patterned from a Linear ABC Triblock Terpolymer. *ACS Nano* **2012**, *6* (9), 8342–8348.

(48) Park, W. I.; Kim, Y.; Jeong, J. W.; Kim, K.; Yoo, J.-K.; Hur, Y. H.; Kim, J. M.; Thomas, E. L.; Alexander-Katz, A.; Jung, Y. S. Host-Guest Self-Assembly in Block Copolymer Blends. *Sci. Rep.* **2013**, *3*, 3190.

(49) Aissou, K.; Nunns, A.; Manners, I.; Ross, C. A. Square and Rectangular Symmetry Tiles from Bulk and Thin Film 3-Miktoarm Star Terpolymers. *Small* **2013**, *9* (23), 4077–4084.

(50) Cheng, J. Y.; Mayes, A. M.; Ross, C. A. Nanostructure Engineering by Templated Self-Assembly of Block Copolymers. *Nat. Mater.* **2004**, *3* (11), 823–828.

(51) Bita, I.; Yang, J. K. W.; Jung, Y. S.; Ross, C. A.; Thomas, E. L.; Berggren, K. K. Graphoepitaxy of Self-Assembled Block Copolymers on Two-Dimensional Periodic Patterned Templates. *Science (80-.).* **2008**, *321*, 939–943.

(52) Son, J. G.; Gwyther, J.; Chang, J.-B.; Berggren, K. K.; Manners, I.; Ross, C. A. Highly Ordered Square Arrays from a Templated ABC Triblock Terpolymer. *Nano Lett.* **2011**, *11* (7), 2849–2855.

(53) Kim, S. O.; Solak, H. H.; Stoykovich, M. P.; Ferrier, N. J.; De Pablo, J. J.; Nealey, P. F. Epitaxial Self-Assembly of Block Copolymers on Lithographically Defined Nanopatterned Substrates. *Nature* **2003**, *424* (6947), 411–414.

(54) Segalman, R. A.; Yokoyama, H.; Kramer, E. J. Graphoepitaxy of Spherical Domain Block Copolymer Films. *Adv. Mater.* **2001**, *13* (15), 1152–1155.

(55) Mansky, P. Controlling Polymer-Surface Interactions with Random Copolymer Brushes. *Science (80-.).* **1997**, *275* (5305), 1458–1460.

(56) Ma, M.; Thomas, E. L.; Rutledge, G. C.; Yu, B.; Li, B.; Jin, Q.; Ding, D.; Shi, A.-C. Gyroid-Forming Diblock Copolymers Confined in Cylindrical Geometry: A Case of Extreme Makeover for Domain Morphology. *Macromolecules* **2010**, *43* (6), 3061–3071.

(57) Wu, Y.; Cheng, G.; Katsov, K.; Sides, S. W.; Wang, J.; Tang, J.; Fredrickson, G. H.; Moskovits, M.; Stucky, G. D. Composite Mesostructures by Nano-Confinement. *Nat. Mater.* **2004**, *3* (11), 816–822.

(58) Hu, H.; Gopinadhan, M.; Osuji, C. O. Directed Self-Assembly of Block Copolymers: A Tutorial Review of Strategies for Enabling Nanotechnology with Soft Matter. *Soft Matter* **2014**, *10* (22), 3867–3889.

(59) Luo, M.; Epps, T. H. Directed Block Copolymer Thin Film Self-Assembly: Emerging Trends in Nanopattern Fabrication. *Macromolecules* **2013**, *46* (19), 7567–7579.

(60) Segalman, R. A. Materials Science. Directing Self-Assembly toward Perfection. *Science* **2008**, *321* (5891), 919–920.

(61) Tavakkoli K G, A.; Gotrik, K. W.; Hannon, A. F.; Alexander-Katz, A.; Ross, C. A.; Berggren, K. K. Templating Three-Dimensional Self-Assembled Structures in Bilayer Block Copolymer Films. *Science* **2012**, *336* (6086), 1294–1298.

(62) Bosworth, J. K.; Paik, M. Y.; Ruiz, R.; Schwartz, E. L.; Huang, J. Q.; Ko, A. W.; Smilgies, D.-M.; Black, C. T.; Ober, C. K. Control of Self-Assembly of Lithographically Patternable Block Copolymer Films. *ACS Nano* **2008**, *2*, 1396–1402.

(63) Tsai, H.; Pitera, J. W.; Miyazoe, H.; Bangsaruntip, S.; Engelmann, S. U.; Liu, C.-C.; Cheng, J. Y.; Bucchignano, J. J.; Klaus, D. P.; Joseph, E. A.; Sanders, D. P.; Colburn, M. E.; Guillorn, M. A. Two-Dimensional Pattern Formation Using Graphoepitaxy of PS-B-PMMA Block Copolymers for

Advanced FinFET Device and Circuit Fabrication. *ACS Nano* **2014**, *8* (5), 5227–5232.

(64) Sundrani, D.; Darling, S. B.; Sibener, S. J. Guiding Polymers to Perfection: Macroscopic Alignment of Nanoscale Domains. *Nano Lett.* **2004**, *4* (2), 273–276.

(65) Segalman, R. A.; Hexemer, A.; Kramer, E. J. Effects of Lateral Confinement on Order in Spherical Domain Block Copolymer Thin Films. *Macromolecules* **2003**, *36* (18), 6831–6839.

(66) Ruiz, R.; Kang, H.; Detcheverry, F. A.; Dobisz, E.; Kercher, D. S.; Albrecht, T. R.; de Pablo, J. J.; Nealey, P. F. Density Multiplication and Improved Lithography by Directed Block Copolymer Assembly. *Science* **2008**, *321* (5891), 936–939.

(67) Stoykovich, M. P. Directed Assembly of Block Copolymer Blends into Nonregular Device-Oriented Structures. *Science (80-.).* **2005**, *308* (5727), 1442–1446.

(68) Cheng, J. Y.; Rettner, C. T.; Sanders, D. P.; Kim, H.-C.; Hinsberg, W. D. Dense Self-Assembly on Sparse Chemical Patterns: Rectifying and Multiplying Lithographic Patterns Using Block Copolymers. *Adv. Mater.* **2008**, *20* (16), 3155–3158.

(69) Hannon, A. F.; Ding, Y.; Bai, W.; Ross, C. A.; Alexander-Katz, A. Optimizing Topographical Templates for Directed Self-Assembly of Block Copolymers via Inverse Design Simulations. *Nano Lett.* **2014**, *14* (1), 318–325.

(70) Hannon, A. F.; Gotrik, K. W.; Ross, C. A.; Alexander-Katz, A. Inverse Design of Topographical Templates for Directed Self-Assembly of Block Copolymers. *ACS Macro Lett.* **2013**, *2* (3), 251–255.

(71) Chang, J.-B.; Choi, H. K.; Hannon, A. F.; Alexander-Katz, A.; Ross, C. A.; Berggren, K. K. Design Rules for Self-Assembled Block Copolymer Patterns Using Tiled Templates. *Nat. Commun.* **2014**, *5*, 3305.

(72) Khaira, G. S.; Qin, J.; Garner, G. P.; Xiong, S.; Wan, L.; Ruiz, R.; Jaeger, H. M.; Nealey, P. F.; de Pablo, J. J. Evolutionary Optimization of Directed Self-Assembly of Triblock Copolymers on Chemically Patterned Substrates. *ACS Macro Lett.* **2014**, *3* (8), 747–752.

(73) Liu, C.-C.; Nealey, P. F.; Raub, A. K.; Hakeem, P. J.; Brueck, S. R. J.; Han, E.; Gopalan, P. Integration of Block Copolymer Directed Assembly with 193 Immersion Lithography. *J. Vac. Sci. Technol. B Microelectron. Nanom. Struct.* **2010**, *28* (6), C6B30.

(74) Jeong, S.-J.; Xia, G.; Kim, B. H.; Shin, D. O.; Kwon, S.-H.; Kang, S.-W.; Kim, S. O. Universal Block Copolymer Lithography for Metals, Semiconductors, Ceramics, and Polymers. *Adv. Mater.* **2008**, *20* (10), 1898–1904.

(75) Cheng, J. Y.; Sanders, D. P.; Truong, H. D.; Harrer, S.; Friz, A.; Holmes,

S.; Colburn, M.; Hinsberg, W. D. Simple and Versatile Methods to Integrate Directed Self-Assembly with Optical Lithography Using a Polarity-Switched Photoresist. *ACS Nano* **2010**, *4* (8), 4815–4823.

(76) Yang, J. K. W.; Jung, Y. S.; Chang, J.-B.; Mickiewicz, R. A.; Alexander-Katz, A.; Ross, C. A.; Berggren, K. K. Complex Self-Assembled Patterns Using Sparse Commensurate Templates with Locally Varying Motifs. *Nat. Nanotechnol.* **2010**, *5* (4), 256–260.

(77) Jung, Y. S.; Ross, C. A. Orientation-Controlled Self-Assembled Nanolithography Using a Polystyrene-Polydimethylsiloxane Block Copolymer. *Nano Lett.* **2007**, *7* (7), 2046–2050.

(78) Stoykovich, M. P.; Müller, M.; Kim, S. O.; Solak, H. H.; Edwards, E. W.; de Pablo, J. J.; Nealey, P. F. Directed Assembly of Block Copolymer Blends into Nonregular Device-Oriented Structures. *Science (80-.).* **2005**, *308* (5727), 1442–1446.

(79) Bates, C. M.; Seshimo, T.; Maher, M. J.; Durand, W. J.; Cushen, J. D.; Dean, L. M.; Blachut, G.; Ellison, C. J.; Willson, C. G. Polarity-Switching Top Coats Enable Orientation of Sub-10-Nm Block Copolymer Domains. *Science (80-.).* **2012**, *338*, 775–779.

(80) Kim, E.; Kim, W.; Lee, K. H.; Ross, C. A.; Son, J. G. A Top Coat with Solvent Annealing Enables Perpendicular Orientation of Sub-10 Nm Microdomains in Si-Containing Block Copolymer Thin Films. *Adv. Funct. Mater.* **2014**, 6981–6988.

(81) Hong, S. W.; Gu, W.; Huh, J.; Sveinbjornsson, B. R.; Jeong, G.; Grubbs, R. H.; Russell, T. P. On the Self-Assembly of Brush Block Copolymers in Thin Films. *ACS Nano* **2013**, *7* (11), 9684–9692.

(82) Olszowka, V.; Hund, M.; Kuntermann, V.; Scherdel, S.; Tsarkova, L.; Böker, A. Electric Field Alignment of a Block Copolymer Nanopattern: Direct Observation of the Microscopic Mechanism. *ACS Nano* **2009**, *3* (5), 1091–1096.

(83) Amundson, K.; Helfand, E.; Quan, X.; Smith, S. D. Alignment of Lamellar Block Copolymer Microstructure in an Electric Field. 1. Alignment Kinetics. *Macromolecules* **1993**, *26* (11), 2698–2703.

(84) Thurn-Albrecht, T.; DeRouchey, J.; Russell, T. P.; Kolb, R. Pathways toward Electric Field Induced Alignment of Block Copolymers. *Macromolecules* **2002**, *35* (21), 8106–8110.

(85) Osuji, C.; Ferreira, P. J.; Mao, G.; Ober, C. K.; Vander Sande, J. B.; Thomas, E. L. Alignment of Self-Assembled Hierarchical Microstructure in Liquid Crystalline Diblock Copolymers Using High Magnetic Fields. *Macromolecules* **2004**, *37* (26), 9903–9908.

(86) Bodycomb, J.; Funaki, Y.; Kimishima, K.; Hashimoto, T. Single-Grain Lamellar Microdomain from a Diblock Copolymer. *Macromolecules* **1999**, *32* (6), 2075–2077.

(87) Singh, G.; Yager, K. G.; Berry, B.; Kim, H.-C.; Karim, A. Dynamic Thermal Field-Induced Gradient Soft-Shear for Highly Oriented Block Copolymer Thin Films. *ACS Nano* **2012**, *6* (11), 10335–10342.

(88) Hashimoto, T.; Bodycomb, J.; Funaki, Y.; Kimishima, K. The Effect of Temperature Gradient on the Microdomain Orientation of Diblock Copolymers Undergoing an Order−Disorder Transition. *Macromolecules* **1999**, *32* (3), 952–954.

(89) Son, J. G.; Gotrik, K. W.; Ross, C. A. High-Aspect-Ratio Perpendicular Orientation of PS- B -PDMS Thin Films under Solvent Annealing. *ACS Macro Lett.* **2012**, *1* (11), 1279–1284.

(90) Cui, G.; Fujikawa, M.; Nagano, S.; Shimokita, K.; Miyazaki, T.; Sakurai, S.; Yamamoto, K. Macroscopic Alignment of Cylinders via Directional Coalescence of Spheres along Annealing Solvent Permeation Directions in Block Copolymer Thick Films. *Macromolecules* **2014**, *47* (17), 5989–5999.

(91) Angelescu, D. E.; Waller, J. H.; Adamson, D. H.; Deshpande, P.; Chou, S. Y.; Register, R. A.; Chaikin, P. M. Macroscopic Orientation of Block Copolymer Cylinders in Single-Layer Films by Shearing. *Adv. Mater.* **2004**, *16* (19), 1736–1740.

(92) Fredrickson, G. H. Steady Shear Alignment of Block Copolymers near the Isotropic–lamellar Transition. *J. Rheol. (N. Y. N. Y).* **1994**, *38* (4), 1045.

(93) Patel, S. S.; Larson, R. G.; Winey, K. I.; Watanabe, H. Shear Orientation and Rheology of a Lamellar Polystyrene-Polyisoprene Block Copolymer. *Macromolecules* **1995**, *28* (12), 4313–4318.

(94) Tang, C.; Wu, W.; Smilgies, D.-M.; Matyjaszewski, K.; Kowalewski, T. Robust Control of Microdomain Orientation in Thin Films of Block Copolymers by Zone Casting. *J. Am. Chem. Soc.* **2011**, *133* (30), 11802–11809.

(95) Onses, M. S.; Ramírez-Hernández, A.; Hur, S.-M.; Sutanto, E.; Williamson, L.; Alleyne, A. G.; Nealey, P. F.; de Pablo, J. J.; Rogers, J. A. Block Copolymer Assembly on Nanoscale Patterns of Polymer Brushes Formed by Electrohydrodynamic Jet Printing. *ACS Nano* **2014**, *8* (7), 6606–6613.

(96) Hu, H.; Choo, Y.; Feng, X.; Osuji, C. O. Physical Continuity and Vertical Alignment of Block Copolymer Domains by Kinetically Controlled Electrospray Deposition. *Macromol. Rapid Commun.* **2015**, *36* (13), 1290–1296.

(97) Zhao, D. Triblock Copolymer Syntheses of Mesoporous Silica with Periodic 50 to 300 Angstrom Pores. *Science (80-.).* **1998**, *279* (5350), 548–552.

(98) Yang, P.; Zhao, D.; Margolese, D. I.; Chmelka, B. F.; Stucky, G. D. Block Copolymer Templating Syntheses of Mesoporous Metal Oxides with Large Ordering Lengths and Semicrystalline Framework. *Chem. Mater.* **1999**, *11*

(10), 2813–2826.

(99) Hedrick, J. L.; Miller, R. D.; Hawker, C. J.; Carter, K. R.; Volksen, W.; Yoon, D. Y.; Trollsås, M. Templating Nanoporosity in Thin-Film Dielectric Insulators. *Adv. Mater.* **1998**, *10* (13), 1049–1053.

(100) Yang, S. Y.; Park, J.; Yoon, J.; Ree, M.; Jang, S. K.; Kim, J. K. Virus Filtration Membranes Prepared from Nanoporous Block Copolymers with Good Dimensional Stability under High Pressures and Excellent Solvent Resistance. *Adv. Funct. Mater.* **2008**, *18* (9), 1371–1377.

(101) Guo, C.; Lin, Y.-H.; Witman, M. D.; Smith, K. A.; Wang, C.; Hexemer, A.; Strzalka, J. W.; Gomez, E. D.; Verduzco, R. Conjugated Block Copolymer Photovoltaics with near 3% Efficiency through Microphase Separation. *Nano Lett.* **2013**.

(102) Sun, S.-S. Design of a Block Copolymer Solar Cell. *Sol. Energy Mater. Sol. Cells* **2003**, *79* (2), 257–264.

(103) Javier, A. E.; Patel, S. N.; Hallinan, D. T.; Srinivasan, V.; Balsara, N. P. Simultaneous Electronic and Ionic Conduction in a Block Copolymer: Application in Lithium Battery Electrodes. *Angew. Chem. Int. Ed. Engl.* **2011**, *50* (42), 9848–9851.

(104) Orilall, M. C.; Wiesner, U. Block Copolymer Based Composition and Morphology Control in Nanostructured Hybrid Materials for Energy Conversion and Storage: Solar Cells, Batteries, and Fuel Cells. *Chem. Soc. Rev.* **2011**, *40* (2), 520–535.

(105) Böker, A.; Elbs, H.; Hänsel, H.; Knoll, A.; Ludwigs, S.; Zettl, H.; Urban, V.; Abetz, V.; Müller, A. H. E.; Krausch, G. Microscopic Mechanisms of Electric-Field-Induced Alignment of Block Copolymer Microdomains. *Phys. Rev. Lett.* **2002**, *89* (13), 135502.

(106) Jung, Y. S.; Lee, J. H.; Lee, J. Y.; Ross, C. a. Fabrication of Diverse Metallic Nanowire Arrays Based on Block Copolymer Self-Assembly. *Nano Lett.* **2010**, *10* (9), 3722–3726.

(107) Hamley, I. W. Nanostructure Fabrication Using Block Copolymers. *Nanotechnology* **2003**, *14* (10), R39–R54.

(108) Tu, K.-H.; Bai, W.; Liontos, G.; Ntetsikas, K.; Avgeropoulos, A.; Ross, C. A. Universal Pattern Transfer Methods for Metal Nanostructures by Block Copolymer Lithography. *Nanotechnology* **2015**, *26* (37), 375301.

(109) Park, M.; Harrison, C.; Chaikin, P. M.; Register, R. A.; Adamson, D. H. Block Copolymer Lithography: Periodic Arrays of 1011 Holes in 1 Square Centimeter. *Science (80-.).* **1997**, *276* (5317), 1401–1404.

(110) Segalman, R. a. Patterning with Block Copolymer Thin Films. *Mater. Sci. Eng. R Reports* **2005**, *48* (6), 191–226.

(111) Cheng, J. Y.; Ross, C. A.; Chan, V. Z.-H.; Thomas, E. L.; Lammertink, R. G. H.; Vancso, G. J. Formation of a Cobalt Magnetic Dot Array via Block Copolymer Lithography. *Adv. Mater.* **2001**, *13* (15), 1174–1178.

(112) Thurn-Albrecht, T. Ultrahigh-Density Nanowire Arrays Grown in Self-Assembled Diblock Copolymer Templates. *Science (80-.).* **2000**, *290*, 2126–2129.

(113) Black, C. T.; Guarini, K. W.; Sandstrom, R. L.; Yeung, S.; Zhang, Y. Formation of Nanometer-Scale Dot Arrays from Diblock Copolymer Templates. *MRS Proc.* **2002**, *728*, S4.9.

(114) Kim, J. Y.; Kim, B. H.; Hwang, J. O.; Jeong, S.-J.; Shin, D. O.; Mun, J. H.; Choi, Y. J.; Jin, H. M.; Kim, S. O. Flexible and Transferrable Self-Assembled Nanopatterning on Chemically Modified Graphene. *Adv. Mater.* **2013**, *25* (9), 1331–1335.

(115) Rose, F.; Bosworth, J. K.; Dobisz, E. A.; Ruiz, R. Three-Dimensional Mesoporous Structures Fabricated by Independent Stacking of Self-Assembled Films on Suspended Membranes. *Nanotechnology* **2011**, *22* (3), 035603.

(116) Jeong, J. W.; Hur, Y. H.; Kim, H.-J.; Kim, J. M.; Park, W. I.; Kim, M. J.; Kim, B. J.; Jung, Y. S. Proximity Injection of Plasticizing Molecules to Self-Assembling Polymers for Large-Area, Ultrafast Nanopatterning in the Sub-10-Nm Regime. *ACS Nano* **2013**, *7* (8), 6747–6757.

(117) Majewski, P. W.; Rahman, A.; Black, C. T.; Yager, K. G. Arbitrary Lattice Symmetries via Block Copolymer Nanomeshes. *Nat. Commun.* **2015**, *6*, 7448.

(118) Son, J. G.; Hannon, A. F.; Gotrik, K. W.; Alexander-Katz, A.; Ross, C. A. Hierarchical Nanostructures by Sequential Self-Assembly of Styrene-Dimethylsiloxane Block Copolymers of Different Periods. *Adv. Mater.* **2011**, *23* (5), 634–639.

(119) Hong, S. W.; Huh, J.; Gu, X.; Lee, D. H.; Jo, W. H.; Park, S.; Xu, T.; Russell, T. P. Unidirectionally Aligned Line Patterns Driven by Entropic Effects on Faceted Surfaces. *Proc. Natl. Acad. Sci. U. S. A.* **2012**, *109* (5), 1402–1406.

(120) Tavakkoli, A. K. G.; Nicaise, S. M.; Hannon, A. F.; Gotrik, K. W.; Alexander-Katz, A.; Ross, C. A.; Berggren, K. K. Sacrificial-Post Templating Method for Block Copolymer Self-Assembly. *Small* **2014**, *10* (3), 493–499, 418.

(121) Shin, D. O.; Mun, J. H.; Hwang, G.-T.; Yoon, J. M.; Kim, J. Y.; Yun, J. M.; Yang, Y.-B.; Oh, Y.; Lee, J. Y.; Shin, J.; Lee, K. J.; Park, S.; Kim, J. U.; Kim, S. O. Multicomponent Nanopatterns by Directed Block Copolymer Self-Assembly. *ACS Nano* **2013**, *7* (10), 8899–8907.

(122) Xiang, H.; Shin, K.; Kim, T.; Moon, S. I.; McCarthy, T. J.; Russell, T. P. Block Copolymers under Cylindrical Confinement. *Macromolecules* **2004**, *37* (15), 5660–5664.

(123) Xiang, H.; Shin, K.; Kim, T.; Moon, S.; Mccarthy, T. J.; Russell, T. P. The Influence of Confinement and Curvature on the Morphology of Block

Copolymers. *J. Polym. Sci. Part B Polym. Phys.* **2005**, *43* (23), 3377–3383.

(124) Zhao, D.; Feng, J.; Huo, Q.; Melosh, N.; Fredrickson, G.; Chmelka, B.; Stucky, G. Triblock Copolymer Syntheses of Mesoporous Silica with Periodic 50 to 300 Angstrom Pores. *Science* **1998**, *279* (5350), 548–552.

(125) Vignolini, S.; Yufa, N. A.; Cunha, P. S.; Guldin, S.; Rushkin, I.; Stefik, M.; Hur, K.; Wiesner, U.; Baumberg, J. J.; Steiner, U. A 3D Optical Metamaterial Made by Self-Assembly. *Adv. Mater.* **2012**, *24* (10), OP23–OP27.

(126) Peng, Q.; Tseng, Y.-C.; Darling, S. B.; Elam, J. W. Nanoscopic Patterned Materials with Tunable Dimensions via Atomic Layer Deposition on Block Copolymers. *Adv. Mater.* **2010**, *22* (45), 5129–5133.

(127) Mendoza, C.; Pietsch, T.; Gutmann, J. S.; Jehnichen, D.; Gindy, N.; Fahmi, A. Block Copolymers with Gold Nanoparticles: Correlation between Structural Characteristics and Mechanical Properties. *Macromolecules* **2009**, *42* (4), 1203–1211.

(128) Warren, S. C.; Messina, L. C.; Slaughter, L. S.; Kamperman, M.; Zhou, Q.; Gruner, S. M.; DiSalvo, F. J.; Wiesner, U. Ordered Mesoporous Materials from Metal Nanoparticle-Block Copolymer Self-Assembly. *Science* **2008**, *320* (5884), 1748–1752.

(129) Kao, J.; Thorkelsson, K.; Bai, P.; Zhang, Z.; Sun, C.; Xu, T. Rapid Fabrication of Hierarchically Structured Supramolecular Nanocomposite Thin Films in One Minute. *Nat. Commun.* **2014**, *5*, 4053.

(130) Tseng, Y.-C.; Darling, S. B. Block Copolymer Nanostructures for Technology. *Polymers (Basel).* **2010**, *2* (4), 470–489.

(131) Jung, Y. S.; Jung, W.; Ross, C. A. Nanofabricated Concentric Ring Structures by Templated Self-Assembly of a Diblock Copolymer. *Nano Lett.* **2008**, *8* (9), 2975–2981.

(132) Jung, Y. S.; Ross, C. A. Well-Ordered Thin-Film Nanopore Arrays Formed Using a Block-Copolymer Template. *Small* **2009**, *5* (14), 1654–1659.

(133) Yang, X.; Xiao, S.; Hsu, Y.; Lee, K. Directed Self-Assembly of Block Copolymer for Bit Patterned Mediawith Areal Density Beyond1 Teradot / Inch 2. *J. Nanomater.* **2013**, *2013* (615896), 1–22.

(134) Lim, H. S.; Lee, J.-H.; Walish, J. J.; Thomas, E. L. Dynamic Swelling of Tunable Full-Color Block Copolymer Photonic Gels via Counterion Exchange. *ACS Nano* **2012**, *6* (10), 8933–8939.

(135) Checco, A.; Rahman, A.; Black, C. T. Robust Superhydrophobicity in Large-Area Nanostructured Surfaces Defined by Block-Copolymer Self Assembly. *Adv. Mater.* **2014**, *26* (6), 886–891.

(136) Rahman, A.; Ashraf, A.; Xin, H.; Tong, X.; Sutter, P.; Eisaman, M. D.; Black, C. T. Sub-50-Nm Self-Assembled Nanotextures for Enhanced Broadband Antireflection in Silicon Solar Cells. *Nat. Commun.* **2015**, *6*, 5963.

(137) Thorkelsson, K.; Mastroianni, A. J.; Ercius, P.; Xu, T. Direct Nanorod Assembly Using Block Copolymer-Based Supramolecules. *Nano Lett.* **2012**, *12* (1), 498–504.

(138) Park, W. I.; You, B. K.; Mun, B. H.; Seo, H. K.; Lee, J. Y.; Hosaka, S.; Yin, Y.; Ross, C. A.; Lee, K. J.; Jung, Y. S. Self-Assembled Incorporation of Modulated Block Copolymer Nanostructures in Phase-Change Memory for Switching Power Reduction. *ACS Nano* **2013**, *7* (3), 2651–2658.

(139) Son, J. G.; Son, M.; Moon, K.-J.; Lee, B. H.; Myoung, J.-M.; Strano, M. S.; Ham, M.-H.; Ross, C. A. Sub-10 Nm Graphene Nanoribbon Array Field-Effect Transistors Fabricated by Block Copolymer Lithography. *Adv. Mater.* **2013**, *25* (34), 4723–4728.

(140) Hsueh, H.-Y.; Chen, H.-Y.; Hung, Y.-C.; Ling, Y.-C.; Gwo, S.; Ho, R.-M. Well-Defined Multibranched Gold with Surface Plasmon Resonance in near-Infrared Region from Seeding Growth Approach Using Gyroid Block Copolymer Template. *Adv. Mater.* **2013**, *25* (12), 1780–1786.

(141) Phillip, W. A.; Dorin, R. M.; Werner, J.; Hoek, E. M. V; Wiesner, U.; Elimelech, M. Tuning Structure and Properties of Graded Triblock Terpolymer-Based Mesoporous and Hybrid Films. *Nano Lett.* **2011**, *11* (7), 2892–2900.

(142) Black, C. T. Self-Aligned Self Assembly of Multi-Nanowire Silicon Field Effect Transistors. *Appl. Phys. Lett.* **2005**, *87* (16), 163116.

(143) Black, C. T.; Guarini, K. W.; Zhang, Y.; Kim, H.; Benedict, J.; Sikorski, E.; Babich, I. V.; Milkove, K. R. High-Capacity, Self-Assembled Metal–Oxide–Semiconductor Decoupling Capacitors. *IEEE Electron Device Lett.* **2004**, *25* (9), 622–624.

(144) Mun, B. H.; You, B. K.; Yang, S. R.; Yoo, H. G.; Kim, J. M.; Park, W. I.; Yin, Y.; Byun, M.; Jung, Y. S.; Lee, K. J. Flexible One Diode-One Phase Change Memory Array Enabled by Block Copolymer Self-Assembly. *ACS Nano* **2015**, *9* (4), 4120–4128.

(145) You, B. K.; Park, W. I.; Kim, J. M.; Park, K.-I.; Seo, H. K.; Lee, J. Y.; Jung, Y. S.; Lee, K. J. Reliable Control of Filament Formation in Resistive Memories by Self-Assembled Nanoinsulators Derived from a Block Copolymer. *ACS Nano* **2014**, *8* (9), 9492–9502.

(146) Jeong, C. K.; Baek, K. M.; Niu, S.; Nam, T. W.; Hur, Y. H.; Park, D. Y.; Hwang, G.-T.; Byun, M.; Wang, Z. L.; Jung, Y. S.; Lee, K. J. Topographically-Designed Triboelectric Nanogenerator via Block Copolymer Self-Assembly. *Nano Lett.* **2014**, *14* (12), 7031–7038.

(147) Hajduk, D. A.; Harper, P. E.; Gruner, S. M.; Honeker, C. C.; Kim, G.; Thomas, E. L.; Fetters, L. J. The Gyroid: A New Equilibrium Morphology in Weakly Segregated Diblock Copolymers. *Macromolecules* **1994**, *27* (15), 4063–4075.

(148) Sveinbjörnsson, B. R.; Weitekamp, R. A.; Miyake, G. M.; Xia, Y.;

Atwater, H. A.; Grubbs, R. H. Rapid Self-Assembly of Brush Block Copolymers to Photonic Crystals. *Proc. Natl. Acad. Sci. U. S. A.* **2012**, *109* (36), 14332–14336.

(149) Adams, M. L.; Lavasanifar, A.; Kwon, G. S. Amphiphilic Block Copolymers for Drug Delivery. *J. Pharm. Sci.* **2003**, *92* (7), 1343–1355.

(150) Jackson, E. A.; Hillmyer, M. A. Nanoporous Membranes Derived from Block Copolymers: From Drug Delivery to Water Filtration. *ACS Nano* **2010**, *4* (7), 3548–3553.

(151) Dorin, R. M.; Sai, H.; Wiesner, U. Hierarchically Porous Materials from Block Copolymers. *Chem. Mater.* **2014**, *26* (1), 339–347.

(152) Yang, S. Y.; Ryu, I.; Kim, H. Y.; Kim, J. K.; Jang, S. K.; Russell, T. P. Nanoporous Membranes with Ultrahigh Selectivity and Flux for the Filtration of Viruses. *Adv. Mater.* **2006**, *18* (6), 709–712.

(153) Singh, G.; Batra, S.; Zhang, R.; Yuan, H.; Yager, K. G.; Cakmak, M.; Berry, B.; Karim, A. Large-Scale Roll-to-Roll Fabrication of Vertically Oriented Block Copolymer Thin Films. *ACS Nano* **2013**, *7* (6), 5291–5299.

(154) Balazs, A. C.; Emrick, T.; Russell, T. P. Nanoparticle Polymer Composites: Where Two Small Worlds Meet. *Science* **2006**, *314* (5802), 1107–1110.

(155) Bockstaller, M. R.; Mickiewicz, R. A.; Thomas, E. L. Block Copolymer Nanocomposites: Perspectives for Tailored Functional Materials. *Adv. Mater.* **2005**, *17* (11), 1331–1349.

(156) Chiu, J. J.; Kim, B. J.; Kramer, E. J.; Pine, D. J. Control of Nanoparticle Location in Block Copolymers. *J. Am. Chem. Soc.* **2005**, *127* (14), 5036–5037.

(157) Guldin, S.; Kolle, M.; Stefik, M.; Langford, R.; Eder, D.; Wiesner, U.; Steiner, U. Tunable Mesoporous Bragg Reflectors Based on Block-Copolymer Self-Assembly. *Adv. Mater.* **2011**, *23* (32), 3664–3668.

(158) Edrington, A. C.; Urbas, A. M.; DeRege, P.; Chen, C. X.; Swager, T. M.; Hadjichristidis, N.; Xenidou, M.; Fetters, L. J.; Joannopoulos, J. D.; Fink, Y.; Thomas, E. L. Polymer-Based Photonic Crystals. *Adv. Mater.* **2001**, *13* (6), 421–425.

(159) Gu, Z.; Kanto, T.; Tsuchiya, K.; Shimomura, T.; Ogino, K. Annealing Effect on Performance and Morphology of Photovoltaic Devices Based on poly(3-Hexylthiophene)-B-Poly(ethylene Oxide). *J. Polym. Sci. Part A Polym. Chem.* **2011**, *49* (12), 2645–2652.

(160) Botiz, I.; Darling, S. B. Self-Assembly of Poly(3-Hexylthiophene)- Block - Polylactide Block Copolymer and Subsequent Incorporation of Electron Acceptor Material. *Macromolecules* **2009**, *42* (21), 8211–8217.

(161) Darling, S. B. Block Copolymers for Photovoltaics. *Energy Environ. Sci.* **2009**, *2* (12), 1266.

Chapter 3: Thin Film Morphologies of Bulk-Gyroid Polystyrene-block-Polydimethylsiloxane under Solvent Vapor Annealing

3.1 Abstract

In this chapter, we investigate the thin film self-assembly of a PS-PDMS block copolymer showing the influence of film thickness, solvent composition ratio, and swelling ratio. Thin film morphologies of a 75.5 kg/mol polystyrene-block-polydimethylsiloxane (PS-*b*-PDMS) diblock copolymer subject to solvent vapor annealing are described. The PS-*b*-PDMS has a double-gyroid morphology in bulk, but as a thin film the morphology can form spheres, cylinders, perforated lamellae or gyroids, depending on the film thickness, its commensurability with the microdomain period, and the ratio of toluene:heptane vapors used for the solvent annealing process. The morphologies are described by self-consistent field theory simulations. Thin film structures with excellent long-range order were produced, which are promising for nanopatterning applications. This work was published in Ref. [1].

3.2 Introduction

Solvent annealing provides a convenient process for controlling microphase separation in block copolymer thin films.[2–4] The film thickness during solvent annealing (both as-cast and swelled with solvent) is an important factor in determining the film morphology,[5] and combinations of film thickness, substrate chemistry and a nonpreferential solvent control morphological transitions, such as the gyroid-lamellar transition in a bulk-gyroid triblock terpolymer film.[6] Other studies have shown that surface energy plays a role in gyroid-cylinder transitions in bulk-gyroid films over 100 nm thick,[7] and solvent removal rate determines the orientation of cylindrical microdomains.[8] Selective solvent annealing can produce diverse thin film morphologies from a given block copolymer because selective solvents change both the effective interaction parameter and the volume fraction of the block copolymer thin film system.[2,9] Therefore, during solvent vapor annealing, the film morpology will depend on not only the as-cast film thickness, but also on the solvent composition and the swelling of the film exposed to the solvent vapor.

Most work on block copolymer films has focussed on bulk lamellar, cylindrical or spherical morphology diblock copolymers, but gyroid structures also form over a narrow compositional range in bulk.[10–17] Bulk gyroid block copolymers have been investigated in cylindrical confinements,[18] but there have been only a few studies of the thin film morphology of solvent-annealed bulk gyroid block copolymers.[32,33] Transitions between gyroids and other morphologies have been observed for a variety of block copolymer compositions.[44,32,33]

Here we present a study of the self-assembly of thin films of a solvent-annealed bulk-gyroid polystyrene-*block*-polydimethylsiloxane (PS-*b*-PDMS (SD75), M_w=75.5 kg/mol) by fine-tuning both the solvent mixture and the film thickness. PS-*b*-PDMS is useful for nanolithography applications due to the high etch selectivity between the PS and PDMS blocks,[4,20,21] the etch resistance of the PDMS block, and the high χ parameter ($\chi_{PS\text{-}PDMS} \sim$ 0.27 at room temperature,[20] though a recent analysis[22] suggests a lower value of 0.14). The molecular weight used here is greater than that of PS-*b*-PDMS used for previous thin film studies.[4] Spun-cast films were solvent vapor annealed in a chamber containing a volume of a liquid solvent mixture. We show that, by selection of the solvent mix ratio, swelling ratio and as-spun film thickness, in-plane cylinders (period ~ 60 nm), perforated lamellae (period ~ 96 nm) or spheres (period ~ 66 nm) with excellent long range order, as well as coexisting morphologies such as lamellae plus cylinders, could be produced. The morphologies are modeled using self-consistent field theory simulations.

3.3 Materials and Methods

Thin films of SD75 were spin-cast from 1wt.% solution in cyclohexane at various spin speeds to control the film thickness. Substrates consisted of oxidized silicon which was chemically functionalized with hydroxyl-terminated polydimethylsiloxane (1 kg mol^{-1}, ~2 nm thick), which corresponds to the minority block of the SD75 block copolymer. The initial film thickness and the thickness during solvent annealing were determined using reflectometry (Filmetrics F20).[23]

Solvent vapor annealing of the block copolymer thin film was done using a range of volumetric mixtures of toluene and heptane (1:0, 10:1, 5:1, 4:1, 3:1, 2.5:1, and 1.5:1) in a solvent reservoir annealing system consisting of a closed chamber of volume 80 cm^3 with a loosely fitted lid that allowed the vapor to leak out slowly. The sample was placed in the chamber supported above 6 cm^3 of liquid solvent. The solvent vapor annealing was carried out at room temperature, 23 ˚C ± 2˚C with humidity 83%. The swelling ratio of the film resulting from each solvent mixture could be varied by using different chambers and lids, which affected the amount of exchange between the solvent and the ambient and therefore affected the partial pressures during anneal. The solvent anneal process was monitored by continuous measurements of the swelled film thickness. After solvent-annealing for times of 3 hours or more under an approximately steady state vapor atmosphere, the film was deswelled over 20 min by sliding open the lid of the chamber in four steps of equal area, one step every 5 min. Based on the time to fully evaporate the solvent for each position of the lid, each step increased the evaporation rate by ~3 cm^3 of solvent/min.

The toluene-heptane system is not an ideal mixture so the ratio of vapor pressures above the liquid mixture is different from the volume fractions of the liquids[2]. The expected vapor pressures for the 1:0, 10:1, 5:1, 4:1, 3:1, 2.5:1, 1.5:1 toluene:heptane volume mixtures at room temperature is described in the supplementary information (section 2(c) and Table S1).

After annealing, a short 5 s CF_4 reactive ion etch was usually performed to remove the surface layer of PDMS that formed due to the low surface energy of PDMS. Then an oxygen plasma treatment removed the PS and converted the self-assembled PDMS microdomains to an immobilized silica-rich topographical pattern which could be imaged by scanning electron microscopy.[24]

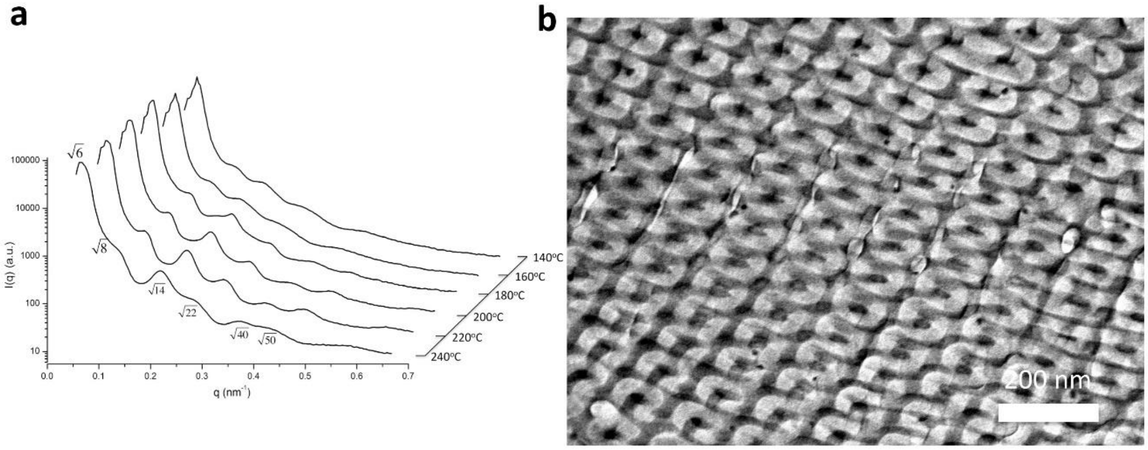

Figure 3.1. (a): Small angle X-ray scattering plots of intensity I(q) vs. q in nm^{-1} for the SD75 sample at a range of temperatures from 140˚C to 240˚C. The horizontal scales are offset for clarity with the main peak appearing at 0.1 nm^{-1}. (b): TEM image of the bulk morphology of SD75 corresponding to a double gyroid structure. Fig. 3.1a was provided by Dr. Karim Aissou. Fig. 3.1b was provided by Prof. Apostolos Avgeropolos

3.4 Bulk morphology

The PS-b-PDMS used here (labeled SD75) has a total molecular weight (M_w) of 75.5 kg mol^{-1}, polydispersity index (PDI) of 1.04, PDMS volume fraction $f_{PDMS} = 0.415$, $N = 847$, and $\chi N \cong 229$ at room temperature based on the value of $\chi_{PS\text{-}PDMS} = 0.27$. It was synthesized by a procedure described by Bellas et al.[25] Figure 3.1a is a synchrotron small angle x-ray scattering (SAXS) profile of a bulk sample of SD75 measured at different temperatures. The SAXS profile shows the existence of one main peak and higher-order peaks with positions $(q/q_{100})^2 = 6, 8, 14, \ldots, 100, \ldots$ The scattering vector q is defined by $q=4\pi\sin\theta/\lambda$, with scattering angle 2θ and x-ray wavelength λ, and corresponds to a real space periodicity of $4\pi/q$. This sequence of peaks corresponds to a double gyroid (DG) structure with the cubic $Ia\bar{3}d$ space group having a domain spacing d_{211} = 61 nm from the first peak, and cubic unit cell parameter of 150 nm. These parameters are in agreement with prior measurements[11] on the same bulk SD75. TEM images of bulk unstained SD75 exemplified by Figure 3.1b shows morphology consistent with a double gyroid structure.[10]

3.5 Film morphology as a function of as-cast film thickness

The solvent annealing process used to process thin films of SD75 is described in detail in the Methods section. The samples were annealed in a chamber containing a reservoir of liquid solvent and the partial vapor pressure was varied by changing the leak rate of the chamber. The swelled thickness of the block copolymer films was monitored by optical reflectometry. To evaluate the influence of as-cast film thickness on the morphology, films were annealed under a vapor from a toluene:heptane 3:1 volumetric mixture for 3 hours. The partial pressures are expected to be P_{tol} = 10.37 Torr, P_{hep} = 6.29 Torr at 23 °C above the non-ideal solvent mixture[2] (supplementary information (SI) section 2(c)). Under this anneal condition all films swelled to 2.1 - 2.2 times the initial film thickness. Due to the high χN of the SD75 (N is the total number of chemical repeat units, in which C_8H_8 is the repeat unit of Polystyrene, $SiOC_2H_6$ is the repeat unit of Polydimethylsiloxane), the swollen films are expected to be be below the order-disorder temperature (ODT) when the solvent concentration is below ~60%.[16,26] This suggests that even in the swelled state the films are below the ODT during our experiments. Microphase separation therefore occurs while the film is swelled rather than occuring during drying, which would be the case if the swelled state were disordered. After a 20 min drying step accomplished by gradually removing the lid of the annealing chamber, the film deswelled to near its as-cast thickness, trapping the swollen morphology.[27] Faster drying by blowing nitrogen to deswell the film produced similar morphologies but with poorer order, described in detail below.

Figure 3.2 shows a series of scanning electron microscopy (SEM) images of the self-assembled structures formed by SD75 films with varying initial thickness under the same solvent annealing conditions, after etching to remove PS and reveal the PDMS morphology, which appears bright. In thicker films, upper and lower layers of PDMS microdomains in a bilayer structure can be distinguished by their different contrast, with the upper layer of PDMS microdomains always appearing brighter. (This contrast difference was also seen previously in bilayer cylindrical structures,[28] in which TEM holography confirmed the presence of a bilayer.) Further examples are given in, section 2(e) and Figures 3.13-14.

With an initial film thickness of 103 or 137 nm, a poorly ordered porous structure was found throughout the film which exhibited interconnected struts reminiscent of the bulk gyroid. Hexagonally-coordinated perforated lamellae (HPL) became the dominant structure as initial film thickness decreased from 85 nm to 63 nm.

Terracing (island and hole formation) can occur during annealing of block copolymer films that form in-plane microdomains due to incommensurability between the polymer film thickness and the out-of-plane period.[5,29] Optical microscopy data (section 2(b) and Figure 3.10) demonstrated that the as-cast film thickness was uniform. The 3-hour solvent annealing used here did not lead to obvious terrace formation in the thicker films (137 nm, Figure 3.2a and 103 nm, Figure 3.2b) where gyroid-like structures existed. However, thinner films, where HPL occurred, form terraces if the film thickness is incommensurate with the HPL layer thickness.

For a 3 hr anneal, films with thickness around 80 nm formed a structure resembling a double layer of HPL (Figure 3.2c) with connections between the upper and lower lamellae in some regions whereas in other regions of the sample there was just a monolayer of HPL. The portion of the sample exhibiting a monolayer HPL increased as the films became thinner. The thickness varied gradually between these types of regions, without terracing. In contrast, further annealing, 6 – 15 hrs, enabled 60-90 nm thick films to exhibit terraces (section 2(b) and Figure 3.10). When the film thickness was 45 nm and swelling ratio around 2.2, no terraces were found except in some regions close to the edge of the substrate, and a highly ordered HPL was formed after the 3-hour toluene: heptane 3:1 vapor annealing. This appears to represent a commensurate thickness, since terraces did not form even on further annealing except in some non-uniform parts of the film. The quality of the structure formed from an initial film thickness of 45 nm was remarkably good, with ‘grain sizes’ or correlation lengths of several μm diameter containing a few point defects, shown in SI section 2(a) and Figure 3.8b.

These results therefore show a transition in morphology from HPL to double layer HPL then to a poorly ordered porous network with increasing thickness for 3:1 toluene:heptane vapor, with particularly well-ordered HPL occuring at 45 nm initial thickness. Experimentally the transition from single to double layer HPL occurred between 45 nm and 79 nm film thickness, while at 85 nm the morphology consisted of an upper and a lower perforated layer with interconnections between them. We therefore estimate the single-layer to double-layer transition thickness at ~65 ± 10 nm.

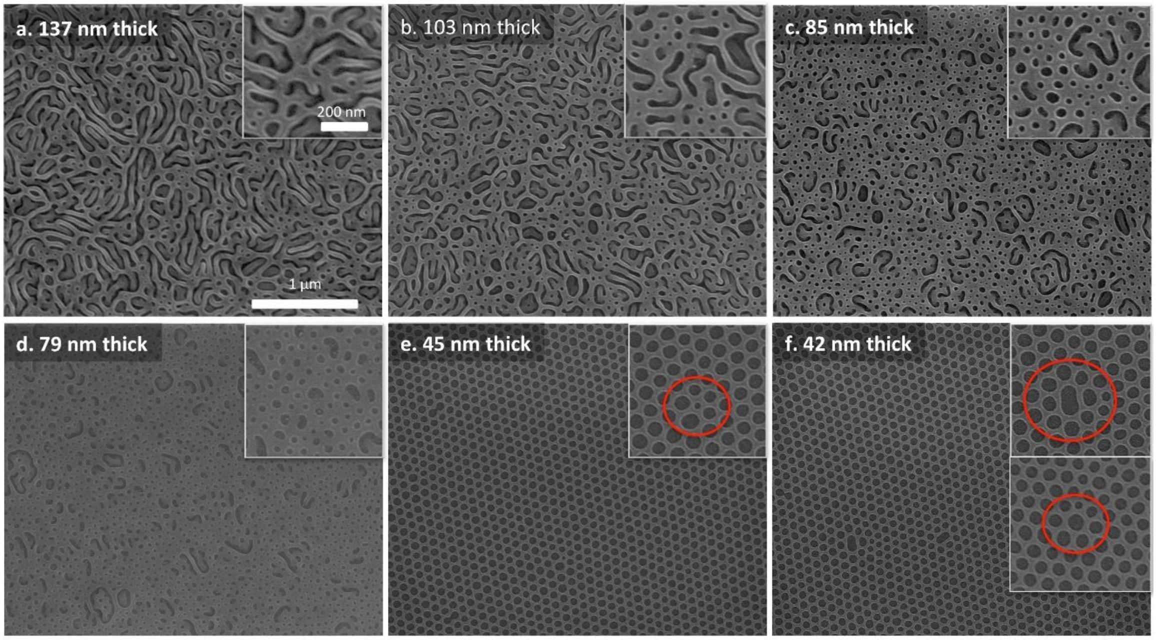

Figure 3.2. Representative SEM images of PDMS microdomains formed in thin films with differing initial thickness at the same solvent vapor annealing condition, from a 3:1 toluene:heptane volumetric mixture (all films swelled to 2.1 - 2.2 times the initial film thickness). The as-cast initial film thickness is indicated at the upper-left corner of each image. a,b: Poorly ordered porous network. c,d: Perforated lamellae (HPL) appeared and dominated as the film became thinner. At ~80 nm thickness two layers of interconnected HPL are visible. e-f: Highly ordered perforated lamellae. e, inset, red circle highlights 5-fold coordinated pores. f, upper inset, red circle highlights 8-fold coordinated pores; lower inset, red circle highlights 7-fold coordinated pores. The images all have the same magnification, shown in a.

3.6 SCFT Modeling of film thickness effects on morphology

Self-consistent field theory (SCFT) simulations were performed to examine the morphology transition as the film thickness changed. These simulations used similar methods to those previously reported by Mickiewicz et al.[30] Further details of the modeling are described in the SI. The interaction and structural parameters used in the SCFT simulation were chosen to represent a bulk-double-gyroid diblock copolymer whose bulk structure is shown in Figure 3.3 inset. The model is described in terms of a characteristic lengthscale, L_0, which was chosen to be the microdomain period when the modeled block copolymer forms a bulk cylindrical morphology. L_0 corresponds to 5.27 R_g with R_g the radius of gyration.

In the experiment the air interface was minority-attractive (evidence for this will be given in the next section), and the oxidized silica substrate was also minority-attractive due to the PDMS brush layer. Films with minority-attractive top and bottom surfaces were modeled, and as expected the model produced a PDMS wetting layer at each surface with thickness $L_0/2$ surrounding a thickness-dependent internal morphology such as spheres, cylinders, etc. Majority-preferential surfaces were also modeled, and we found that the internal morphology was identical to that seen in a simulation of a thicker film with minority-preferential surfaces. In other words, a majority-attractive simulation of thickness t was equivalent to a minority-attractive simulation of thickness $t+L_0$ without its surface layers. This is shown schematically in Fig. 3.3(a). In order to reduce computation time, we therefore modeled majority-preferential top and bottom surfaces for convenience. The model structures in Fig. 3.3(b) are therefore shown without the top and bottom surface layers, even though these layers exist in the experiment.

The model calculates the morphology of the swelled film. Therefore when comparing model and experimental results, a model of thickness t corresponds to an experimental swelled film thickness of $t+L_0$, and to an as-cast film of thickness $(t+L_0)$/SR where SR is the swelling ratio.

In Figure 3.3(b), results for a simulation with $(\chi N)_{\text{eff}} = 18.0$ and $f = 0.411$ are shown. $(\chi N)_{\text{eff}}$ is smaller than the χN of the neat block copolymer because of both the coarse-graining of the model which reduces the number of units in the chain by a factor of 0.15 (125 repeat units were used in the simulation instead of N = 847), and the effect of swelling which lowers χ by approximately a factor of 2.[31] The volume fraction was chosen to match the bulk volume fraction, but preferential uptake of the toluene and heptane by the blocks will vary the effective volume fraction. Simulations describing the effects of vapor composition on morphology will be presented elsewhere,[32] but the simulations presented here correspond most closely to a 3:1 toluene:heptane ratio in the vapor.

The free energy of the microphase-separated film decreased with increasing film thickness until the transition between one and two layers of microdomains was reached. Around this transition region ($0.8 < t/L_0 < 1.2$) there was a local free energy minimum representing perforated lamellae. As thickness increased from the minimum energy thickness the morphology transitioned from perforated lamellae to cylinders, bicontinuous cylinders and double-layer perforated lamellae (as shown in SCFT simulation results, figure 3.3b). Variations in the effective volume fraction lead to dominance of different morphologies, e.g. HPL was present over a wider thickness range as effective volume fraction increases, but all the models showed a transition from one to two layers of microdomains at a thickness $\sim L_0$.

In the model, the single-to-double layer transition at a thickness ~L_0 corresponded to an actual film thickness of $2L_0$ when the wetting layers are included. The spacing of in-plane cylinders measured experimentally (see next section) yields L_0 = 63 nm, from which the transition thickness should be $2L_0$ = 126 nm. This is in reasonable agreement with the transition thickness of the swelled film (~65 ± 10 nm multiplied by the swelling ratio of 2.1, which is ~136 ± 20 nm). This supports the use of the swelled film thickness when comparing the model to the experiment.

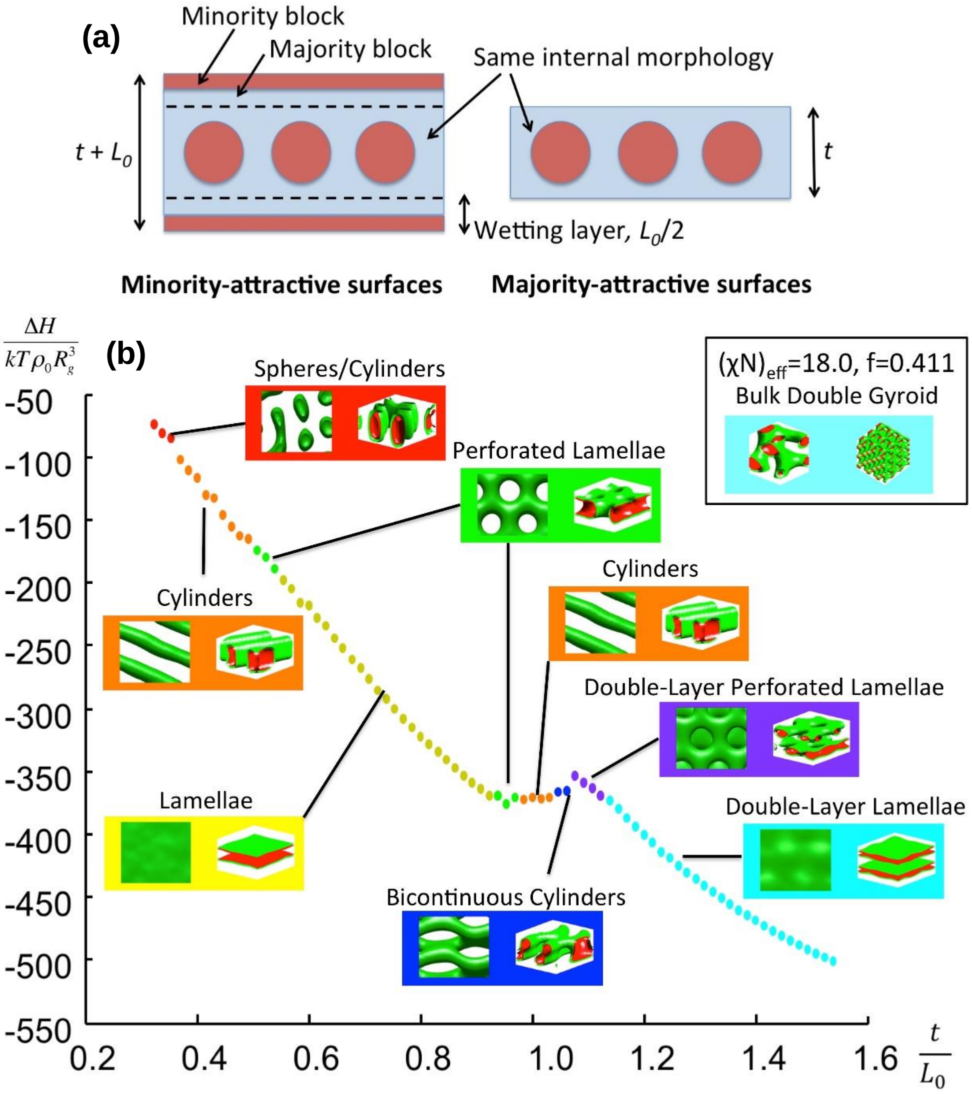

Figure 3.3. (a) A schematic showing the equivalence of the internal structure in a simulation of thickness t+L_0 with minority-attractive surfaces vs. a simulation of

thickness t with majority-attractive surfaces. The latter were simulated in order to reduce computation time. (b) Normalized free energy difference ΔH of the simulated thin film structures compared to a disordered state for a bulk-gyroid BCP system ($\chi N_{eff} = 18.0$, f = 0.411) versus film thickness. k is the Boltzmann constant, T the temperature, $\boldsymbol{\rho_0}$ is the monomer density, R_g the radius of gyration, and L_0 is 5.27 R_g. The inset shows the bulk gyroid structure at different magnifications. Fig. 3.3b data was provided by Dr. Adam Hannon.

3.7 Film morphology as a function of solvent vapor composition and swelling ratio

In PS-*b*-PDMS, heptane selectively swells PDMS while toluene is slightly selective for polystyrene but swells both blocks,[4] so changes in morphology with solvent vapor composition are expected. The solvent vapor composition can also affect the surface-wetting layer, so we first verified that PDMS was present at the air interface, as seen in several prior studies,[4] due to its lower surface energy. To establish whether PDMS was present at the top surface of solvent-annealed films, samples were compared after two processes: a one-step etch in O_2 which removes PS, and a two-step process consisting of a short CF_4 etch which removes any PDMS surface layer then an O_2 etch. The two-step process produced clear images of the internal PDMS microdomains whereas the one-step process showed evidence of the remnants of the unetched PDMS surface layer on top of the internal microdomains (Figure 3.4). This shows that a PDMS surface layer was present in samples annealed in the full range of toluene:heptane vapors studied here, including pure toluene.

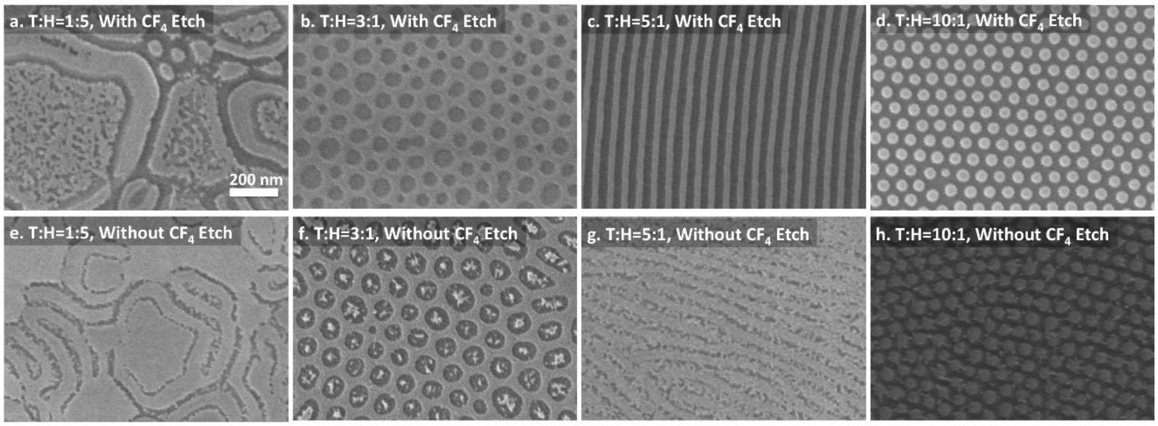

Figure 3.4. Representative SEM images of oxidized PDMS nanostructures with differing toluene:heptane (T:H) volumetric ratio in solvent annealing. a. T:H = 1:5, b. 3:1, c. 5:1, d. 10:1 imaged after 5s CF_4 etch and then 22s O_2 etch; e. T:H = 1:5, f. 3:1, g. 5:1, h. 10:1 imaged after 22s O_2 etch.

Figure 3.5 shows the morphology of films of SD75 with as-cast thickness 45 nm as a function of volumetric ratio of the liquid solvents added to the chamber as well as the swelling ratio, which was adjusted by changing the solvent vapor pressure. At a solvent ratio of toluene: heptane = 3:1 the swelling ratio was 2.1 (i.e. swelled thickness 95 nm), and the film formed HPL (Figure 3.5e) with center-to-center spacing 96 nm and hole size around 75 nm. The row spacing of the pores was $\sqrt{3}/2$ x 95 nm = 79 nm. In contrast, at a solvent ratio of toluene: heptane = 5:1 the swelling ratio was 1.4 (swelled thickness 63 nm), and the film formed a monolayer of in-plane cylinders (Figure 3.5c) with period 63 nm and line width around 35 nm. Figure 3.6a,b show additional images of cylindrical microdomains containing spiral and fingerprint defects. At a solvent ratio of toluene: heptane = 10:1 the swelling ratio was 2.5, and the film formed spheres with a period 66 nm (Figure 3.5b, Figure 3.13). Figure 3.9 shows the distribution of microdomain sizes for samples consisting of spheres and for HPL.

At other solvent ratios of 4:1 (swelling ratio 1.9), 2.5:1 (swelling ratio 1.4), 1.5:1 (swelling ratio 1.2), and pure toluene (swelling ratio 2.4), coexistence of HPL and cylinders (C), C and lamellae (L), HPL and L, and spheres (S) and a wetting layer were found respectively. The HPL/L interface (Figure 3.5g) was a curved line that outlined the hexagonal hole close-packed arrays; the HPL/C interface (Figure 3.5d) had a serrated border; the C/L interface (Figure 3.5f) was a straight line; and the S/wetting layer interface had a size-gradient of spheres (Figure 3.5a). Figure 5h indicates that the mixed morphologies corresponded to terrace formation and the morphological interface is the boundary of the terrace. Additional examples are shown in section 2(d) and Figures 3.11 and 3.12.

The data of Figure 3.5 indicate that at these modest solvent vapor pressures of a few Torr, the structure that forms is influenced by both the solvent ratio, which governs swelling, effective χ, and the effective volume fraction of the blocks,[33] and the swelled film thickness, which determines commensurability with the microdomain spacing. We expect that when the swelled film thickness is commensurate with the block copolymer period a uniform, single morphology would form over the film, as in the HPL formed under the 3:1 toluene:heptane (Figure 3.5e), the cylinders in the 5:1 toluene:heptane mixture (Figure 3.5c) and the spheres in the 10:1 mixture (Figure 3.5b). However when the swelled thickness is incommensurate, a mixed morphology is more likely and terracing is promoted, as in the samples which exhibited mixed HPL+C, C+L or HPL+L morphologies.

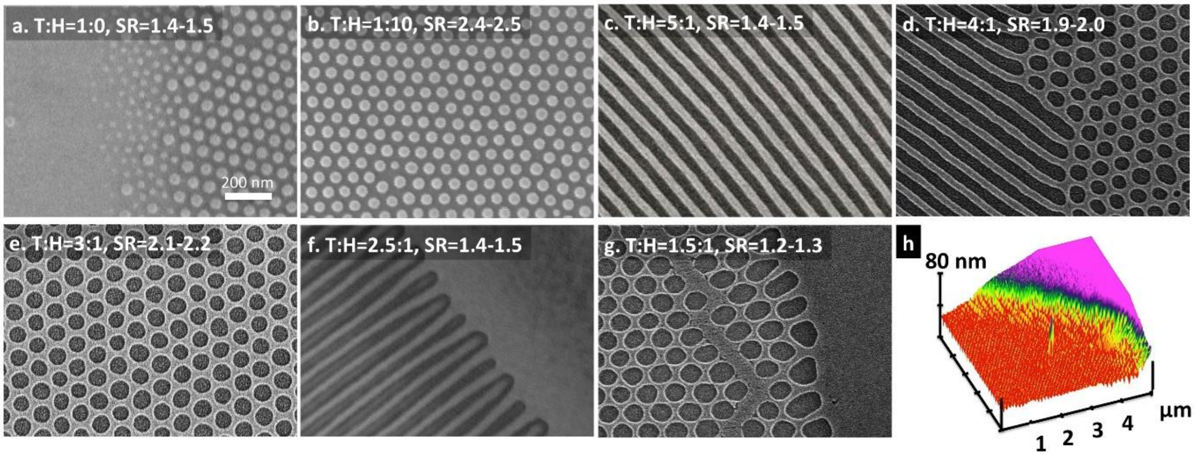

Figure 3.5. Morphologies observed for as-spun film thickness = 45 nm under different solvent vapor annealing conditions (the ratio of toluene: heptane in the solvent reservoir and the swelling ratio are labeled on each image). a. coexistence of spheres and lamellae or wetting layer in pure toluene. b. Spheres from 10:1 toluene: heptane forming patterns with period 66 nm. c. Cylinders formed in 5:1 toluene: heptane with period 63 nm and PDMS linewidth 35 nm; d. coexistence of cylinders and perforated lamellae; e. perforated lamellae, 3:1 toluene: heptane mixture vapor forming perforated lamellar patterns with period 92 nm, hole size 75 nm; f. coexistence of cylinders and lamellae; g. coexistence of perforated lamellae and lamellae; h. 3D AFM image of coexistence of perforated lamellae and lamellae showing a height change.

3.8 The effect of drying rate

The annealing process consists of three successive regimes: solvent incorporation, annealing at a constant swelling ratio, and drying or deswelling. In the SD75 we expect microphase separation to occur in the swelled film. Drying then causes the swollen film to collapse in the out-of-plane direction and trap the morphology since the PS goes below the glass transition temperature. In general, the solvent-annealed microdomain morphology will depend on all three regimes, and the contribution of the drying process has been examined, for example in thick films.[8, 44]

Figure 3.6 shows the effect of a higher drying speed using a blast of nitrogen, after annealing under the conditions that produced well-ordered HPL (45 nm film, 3:1 toluene:heptane, swelling ratio = 2.2) and C (45 nm film, 5:1 toluene:heptane, swelling ratio = 1.5) as used in Fig 3.5g and 5c respectively. The films deswelled within 1 second. In Figure 3.6c the pore size in the HPL had a greater variability (though the average center-to-center spacing was 90 nm, which is similar to Figure 3.5e), while in Figure 3.6d the cylinders had more discontinuities and a more irregular edge roughness (though the average period is ~60 nm similar to Figure 3.5c). In comparison the samples shown in Figure 3.5 were quenched by gradually opening the chamber lid in 20 min, and the deswelling was observed to follow an exponential decay with time. Most of the solvent was removed from the film in the first 50s of the 20 min drying. Hence the dried morphology is affected by both the steady state solvent atmosphere and the drying process.[21]

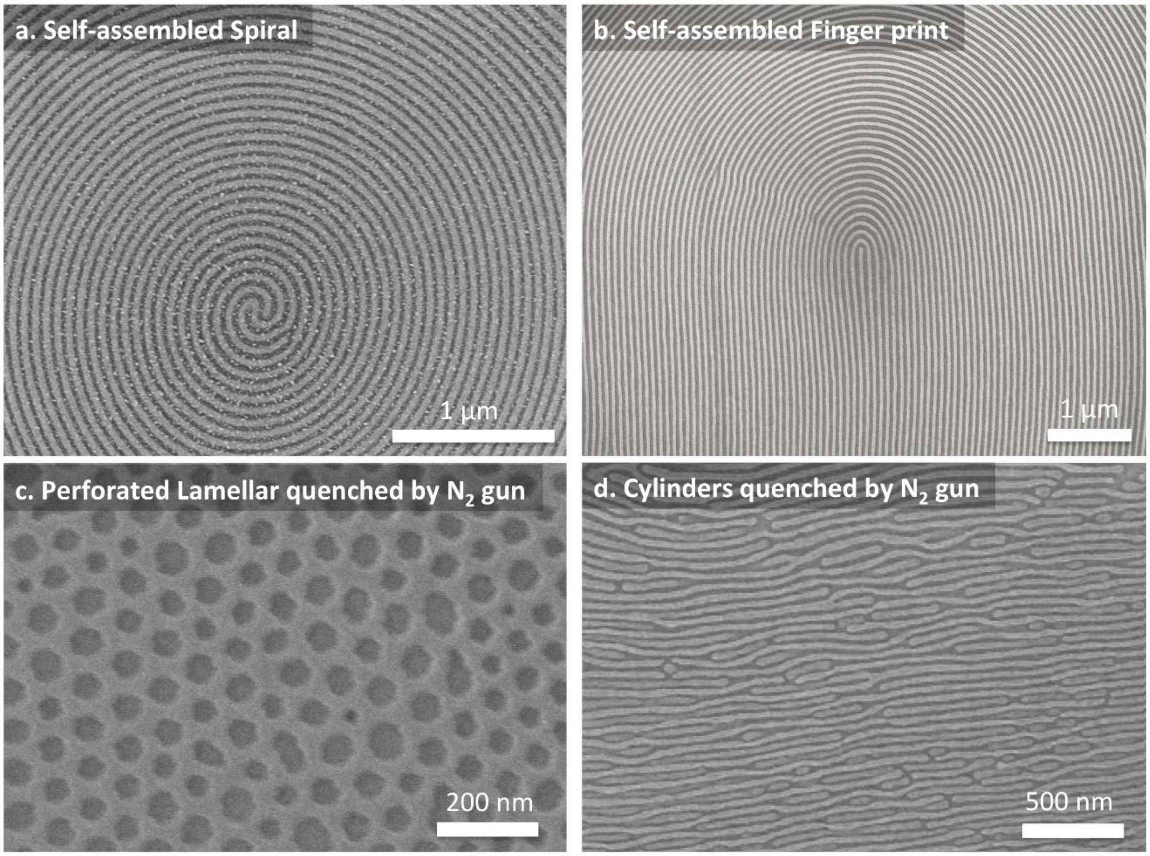

Figure 3.6. a. Fingerprint pattern around a defect in the cylinder array; b. spiral pattern, a defect in the cylinders, both annealed under the same conditions as Figure 3.5c. c, d. Morphologies observed for fast drying by using a blast of nitrogen. c. Perforated lamellae; d. cylinders.

3.9 Defect analysis

The best ordered structures achieved in the present work were cylinders with defect density ~0.01 defects/ μm^2 over an area of about 10 × 10 μm^2 (Figure 3.8a), or perforated lamellae with defect density ~0.2 defect/ μm^2 within 'grains' of areas about 4 × 4 μm^2

(Figure 3.8b). Nearest neighbor distances and pair correlations for HPL and spheres are given in Figure 3.9. The defects in the cylinder arrays mainly consisted of a single disclination (cylinder termination) surrounded by a large area of cylinders bent by 180˚ (Figure 3.6b) or forming a spiral (Figure 3.6a), unlike the defectivity in lamella-forming diblock copolymers.[34] Other defects included Y-junctions between two or more cylinders, and a Y junction associated with a termination.

For the HPL, there were two dominant defect types. Some of these defects were 8-fold coordinated pores that adopted an elliptical shape, and can be described as the result of a missing bridge between two pores. Similarly coordinated defects have been observed in other HPL films produced from a bulk cylindrical block copolymer.[3,27] Defects consisting of adjacent 5-, 7- and 8-coordinated pores (figure 3.2e,f insets) were also seen representing a dislocation in the 2D array. Separated 5- or 7-fold coordinated pores occurred at grain boundaries. For the monolayer of spheres, the defects within a grain consisted of missing spheres or sphere-size variations. Multiple annealing further reduced defects, i.e. for the same swelling ratio, deswelling and swelling the film several times increased the ordered area.

3.10 Self-consistent field theory simulations

In the simulations performed, the system was modeled using real space unit cells of N_x by N_y by N_z grid points. The system is modeled using a standard block copolymer partition function $Z = \int e^{-H[\Omega(\vec{r})]} d\Omega$ where $H[\Omega(\vec{r})]$ is the free energy Hamiltonian of the system as a functional of the chemical potential fields Ω which are a function of the real space position $\vec{r}$. Using a mean field approximation, the assumption is made that there exists a dominant chemical potential field configuration Ω^* that makes $Z \cong e^{-H[\Omega^*(\vec{r})]}$ such that $\frac{\delta H}{\delta \Omega^*} = 0$ is satisfied. This means that if Ω^* is found, it is a saddle point solution that represents either a minimum or metastable equilibrium structure for simulation conditions considered. These equations are solved by initiating the system with a random density field configuration, using a complex Langevin relaxation scheme to find Ω^* that satisfies the saddle point condition, and updates the conjugate density fields and propagator functions related to the Ω^* field. More information on the numerical implementation of SCFT in block copolymer systems is presented by Fredrickson et al.[30,35,36]

For bulk simulations, periodic boundary conditions are considered in all 3 directions with $N_x = N_y = N_z = 16$. To gauge the natural periodicities of the morphologies in the bulk, a length L in units of R_g was assigned to the to the x, y, and z sides of the unit cell and varied from $2.43R_g$ to $7.30R_g$. The simulations were then performed over this range of assigned box lengths and the resulting morphologies were categorized. The dominant morphologies found then had free energy curves computed by taking the density field solutions from the side length simulations, calculating equilibrated energies by holding those density fields constant, and finding the corresponding chemical potentials under the different conditions. These calculations were done for 4 proposed structures: square packed cylinders, hexagonally packed cylinders, cubic gyroid, and double gyroid, for three different values of χN. The 3D morphology density fields are shown in Figure 3.7. From this analysis, the natural period of the hexagonal cylinder phase was found to be $5.27R_g$ and this was used as L_0 in order to provide a length scale for the thin film simulations.

More details on using SCFT simulation to understand solvent vapor annealing can be found in Ref. [37]

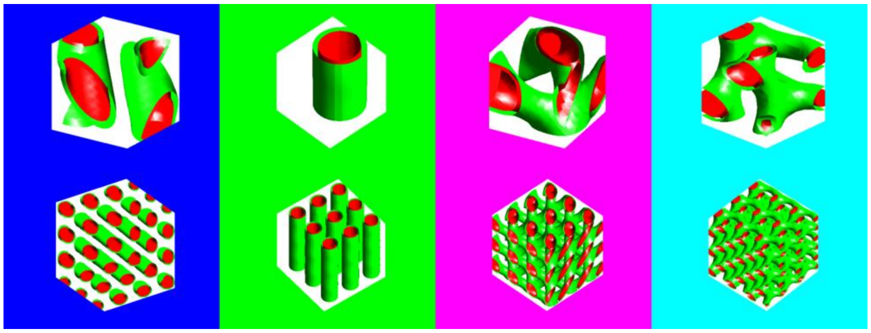

Figure 3.7. Simulated SCFT equilibrium structures of the nanostructures formed in the bulk state. Green surfaces are where the polymer density $\phi = 0.5$ and red areas are where the density is minority rich ($\phi > 0.5$). Top row shows a single unit cell from the SCFT calculations and bottom row shows 3 units cells by 3 unit cells of the structure. From left to right the structures are hexagonally packed cylinders (blue), square packed cylinders (green), cubic gyroid (magenta), and double gyroid (cyan). Figure 3.7 data was provided by Dr. Adam Hannon.

3.11 Experimental Supplementary infomation

(a) A large area of Perforated Lamellae and Cylinders

Figure 3.8 (a) shows a large area of cylinders with few defects (0.2 / μm^2) and (b) shows a large area of perforated lamellae with few defects (0.4/ μm^2).

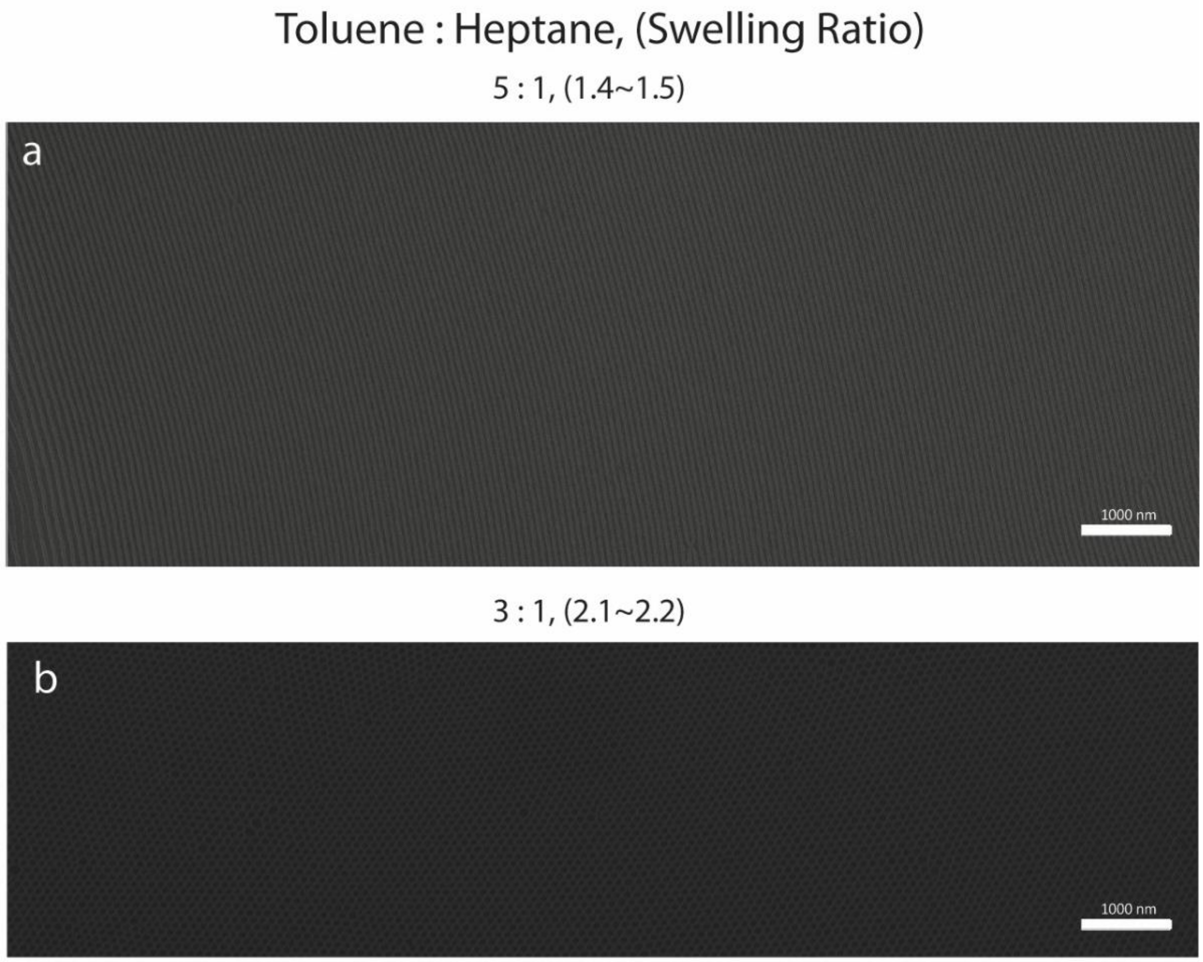

Figure 3.8. (a) A large area of cylinders**.** (b) A large area of Perforated Lamellae with initial as-cast film thickness 45 nm.

The pair correlation functions and nearest neighbor distance distributions of the hexagonal perforated lamellae and spheres are plotted in Figure 3.7 in order to learn the respective correlation lengths. Spheres have an inter-domain spacing of 67.4±7.8 nm and their correlation length is about 800 nm, whereas the hexagonal perforated lamellae have an inter-domain spacing of 96.4±7.8 nm and their correlation length is over 5 µm.

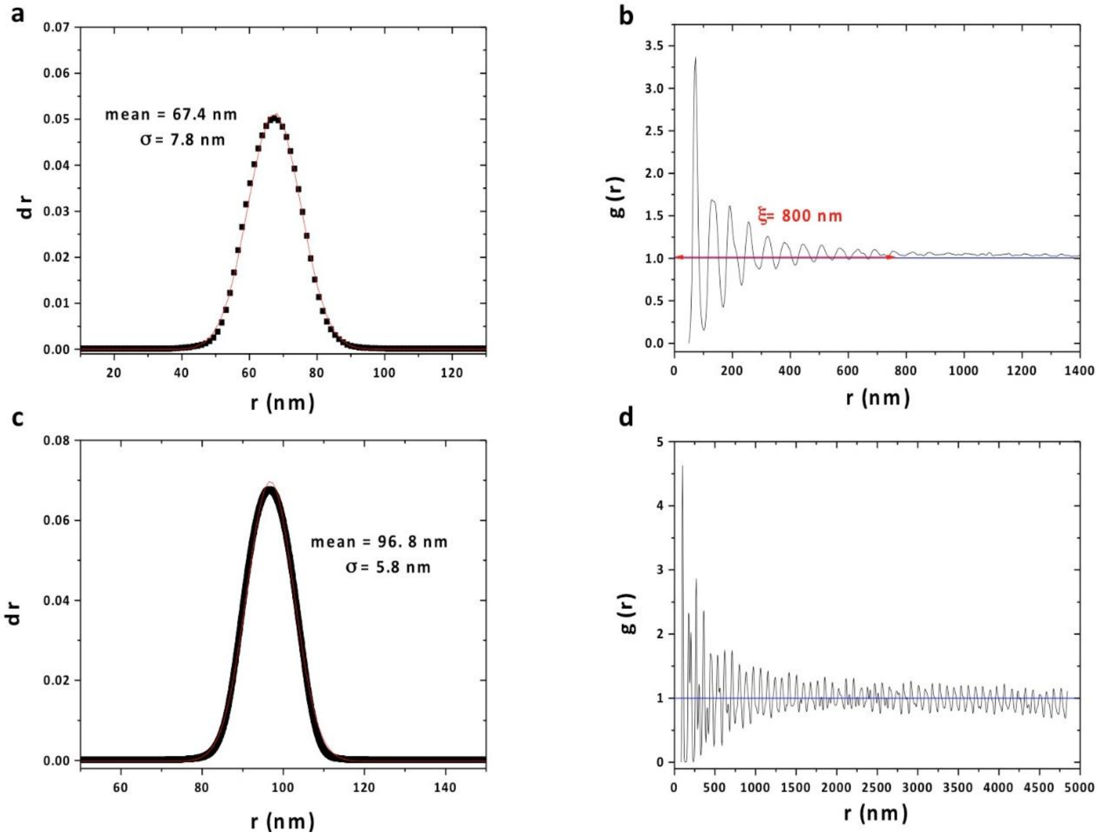

Figure 3.9. (a), (c), Nearest Neighbor distance distribution; (b), (d), Pair-correlation function; (a), (b), Sphere phase; (c), (d), Hexagonal Perforated Lamellae phase. Fig. 3.9 data was provided by Dr. Karim Aissou.

(b) Terrace formation as annealing time increased

For SD75 PS-PDMS films with thickness 90 nm, vapor from a toluene: heptane 3:1, volumetric mixture (P_{tol} = 2.055 kPa, P_{hep} =0.673 kPa) did not lead to dewetting for 3-hour annealing as shown in Figure 3.18.a. Terraces were observed after 6-hour annealing as shown in Figure 3.10.b. During annealing, the shape and thickness of terraces were found to change and stabilized after ~15 hour for the 90 nm SD75 film.

A film with thickness 90 nm annealed in a vapor from a toluene:heptane 3:1 volumetric mixture is incommensurate with the optimum thickness of any of the possible morphologies calculated by SCFT. Therefore the films start to form terraces in which each terrace has an optimum thickness for a particular morphology. The in situ optical microscopy records this terrace forming process. Quenching the films when the film just started to form terraces then etching showed that the terraces corresponded to different morphologies (see Figs. 3.11).

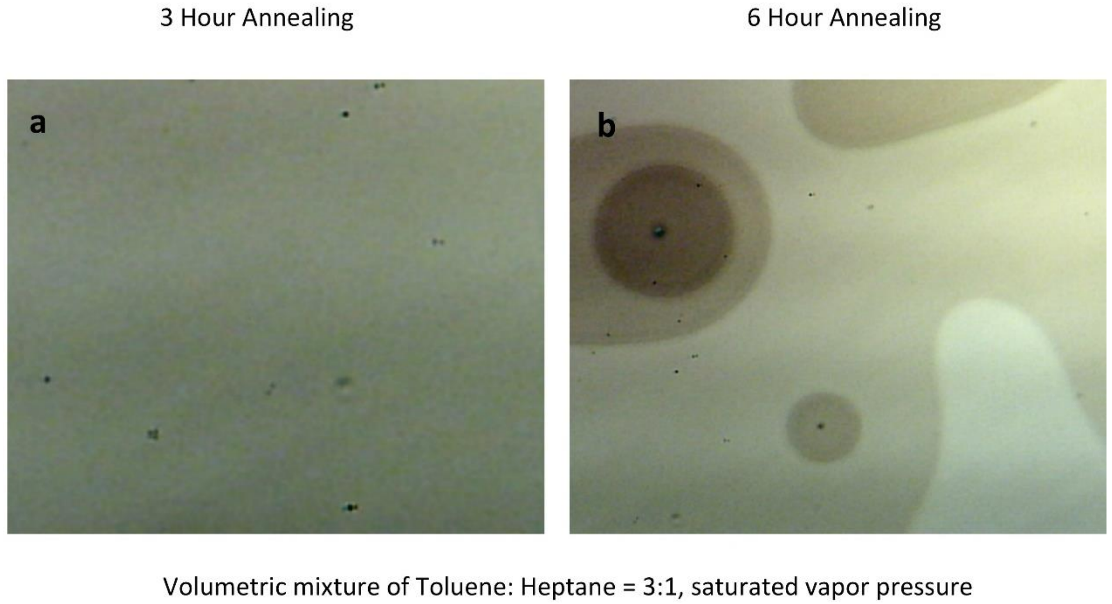

Figure 3.10. BCP films with films of thickness of ~90 nm annealed under vapor pressure (P_{tol} = 2.055 kPa, P_{hep} =0.673 kPa) from a toluene: heptane 3:1 volumetric mixture at room temperature. Terraces form when annealing time is around 6 hours or longer. (a) 3-hour annealing (b) 6-hour annealing.

(c) Expected Vapor pressures for various solvent mixtures (toluene:heptane) at room temperature (23 ˚C ± 2˚C) with controlled leakage

The non-random two liquid model (NRTL) model[38] can be used to calculate activity coefficients (γ_1, γ_2) for liquid mixtures of binary solvents. The calculated partial pressure is given by:

$$p_1 = \gamma_1 x_1 \, p_1^*$$
$$p_2 = \gamma_2 x_2 \, p_2^*$$

where p_1, p_2 are the partial pressures of components 1, 2. p_1^*, p_2^* are saturated vapor pressures in the pure states. x_1, x_2 are the mole fractions of components 1, 2 in liquid mixtures.

Therefore the expected vapor pressures for various solvents mixtures (toluene: heptane) at room temperature (23 ˚C ± 2˚C) are:

Toluene: Heptane (Swelling Ratio)	1.5:1 (1.3)	2.5:1 (1.5)	3:1 (2.2)	4:1 (2.0)	5:1 (1.5)	10:1 (2.5)	1:0 (2.5)
$p_{toluene}$(Torr)	4.90	6.73	10.37	10.06	7.86	14.29	16.34
$p_{heptane}$(Torr)	5.94	4.90	6.29	4.57	2.86	2.60	0

Table 1. Expected vapor pressures for various solvent mixtures (toluene:heptane) at room temperature with controlled leakage.

(d) The height difference between two morphologies in one film

With other conditions in solvent annealing the same, slightly changing the ratio of solvents can leading to a different area ratio of lamellae and cylinders. The shape of the region containing cylinders (lighter region in Figure 3.12, 13) also changed from equiaxed to stripe-like as the fraction of toluene increased. The AFM images of the etched film (Figure 3.11) show that the two regions of different morphology have a height difference at their boundary. The L phase is higher than HPL phase therefore we concluded that that the L region is lamellar and does not indicate dewetting. The step height is half of the film thickness. The optical microscopy images (Figure 3.12) of the unetched film during annealing and the SEM images of the etched film indicate that the two-phase boundary corresponds to the terrace boundary.

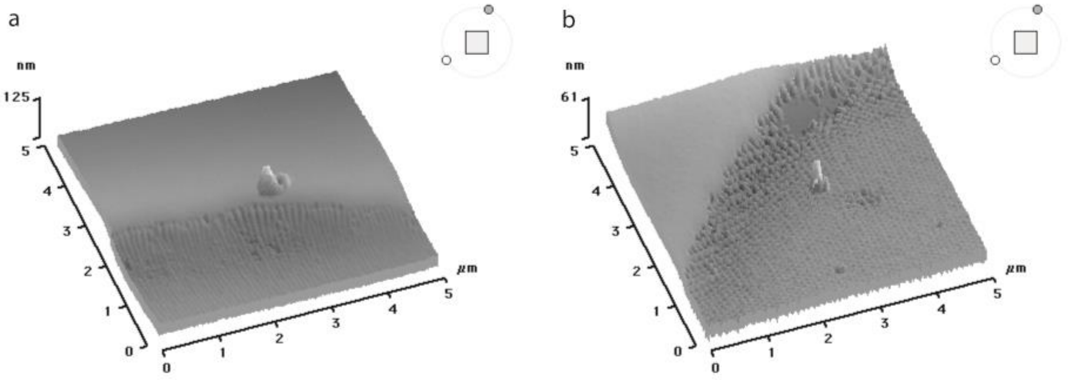

Figure 3.11. AFM image of mixed morphologies (a, L and C, b, HPL and L). The interface between two phases (left: C+L, right HPL+L) corresponds to a terrace edge.

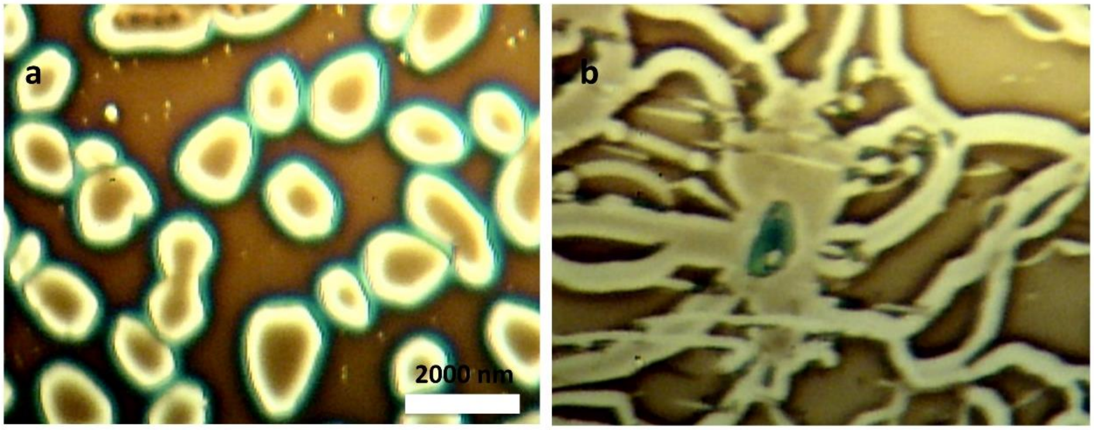

Figure 3.12. Optical microscopy images of the unetched films with cylinder-lamella coexistence. After SEM, the lighter region was found to be cylinders, and the darker region is lamella. (a) Volumetric ratio of Toluene and Heptane 1.3:1 (b) Volumetric ratio of Toluene and Heptane 1.5:1.

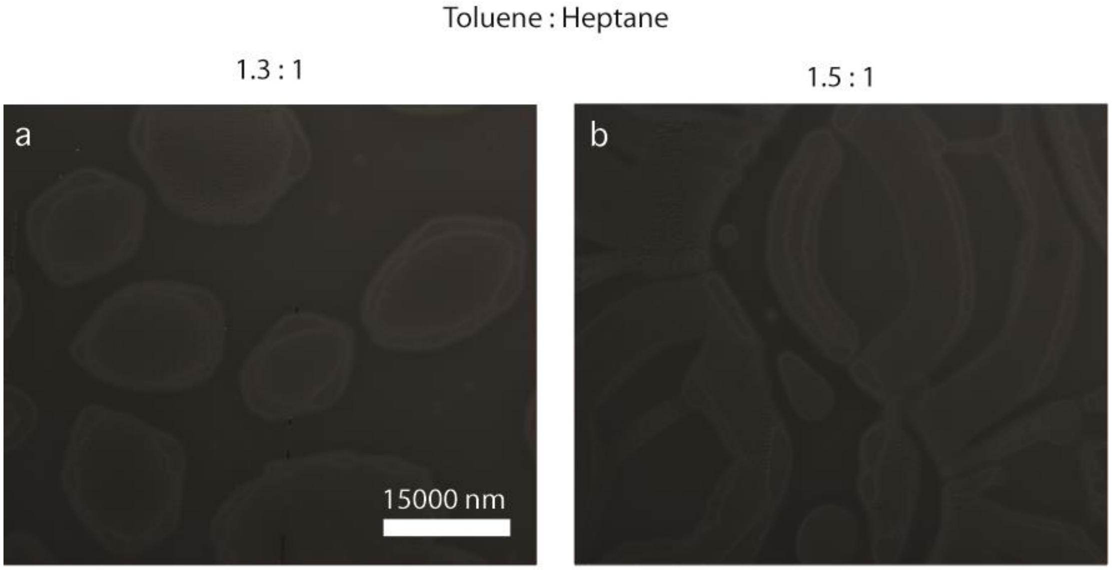

Figure 3.13. Cylinder-Lamella coexistence observed at different solvent annealing conditions with swelling ratio around 1.5, as-cast film thickness 45 nm, 3-hour annealing. The lighter region is cylinders, the darker region is lamellae. (a) Volumetric ratio of toluene and heptane 1.3:1, area ratio of cylinders is ~0.4 (b) Volumetric ratio 1.5:1, Area ratio of cylinders is ~0.7.

(e) Formation of a layer of PDMS at the air/BCP film interface

SD75 films with initial film thickness 45 were annealed in various solvent mixtures. The CF_4/O_2 etch (upper images, Figure 3.14) removes any PDMS surface layer, whereas using just O_2 (lower images) leaves a residue of the PDMS surface layer seen as bright particles, and the internal PDMS microdomains are not as clear. The SEM images show the PDMS layer is present on the top surface for all the solvent vapor conditions, though this layer appears thinner as the toluene fraction increased.

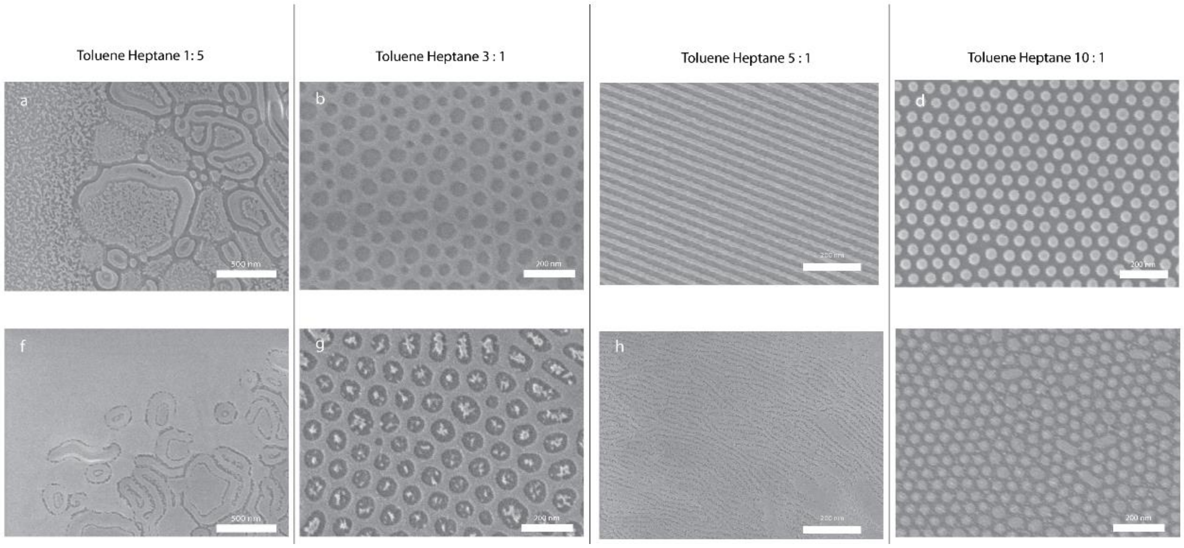

Figure 3.14. SD75 BCP films with initial film thickness 45 nm were annealed in various solvent mixtures. (a-d) Reactive Ion Etching in CF_4 then in O_2. (f-i) Reactive Ion Etching directly in O_2.

(f) Identifying bilayer self-assembled structures:

To distinguish between spheres and perpendicular cylinders, a thicker film was annealed under the same annealing condition for producing spheres (figure 3.5b). In the highlighted region of figure 3.15a, the contrast and the center-to-center distance indicate that a bilayers of spheres formed, rather than perpendicular cylinders. The upper layer of spheres is brighter, as seen for bilayer cylinders in which the bilayer was verified both by tilted view SEM[6]. Fig. 3.16 shows another example of a bilayer structure with a region of cylindrical morphology and a region of interconnected microdomains.

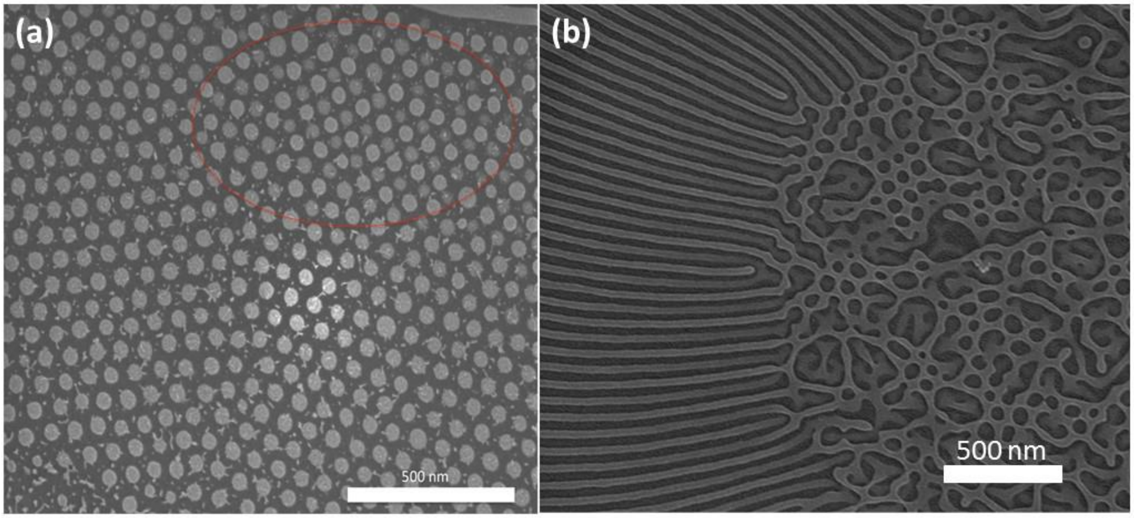

Figure 3.15. (a) Spheres observed for film thickness = 65 nm under 10:1 toluene: heptane volumetric ratio. The circled region shows a bilayer of spheres with one layer darker contrast (lower height) than the other. (b) Top view SEM image of SD75 BCP with a region of cylinders at the left and interconnected structures at the right.

3.12 Pattern transfer using self-assembled nanostructure as a mask

The etched BCP film can be used as a sacrificial mask for patterning another material.[39,40] Monolayers of in-plane cylinders or spheres, perpendicular cylinders and lamellae, and perforated lamellae are particularly suitable for pattern transfer. Pattern transfer takes advantages of the methods developed for planar processing, including additive (e.g. liftoff) and subtractive (etching) methods. More details on BCP pattern transfer can be found in Ref. [41].

Etching an underlying material through a BCP mask allows pattern transfer into many materials including multilayers or epitaxial structures that cannot be grown on top of the BCP mask.[40,42,43] Reactive ion etching or ion-beam etching are typically used, and the BCP pattern may first be transferred into a hard mask such as a heavy metal (Ta, W, etc.) or hard carbon which has greater durability than the BCP film during the etch of the functional material. Many transition metals cannot be easily etched by reactive ion etching. Ion beam etching may be used but this process typically exhibits redeposition and poor etch selectivity, often requiring a hard mask.

Additive patterning has also been widely applied including electrodeposition, lift-off and damascene processes.[44,45] Lift-off involves depositing the functional material onto a soluble BCP pattern with vertical or undercut pores using a collimated vapor deposition process such as evaporation to produce well-defined edge morphologies of the deposited material. Dissolving the BCP pattern removes the material on top of it, leaving only the material that was deposited on the substrate at the bottom of the pores. In a damascene process, the functional material is deposited over BCP topographical features then etched back and planarized by, for example, reactive ion etching. Etching is stopped once it has reached the BCP features, leaving the functional material within the pores of the BCP film.[46]

Using the damascene pattern transfer process, Cobalt nanodots and nanowires are fabricated using a gyroid-forming PS-PDMS (M_w=75.5 kg/mol) BCP. Localized topography and magnetic structures were probed by MFM after dc demagnetization, as shown in Figure 3.16. The MFM image of the etched cobalt dots (Figure. 3.16b) shows a dark and bright contrast at each end of a diameter which is indicative of an in-plane dipole. The magnetization directions in most of the dots were parallel with their nearest neighbors, in agreement with the effect of magnetostatic interactions at remanence after in plane saturation. On the other hand, in the MFM image of cobalt wires, bright contrast was found either at the end of wires or at the location of large-angle bends, indicating the existence of magnetic poles and domain walls in the wires.[41]

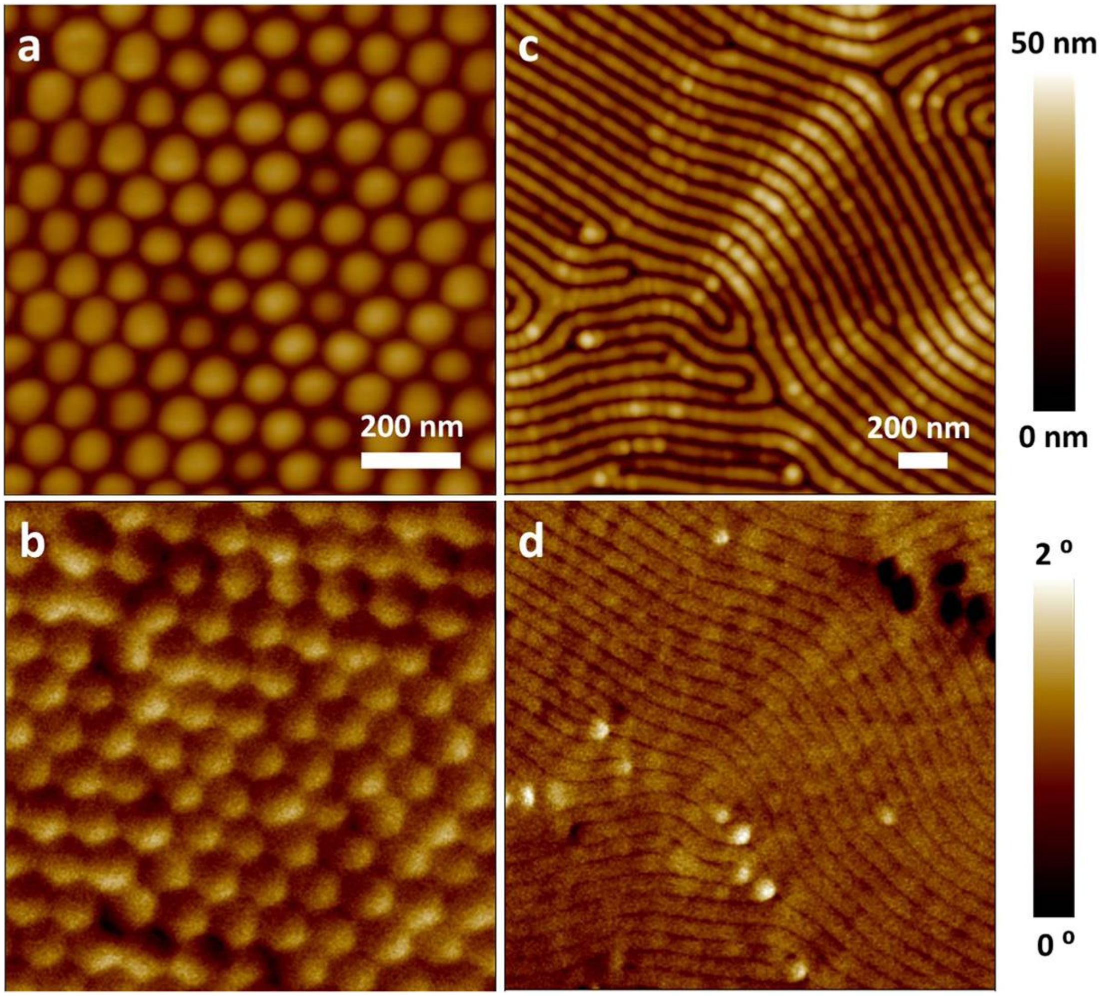

Figure 3.16. The surface topography of ion beam patterned (a) cobalt nanodots and (c) nanowires imaged by scanning probe microscopy. (b), (d) The corresponding magnetic structure of the morphologies in (a) and (c). The figure was reproduced from Ref. [41].

3.13 Conclusions

Thin film morphologies of a bulk gyroid block copolymer showed a rich set of morphologies determined by the film thickness and solvent annealing conditions, including solvent vapor pressure and composition, annealing time and drying process. A feedback mechanism was established by applying a Filmetrics to monitor the swelling ratio in situ and adding a fine leakage valve to control the vapor pressure; therefore the swelling ratio can be tuned at different solvent compositions. The solvent composition and pressure affect the relative swelling of the two blocks and therefore the effective volume fraction, the swelled film thickness, and the effective χ. In plane cylinders (period 63 nm), HPL (center to center spacing 92 nm) and spheres (center to center spacing 66 nm) with excellent long range order and low defect levels were produced from the SD75 at specific film thickness and solvent vapor compositions. Other solvent ratios produced mixed morphology structures such as comb-like patterns from coexisting lamellae and cylinders. The morphologies obtained at different thicknesses matched some of those predicted by SCFT, which included the formation of in-plane lamellae, single or double layer perforated lamellae, or single or double layer cylinders depending on the film thickness and the block volume fraction.

The best ordered nanostructures were achieved by selecting the film thickness, solvent ratio and swelling ratio to obtain a swelled film whose thickness was commensurate with the morphology corresponding to the effective volume fraction and χN in the swelled film, thereby avoiding terracing, and using a slow solvent drying process after solvent vapor annealing. The excellent order and tunability produced from this untemplated block copolymer of relatively large molecular weight is likely to inspire applications in fabricating devices such as heterojunction photovoltaics, fuel cells, desalination or heat transfer membranes where periodicity in the 60 – 100 nm range is required.

References:

(1) Bai, W.; Hannon, A. F.; Gotrik, K. W.; Choi, H. K.; Aissou, K.; Liontos, G.; Ntetsikas, K.; Alexander-Katz, A.; Avgeropoulos, A.; Ross, C. A. Thin Film Morphologies of Bulk-Gyroid Polystyrene- Block -Polydimethylsiloxane under Solvent Vapor Annealing. *Macromolecules* **2014**, *47* (17), 6000–6008.

(2) Gotrik, K. W.; Hannon, A. F.; Son, J. G.; Keller, B.; Alexander-Katz, A.; Ross, C. A. Morphology Control in Block Copolymer Films Using Mixed Solvent Vapors. *ACS Nano* **2012**, *6* (9), 8052–8059.

(3) Jung, Y. S.; Ross, C. A. Solvent-Vapor-Induced Tunability of Self-Assembled Block Copolymer Patterns. *Adv. Mater.* **2009**, *21* (24), 2540–2545.

(4) Jung, Y. S.; Ross, C. A. Orientation-Controlled Self-Assembled Nanolithography Using a Polystyrene-Polydimethylsiloxane Block Copolymer. *Nano Lett.* **2007**, *7* (7), 2046–2050.

(5) Knoll, A.; Horvat, A.; Lyakhova, K.; Krausch, G.; Sevink, G.; Zvelindovsky, A.; Magerle, R. Phase Behavior in Thin Films of Cylinder-Forming Block Copolymers. *Phys. Rev. Lett.* **2002**, *89* (3), 035501.

(6) She, M.-S.; Lo, T.-Y.; Ho, R.-M. Controlled Ordering of Block Copolymer Gyroid Thin Films by Solvent Annealing. *Macromolecules* **2014**, *47* (1), 175–182.

(7) Epps, T. H.; DeLongchamp, D. M.; Fasolka, M. J.; Fischer, D. A.; Jablonski, E. L. Substrate Surface Energy Dependent Morphology and Dewetting in an ABC Triblock Copolymer Film. *Langmuir* **2007**, *23* (6), 3355–3362.

(8) Phillip, W. A.; Hillmyer, M. A.; Cussler, E. L. Cylinder Orientation Mechanism in Block Copolymer Thin Films Upon Solvent Evaporation. *Macromolecules* **2010**, *43* (18), 7763–7770.

(9) Paradiso, S. P.; Delaney, K. T.; García-Cervera, C. J.; Ceniceros, H. D.;

Fredrickson, G. H. Block Copolymer Self Assembly during Rapid Solvent Evaporation: Insights into Cylinder Growth and Stability. *ACS Macro Lett.* **2014**, *3* (1), 16–20.

(10) Jin, S.; Yoon, J.; Heo, K.; Park, H.-W.; Kim, J.; Kim, K.-W.; Shin, T. J.; Chang, T.; Ree, M. Detailed Analysis of Gyroid Structures in Diblock Copolymer Thin Films with Synchrotron Grazing-Incidence X-Ray Scattering. *J. Appl. Crystallogr.* **2007**, *40* (5), 950–958.

(11) Politakos, N.; Ntoukas, E.; Avgeropoulos, A.; Krikorian, V.; Pate, B. D.; Thomas, E. L.; Hill, R. M. Strongly Segregated Cubic Microdomain Morphology Consistent with the Double Gyroid Phase in High Molecular Weight Diblock Copolymers of Polystyrene and Poly(dimethylsiloxane). *J. Polym. Sci. Part B Polym. Phys.* **2009**, *47* (23), 2419–2427.

(12) Wang, C.-Y.; Lodge, T. P. Kinetics and Mechanisms for the Cylinder-to-Gyroid Transition in a Block Copolymer Solution. *Macromolecules* **2002**, *35* (18), 6997–7006.

(13) Vigild, M. E.; Almdal, K.; Mortensen, K.; Hamley, I. W.; Fairclough, J. P. A.; Ryan, A. J. Transformations to and from the Gyroid Phase in a Diblock Copolymer. *Macromolecules* **1998**, *31* (17), 5702–5716.

(14) Hajduk, D. A.; Harper, P. E.; Gruner, S. M.; Honeker, C. C.; Kim, G.; Thomas, E. L.; Fetters, L. J. The Gyroid: A New Equilibrium Morphology in Weakly Segregated Diblock Copolymers. *Macromolecules* **1994**, *27* (15), 4063–4075.

(15) Yu, B.; Li, B.; Sun, P.; Chen, T.; Jin, Q.; Ding, D.; Shi, A.-C. Cylinder-Gyroid-Lamella Transitions in Diblock Copolymer Solutions: A Simulated Annealing Study. *J. Chem. Phys.* **2005**, *123* (23), 234902.

(16) Lodge, T. P.; Hanley, K. J.; Pudil, B.; Alahapperuma, V. Phase Behavior of Block Copolymers in a Neutral Solvent. *Macromolecules* **2003**, *36* (3), 816–822.

(17) Lo, T.-Y.; Ho, R.-M.; Georgopanos, P.; Avgeropoulos, A.; Hashimoto, T. Direct Visualization of Order–Order Transitions in Silicon-Containing Block Copolymers by Electron Tomography. *ACS Macro Lett.* **2013**, *2* (3), 190–194.

(18) Ma, M.; Thomas, E. L.; Rutledge, G. C.; Yu, B.; Li, B.; Jin, Q.; Ding, D.; Shi, A.-C. Gyroid-Forming Diblock Copolymers Confined in Cylindrical Geometry: A Case of Extreme Makeover for Domain Morphology. *Macromolecules* **2010**, *43* (6), 3061–3071.

(19) Hajduk, D. A.; Takenouchi, H.; Hillmyer, M. A.; Bates, F. S.; Vigild, M. E.; Almdal, K. Stability of the Perforated Layer (PL) Phase in Diblock Copolymer Melts. *Macromolecules* **1997**, *30* (13), 3788–3795.

(20) Nose, T. Coexistence Curves of Polystyrene/ Poly(dirnethylsiloxane) Blends. *Polymer (Guildf).* **1995**, *36* (11), 2243–2248.

(21) Son, J. G.; Gotrik, K. W.; Ross, C. A. High-Aspect-Ratio Perpendicular Orientation of PS- B -PDMS Thin Films under Solvent Annealing. *ACS Macro Lett.* **2012**, *1* (11), 1279–1284.

(22) Kennemur, J. G.; Yao, L.; Bates, F. S.; Hillmyer, M. A. Sub-5 Nm Domains in

Ordered Poly(cyclohexylethylene)- Block -Poly(methyl Methacrylate) Block Polymers for Lithography. *Macromolecules* **2014**, *47* (4), 1411–1418.

(23) Elbs, H.; Krausch, G. Ellipsometric Determination of Flory-Huggins Interaction Parameters in Solution. *Polymer (Guildf).* **2004**, *45* (23), 7935–7942.

(24) Jung, Y. S.; Jung, W.; Tuller, H. L.; Ross, C. A. Nanowire Conductive Polymer Gas Sensor Patterned Using Self-Assembled Block Copolymer Lithography. *Nano Lett.* **2008**, *8* (11), 3776–3780.

(25) Bellas, V.; Iatrou, H.; Hadjichristidis, N. Controlled Anionic Polymerization of Hexamethylcyclotrisiloxane. Model Linear and Miktoarm Star Co- and Terpolymers of Dimethylsiloxane with Styrene and Isoprene. *Macromolecules* **2000**, *33* (19), 6993–6997.

(26) Gu, X.; Gunkel, I.; Hexemer, A.; Gu, W.; Russell, T. P. An in Situ Grazing Incidence X-Ray Scattering Study of Block Copolymer Thin Films during Solvent Vapor Annealing. *Adv. Mater.* **2014**, *26* (2), 273–281.

(27) Aissou, K.; Shaver, J.; Fleury, G.; Pécastaings, G.; Brochon, C.; Navarro, C.; Grauby, S.; Rampnoux, J.-M.; Dilhaire, S.; Hadziioannou, G. Nanoscale Block Copolymer Ordering Induced by Visible Interferometric Micropatterning: A Route towards Large Scale Block Copolymer 2D Crystals. *Adv. Mater.* **2013**, *25* (2), 213–217.

(28) Tavakkoli K G, A.; Gotrik, K. W.; Hannon, A. F.; Alexander-Katz, A.; Ross, C. A.; Berggren, K. K. Templating Three-Dimensional Self-Assembled Structures in Bilayer Block Copolymer Films. *Science* **2012**, *336* (6086), 1294–1298.

(29) Netz, R.; Andelman, D.; Schick, M. Interfaces of Modulated Phases. *Phys. Rev. Lett.* **1997**, *79* (6), 1058–1061.

(30) Mickiewicz, R. A.; Yang, J. K. W.; Hannon, A. F.; Jung, Y.-S.; Alexander-Katz, A.; Berggren, K. K.; Ross, C. A. Enhancing the Potential of Block Copolymer Lithography with Polymer Self-Consistent Field Theory Simulations. *Macromolecules* **2010**, *43* (19), 8290–8295.

(31) Hashimoto, T.; Shibayama, M.; Kawai, H. Ordered Structure in Block Polymer Solutions. 4. Scaling Rules on Size of Fluctuations with Block Molecular Weight, Concentration, and Temperature in Segregation and Homogeneous Regimes. *Macromolecules* **1983**, *16* (7), 1093–1101.

(32) Hannon, Adam F., Bai, Wubin, Gotrik, Kevin, Alexander-Katz, Alfredo, Ross, C. Advances in Simulation Methods and the Theoretical Framework for Solvent Vapor Annealing of Block Copolymer Thin Film. *Unpublished*.

(33) Son, J. G.; Hannon, A. F.; Gotrik, K. W.; Alexander-Katz, A.; Ross, C. A. Hierarchical Nanostructures by Sequential Self-Assembly of Styrene-Dimethylsiloxane Block Copolymers of Different Periods. *Adv. Mater.* **2011**, *23* (5), 634–639.

(34) Takahashi, H.; Laachi, N.; Delaney, K. T.; Hur, S.-M.; Weinheimer, C. J.; Shykind, D.; Fredrickson, G. H. Defectivity in Laterally Confined Lamella-Forming Diblock Copolymers: Thermodynamic and Kinetic Aspects.

Macromolecules **2012**, *45* (15), 6253–6265.

(35) Fredrickson, G. H. The Equilibrium Theory of Inhomogeneous Polymers http://www.oxfordscholarship.com/view/10.1093/acprof:oso/9780198567295.001.0001/acprof-9780198567295.

(36) Fredrickson, G. H.; Ganesan, V.; Drolet, F. Field-Theoretic Computer Simulation Methods for Polymers and Complex Fluids. *Macromolecules* **2002**, *35* (1), 16–39.

(37) Hannon, A. F.; Bai, W.; Alexander-Katz, A.; Ross, C. A. Simulation Methods for Solvent Vapor Annealing of Block Copolymer Thin Films. *Soft Matter* **2015**.

(38) Renon, H.; Prausnitz, J. M. Local Compositions in Thermodynamic Excess Functions for Liquid Mixtures. *AIChE J.* **1968**, *14* (1), 135–144.

(39) Hamley, I. W. Nanostructure Fabrication Using Block Copolymers. *Nanotechnology* **2003**, *14* (10), R39–R54.

(40) Tu, K.-H.; Bai, W.; Liontos, G.; Ntetsikas, K.; Avgeropoulos, A.; Ross, C. A. Universal Pattern Transfer Methods for Metal Nanostructures by Block Copolymer Lithography. *Nanotechnology* **2015**, *26* (37), 375301.

(41) Tu, K.-H.; Bai, W.; Liontos, G.; Ntetsikas, K.; Avgeropoulos, A.; Ross, C. A. Universal Pattern Transfer Methods for Metal Nanostructures by Block Copolymer Lithography. *Nanotechnology* **2015**.

(42) Segalman, R. a. Patterning with Block Copolymer Thin Films. *Mater. Sci. Eng. R Reports* **2005**, *48* (6), 191–226.

(43) Cheng, J. Y.; Ross, C. A.; Chan, V. Z.-H.; Thomas, E. L.; Lammertink, R. G. H.; Vancso, G. J. Formation of a Cobalt Magnetic Dot Array via Block Copolymer Lithography. *Adv. Mater.* **2001**, *13* (15), 1174–1178.

(44) Thurn-Albrecht, T. Ultrahigh-Density Nanowire Arrays Grown in Self-Assembled Diblock Copolymer Templates. *Science (80-.).* **2000**, *290*, 2126–2129.

(45) Xiao, S.; Yang, X.; Edwards, E. W.; La, Y.-H.; Nealey, P. F. Graphoepitaxy of Cylinder-Forming Block Copolymers for Use as Templates to Pattern Magnetic Metal Dot Arrays. *Nanotechnology* **2005**, *16*, S324–S329.

(46) Black, C. T.; Guarini, K. W.; Sandstrom, R. L.; Yeung, S.; Zhang, Y. Formation of Nanometer-Scale Dot Arrays from Diblock Copolymer Templates. *MRS Proc.* **2002**, *728*, S4.9.

Chapter 4: In Situ Characterization of the Self-assembly of a Polystyrene-Polydimethylsiloxane Block Copolymer during Solvent Vapor Annealing

4.1 Abstract

In this chapter, we investigate self-assembly mechanism of a PS-PDMS BCP using in situ Grazing incidence Small angle X-ray scattering measurement with focus on the process-dependent evolution of microdomain orientation, lattice dimension and degree of ordering. Grazing incidence small angle X-ray scattering was used to follow the microphase separation during room-temperature solvent annealing of films of high interaction parameter cylinder-forming 16 kg/mol polystyrene-*b*-polydimethylsiloxane block copolymer in a toluene-heptane mixed solvent vapor. Microphase separation was observed for swelling ratios above 1.2, but swelling ratios above 1.9 caused the films to disorder. The films exhibited a thickness-dependent microdomain reorientation during annealing, with the initial out-of-plane cylinder orientation converting to an in-plane orientation as a result of preferential surface interactions. Drying led to a reduction in the out-of-plane cylinder spacing, with slower drying leading to greater deswelling and larger distortion of the hexagonal lattice. This work was published in Ref [1].

4.2 Introduction

In situ measurements of the microphase separation during annealing can provide insight into the kinetic processes that take place in the film. Solvent vapor annealing (SVA) has been demonstrated as a powerful method for controlling the order in BCP films, allowing control of microdomain morphology (due to the different selectivities between the solvent vapor and the blocks), the microdomain orientation, and the correlation length.[9,26] SVA can be carried out at room temperature, and combinations of heating and solvent exposure have produced microphase separation in annealing times of a few minutes or less.[11,27] Solvent vapor annealing can be described as taking place in three stages: i) solvent absorption, ii) solvent-BCP concentration equilibration, and iii) solvent desorption. Some solvent annealing methods only include stage i) and iii), [28] or iii).[29,30] However, the connection between the nanostructure formed in the swollen film and the final dried film is not well established,[31] and in situ characterization is needed to quantitatively analyze the self-assembly during SVA.

In stage i), solvent absorption swells the BCP film, decreases the Flory-Huggins interaction parameter χ, and reduces the entanglement of polymer chains, lowering the glass transition temperature of the BCP/solvent system and enhancing polymer diffusivity.[32,33] Solvent-swollen BCP systems can then rearrange, while the continuing absorption of solvent will influence the kinetic pathway for assembly. Prior work on the solvent absorption stage has shown the effect of swelling ratio (defined as swelled film thickness divided by as-cast film thickness) on the structural reorganization,[30,34,35] and the spacing and orientation evolution of both lamellae-forming[28,36] and cylinder-forming[37] block copolymers.

Once the solvent concentration in the film reaches equilibrium (stage ii), the effective χN and volume fraction as well as interface or surface interactions determine the morphology in the swollen state. In stage iii), solvent desorption increases the entanglement of polymer chains, and the BCP/solvent system traverses the glass transition temperature, locking in the self-assembled structure. The deswelling of the film may induce reorientation[38] and deformation or collapse of the microdomains as the film volume is reduced.[35] Dynamical field theory simulations demonstrated that reorientation was influenced by solvent desorption rate,[39] and the evolution of in-plane microdomain spacing and microdomain correlation length induced by solvent desorption was described for cylinder-forming polystyrene-*b*-poly2vinylpyridine.[35] For sufficiently high solvent fractions the film may become disordered, and solvent drying then results in an ordering front propagating through the film.[38] Previous studies have also described the evolution of microdomain spacing and correlation length during drying from the ordered swollen state.[35,40]

The microdomain morphology produced in a BCP film by SVA is therefore strongly affected by the film thickness and swelling ratio, substrate surface energy, solvent composition and vapor pressure, and solvent absorption and desorption rates. It is challenging to quantify how these numerous factors influence the self-assembly process. Many questions remain unanswered, including the nature of structural transitions and microdomain deformation during annealing, and changes in period and symmetry of the structure as the film dries. In-situ studies of BCP ordering using grazing-incidence small-angle X-ray scattering (GISAXS) can help in this regard, by resolving intermediate states and reconstructing the kinetic pathway that selects the final morphological states. In-situ GISAXS studies on solvent annealing of BCP thin films have focused on characterizing the swelling and deswelling of the BCP in the solvent vapor, and the associated structural transitions, reorientation and deformation or instability, usually with a single neutral solvent. [28,30,37,41–45] The solvent concentration was found to control the orientation of cylinders in polyisoprene-*b*-polylactide films [46,47], as well as the microdomain rearrangement of a lamellae-forming polystyrene-*b*-polybutadiene thin film.[36] Thin films of polystyrene-*block*-poly(ethylene oxide) complexed with salts yielded cylindrical microdomains oriented with their axes either in-plane (IP) or out-of-plane (OP) to the underlying substrate, with long-range lateral order after solvent annealing.[42,48] Pore evolution by block-copolymer self-assembly was also observed using time-resolved GISAXS.[49] These analyses have focused on BCPs with modest interaction parameter χ. The in-situ observation of the SVA ordering process for a high-χ block copolymer will provide an important comparison, and is particularly relevant to applications where a high χ enables scaling to small period structures. Further, in high χ BCPs, choice of selective solvents offers control over the morphology and period to produce non-bulk structures.[9] In situ studies of microdomain morphology and orientation are particularly important for enabling applications where microdomains with out-of-plane orientation are needed, because microdomains in high-χ BCPs often exhibit in-plane orientation due to large surface energy differences between the blocks.[50]

Polystyrene-*b*-polydimethysiloxane (PS-*b*-PDMS) is advantageous for forming microdomains with sub-10 nm period, because of its high χ (~0.27 at room temperature, though a recent analysis suggested 0.14).[51,52] Moreover, its etch resistance and etch selectivity make it useful in nanolithography applications. Here, we describe an in situ GISAXS study of SVA of a cylinder-forming PS-*b*-PDMS block copolymer using a mixture of selective solvent vapors. PS-*b*-PDMS produced excellent contrast in GISAXS between the organic PS block and the Si-containing PDMS, allowing the early stages of structural evolution to be characterized. At most of the SVA conditions studied, the BCP remained below the order-disorder temperature and the evolution of cylinder orientation and cylinder spacing was determined throughout the three stages of SVA in toluene-heptane vapor mixtures.

4.3 Experimental Methods

Experiments were conducted at the X9 beamline (National Synchrotron Light Source) using a custom cell into which solvent vapors were introduced. The BCP was PS-*b*-PDMS with molecular weight 16 kg/mol designated SD16, with $f_{\mathrm{PDMS}} = 0.31$, PDI = 1.08, and a bulk cylindrical morphology with nominal center-to-center spacing of 18 nm, spin-coated from cyclohexane onto oxidized silicon substrates. The initial film thickness was controlled by varying the SD16 solution concentration and spin speed. The solvent vapor was produced from a toluene: heptane mixture in a bubbler. The total volume of the solvent mixture and the nitrogen flow rate through the bubbler were tuned in order to control the solvent vapor pressure inside the cell and the film swelling was measured during the experiment by spectral reflectometry. A pure nitrogen flow was directly connected to the cell in order to control the solvent desorption rate. The structure was examined ex situ by SEM after etching the PS in oxygen to leave oxidized PDMS microdomains. Details of the experimental procedures are given in the Methods section and in Figure 4.7 in the supporting materials. Where there is a mixture of cylinder orientations in the film, the period for the IP and OP cylinders can be independently measured from the GISAXS data (see supplementary information and Fig. 4.12 for method). We define the periodicity as follows: for IP cylinders H_z is the distance between layers of cylinders and H_x is the center-to-center distance (for ideally closepacked cylinders $H_z/H_x = \sqrt{3}/2$) and for OP cylinders P_x is the center-to-center distance, nominally equal to H_x.

The poly(styrene-*b*-dimethylsiloxane) (PS-*b*-PDMS) diblock copolymer was purchased from Polymer Source Inc., Canada. The molar mass is 16.0 kg/mol, and the volume fraction of PDMS is f_{PDMS}~0.31 with polydispersity index 1.08. Solutions of the 16 kg/mol PS-PDMS were made in cyclohexane with concentration 1%, 3%, 5%, 10% and 15% respectively. Films with thickness ranging from 28 nm to 1.1 μm were obtained by spin coating on as-received Si substrates.

For the solvent vapor annealing, the equipment was similar to the flow system described by Gotrik et al.[8] Additionally a mass flow controller with 0-200 sccm range was added into the flow system in order to have a wide range of control on the solvent atmosphere. For in-situ GISAXS experiments, a custom solvent annealing cell was mounted inside the measurement chamber, Fig. 4.7. The small cell was air-tight and featured two Kapton windows, to allow the incident x-ray beam, and resultant x-ray scattering, to transit. The lid of the cell included a quartz window to allow real-time monitoring of film thickness via UV-VIS spectral reflectometry (Filmetrics). The cell also featured an inflow tube and solvent exhaust tube to allow for controlling the atmosphere within the chamber. The inflow tube was connected to a mixer fed by two flow channels: pure nitrogen for controlling the solvent absorption and desorption rate, and a solvent bubbler which contained a Toluene: Heptane 5:1 volumetric mixture. In order to obtain the highest solvent vapor pressure (process C, Fig. 4.2), 10 ml Toluene: Heptane 5:1 volumetric mixture was also added into the custom cell. Most of the annealing in this work was carried out during periods of 25 min to 85 min where the most dramatic structural changes took place. However it is likely that further annealing would lead to additional structural evolution and eventual dewetting of the film.

After annealing, a thin PDMS layer preferentially wetted the air/BCP film interface due to the lower surface energy of the PDMS block, and was removed by a short CF_4 reactive ion etch.[9] Then an O_2 plasma selectively removed the PS microdomains and converted the PDMS microdomains into a robust partially oxidized silica-rich nanopattern, which was imaged by scanning electron microscopy. The cross-sections were prepared by cracking the sample in liquid nitrogen followed by reactive ion etching, and imaged after tilting the sample 70^{o} to the SEM detector in order to show the morphology of both top and cross-section surface.

The time-resolved measurements provided by synchrotron GISAXS are capable of studying the buried BCP film morphology in a non-destructive way and represent averaged statistical significant microscopic information over a millimeter-size area.[65] GISAXS experiments were performed at beamline X9 of the National Synchrotron Light Source (NSLS) at Brookhaven National Laboratory. An incident x-ray beam of energy 14.1 keV (wavelength $\lambda = 0.8793$ nm) was collimated using a two-slit system, and focused to a beam 100 μm wide by 50 μm tall at the sample position using a Kirkpatrick-Baez (K-B) mirror system, using polished Si surfaces as mirrors. Samples were mounted inside a custom chamber compatible with solvent vapor flow-through, which was affixed to a motion-hardware stack for GISAXS alignment and measurement. The light interferometer was mounted to the cell so as to maintain alignment with the sample during scattering experiments. Grazing-incidence experiments were performed over a range of incidence angles, both below and above the film-vacuum critical angle. Two-dimensional scattering images were measured using either a charged-coupled device detector (MarCCD), or a hybrid pixel-array detector (Dectris Pilatus 1M). The SAXS detector was positioned at 5.274 m from the sample; data conversion to *q*-space was accomplished using Silver Behenate powder as a standard. Measurements were made every 2 minutes and the sample was translated between every two measurements to ensure that the results were not affected by cross-linking or other beam-induced damage.

4.4 Results and Discussion

We first describe the evolution of the structure of a film of SD16 with as-spun thickness of 241 nm in a vapor produced from a toluene:heptane 5:1 volumetric mixture, Figure 4.1 (Process A). Solvent vapor generated from the toluene: heptane 5:1 volumetric mixture resulted in approximately equal swelling of the PS block and PDMS block (see supporting information and Fig. 4.8), enabling us to track the formation of bulk-morphology cylindrical microdomains in situ in the swollen state. According to SEM, the as-spun film was poorly ordered, consisting of irregular micellar or short cylindrical features having a period of 12 - 16 nm. Corresponding GISAXS measurements confirm a poorly ordered structure, with $2H_z/\sqrt{3}$ considerably smaller than H_x. This is consistent with the as-cast state being a vertically collapsed structure that became ‘frozen-in’ as a result of the rapid solvent evaporation. During the solvent absorption stage (0 – 3 mins), solvent uptake swelled the film from 241 nm as-cast to 341 nm (swelling ratio SR = 1.41), and H_z increased dramatically from ~12 nm to ~17 nm, according to the scattering peak position in the q_z direction. However H_x only showed a slight increase of ~1 nm, based on the q_x scattering peak. The GISAXS peaks became sharper and more intense, indicating improvement in structural order. The swollen lattice of microdomains was considerably less distorted (i.e. $2H_Z/\sqrt{3}H_x$ was close to 1) than the as-cast state.

After 3 min SVA the swelling ratio was near 1.5 and well-defined cylinders were present, with coexisting IP and OP orientations of the cylinder axes. A weak ring in GISAXS connecting the IP and OP Bragg peaks indicated orientational disorder at this early stage of the ordering process; i.e. a small fraction of cylinders were oriented in directions other than IP or OP. This orientational disorder rapidly decreased as annealing proceeded, yielding a mixture of IP and OP orientations. As annealing proceeded, the fraction of OP cylinders decreased; after only 30 min, the cylinders were almost all oriented IP. The cylinder reorientation depended on both film thickness and annealing time, and will be described in more detail below. To complete the annealing process, the solvent vapor flow was stopped at 30 min and pure nitrogen was injected slowly (100 sccm for 5 mins and then 200 sccm for 15 mins) which resulted in film deswelling from a SR of 1.56 to 1.00. The higher ordering scattering peaks intensified as the solvent desorbed, due in part to an increase in the scattering contrast between the two BCP blocks as the solvent content in the film decreased. Solvent desorption led to a reduction in H_Z from 17 nm to 13 nm but H_x changed by only 1 nm (17 nm before solvent desorption, 18 nm after solvent desorption). The 1 nm changes were repeatable in several experiments. The solvent desorption rate affected the degree of structural deformation and will be described in more detail later. The final structure consisting of highly-ordered IP cylinders is shown in the SEMs labeled A6 in Fig. 4.1.

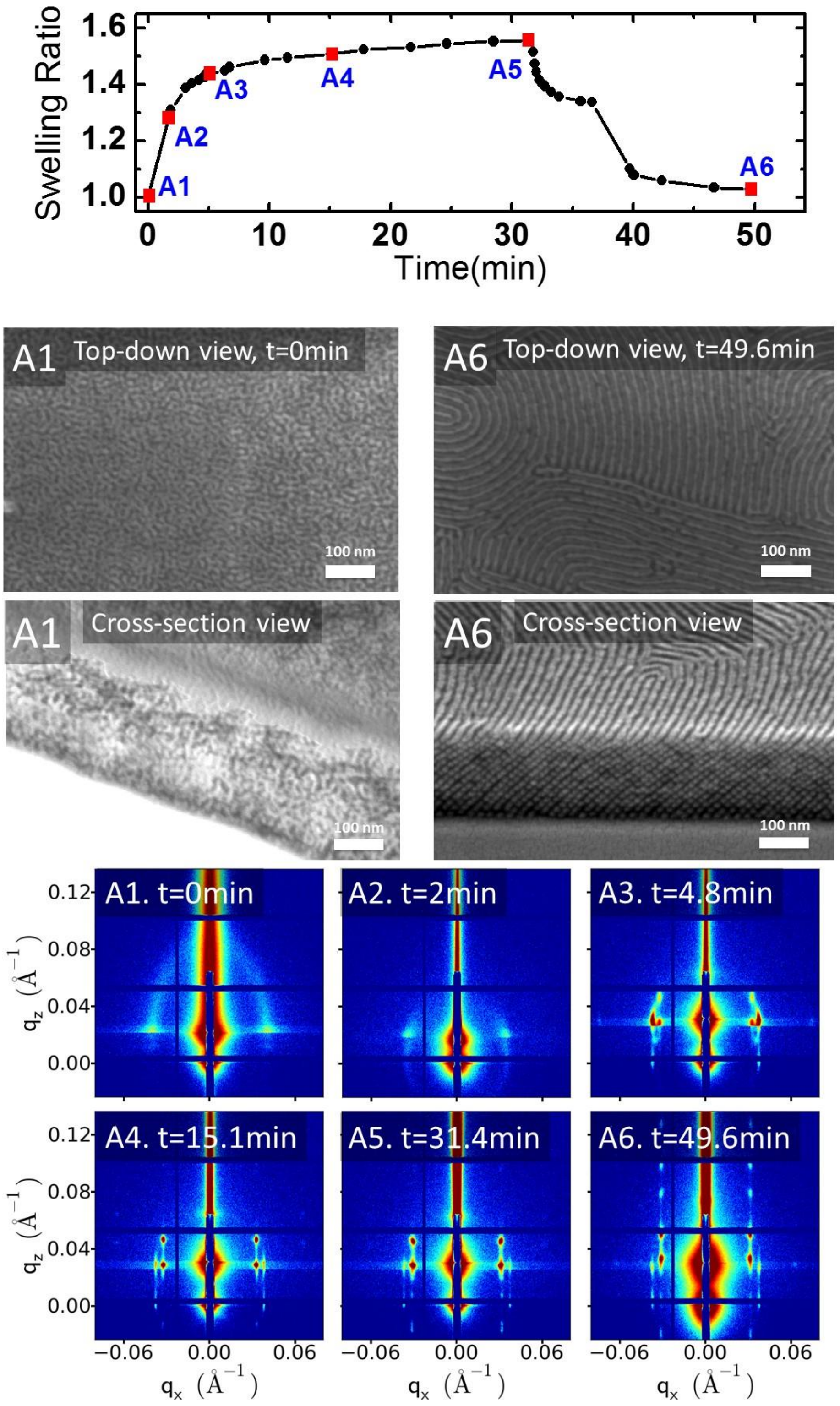

Figure 4.1. Process A: Solvent Vapor Annealing of a film of SD16 with as-spun thickness of 241 nm under solvent vapor produced from a toluene:heptane 5:1 volumetric mixture. The abrupt change in slope during deswelling (between A5 and A6) is a result of the change in nitrogen flow rate after the first 5 min of flow. The SEM images show the

as-cast film (A1) and the film after drying (A6) in top view and cross-sections. The GISAXS data correspond to times marked on the upper panel. The in situ measurement was done with help from Dr. Kevin Yager.

The effect of swelling ratio on the structural evolution was then investigated by changing the solvent flow rate and the total volume of solvent mixture in the reservoir compared to the conditions of process A. The solvent vapor pressure was at steady state before the sample was introduced into the annealing chamber with little disturbance to the solvent environment. Higher solvent vapor pressures resulted in faster swelling and higher saturation swelling ratio, as shown in Figure 4.2. For process C shown by the red line in Fig. 4.2, carried out at the highest swelling ratio using 10 sccm solvent flow through the bubbler and 10 ml additional solvent added in the sample cell, as the swelling ratio reached SR = 1.70, the GISAXS peaks representing hexagonally-packed cylinders became weaker and were replaced by a ring-shaped peak, which disappeared at SR = 1.88. This is interpreted as the disordering of the BCP film, i.e the order-disorder temperature (ODT) decreased to room temperature for the SD16 in the toluene:heptane 5:1 vapor at a critical swelling ratio of SR_C around 1.9. Both previous experiments and a theoretical model have demonstrated that vapor from a toluene:heptane 5:1 volumetric mixture induced a similar amount of swelling of PS and PDMS homopolymers (see supplementary information),[8,53] therefore we expect the effective volume fraction of PDMS in the swelled film at equilibrium to be similar to that of the neat BCP, and the dilution approximation is used to interpret the ODT in the swollen state. From the relation $\chi_{eff} = \chi(1 - f_s)^n$ where χ_{eff} is the effective interaction parameter, f_s is the fraction of solvent, which is known from the SR, n is an exponent taken as 1.6 for a high solvent concentration[54,55]. Common statistical segment volume v=0.118nm^3, the volume-averaged degree of polymerization, N = 160, and $\chi = 0.27$ (room temperature) for the SD16,[51,52,56] at SR_C we estimate $\chi_{eff}N = 15$. This is in good agreement with the χN of an ideal block copolymer with cylindrical morphology ($f = 0.31$) at its order-disorder temperature[57].

For lower vapor pressures (produced by 3 sccm flow through the bubbler, shown by the purple line process B in Fig. 4.2), the swelling ratios remained small. At SR = 1.11 the structure was still a poorly ordered worm-like structure resembling the as-cast morphology, but with a larger H_z of ~14 nm compared with the as-cast film H_z ~12 nm. At SR = 1.17 the interface between blocks became sharper as the scattering peaks intensified. At larger swelling ratios, e.g. SR = 1.23, peaks characteristic of cylinders appeared, and the order and correlation length improved with increasing SR. Therefore a SR of at least ~1.2 was required to give sufficient mobility for cylindrical microdomains to form in the 241 nm thick film, but above SR ~1.88 the BCP became disordered. This defines an optimal window for SVA to be productive with respect to improving structural order. The film must uptake enough solvent to induce mobility and allow rearrangement of the morphology; but must not drive the system into the disordered part of the phase diagram.

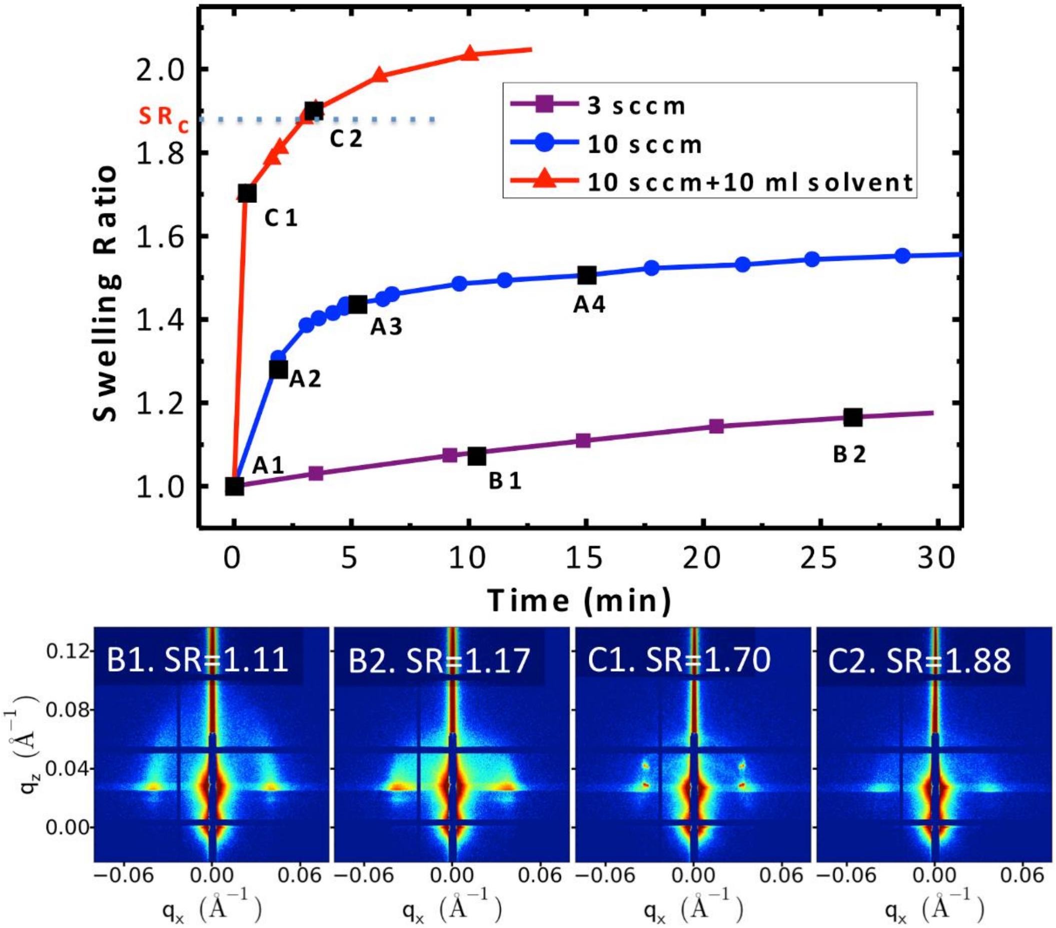

Figure 4.2. GISAXS during the solvent absorption stage for three different solvent vapor pressures achieved by varying the gas flow through the bubbler or adding additional solvent into sample cell. As-cast film thickness was 241 nm. The SD16 films were annealed under solvent vapor from a Toluene: Heptane 5:1 volumetric mixture. GISAXS data corresponds to the times marked on the plot of swelling ratio vs. times for processes B and C. $SR_c = 1.88$ indicates the swelling ratio at which the BCP passed through its order-disorder temperature. GISAXS data of process A was given in Fig. 4.1. The in situ measurement was done with help from Dr. Kevin Yager.

We now describe the effect of film thickness in the regime of swelling ratio below SR_c where a well-ordered cylindrical morphology formed in the swollen state. Films with as-cast thickness from 28 nm to 1141 nm are compared in Fig. 4.3, which shows SEM images of the dried films, and Fig. 4.4, which shows the swelling ratio and cylinder orientation vs. time. Figs. 4.9, 4.10, and 4.11 show some of the GISAXS data. For the film with 28 nm as-cast thickness, commensurate with a monolayer of IP cylinders, a swelling ratio of 1.15 produced good order (Figs. 4.3a and 4.10), but for the thicker films a SR around 1.5 was used. The time required for the swelling ratio to stabilize at SR ~ 1.5 increased with film thickness.

The post-SVA morphology of the thinnest film, Fig. 4.3a, consisted of IP cylinders, whereas the other films exhibited coexisting IP and OP cylinders. All the samples had one or a few layers of IP cylinders at the top surface. After 1 hour anneals, Fig. 4.3g, highly oriented OP cylinders were present in a 1.1 μm thick film (except at the top surface) but in a 241 nm thick film, IP cylinders were the majority, Fig. 4.3c.

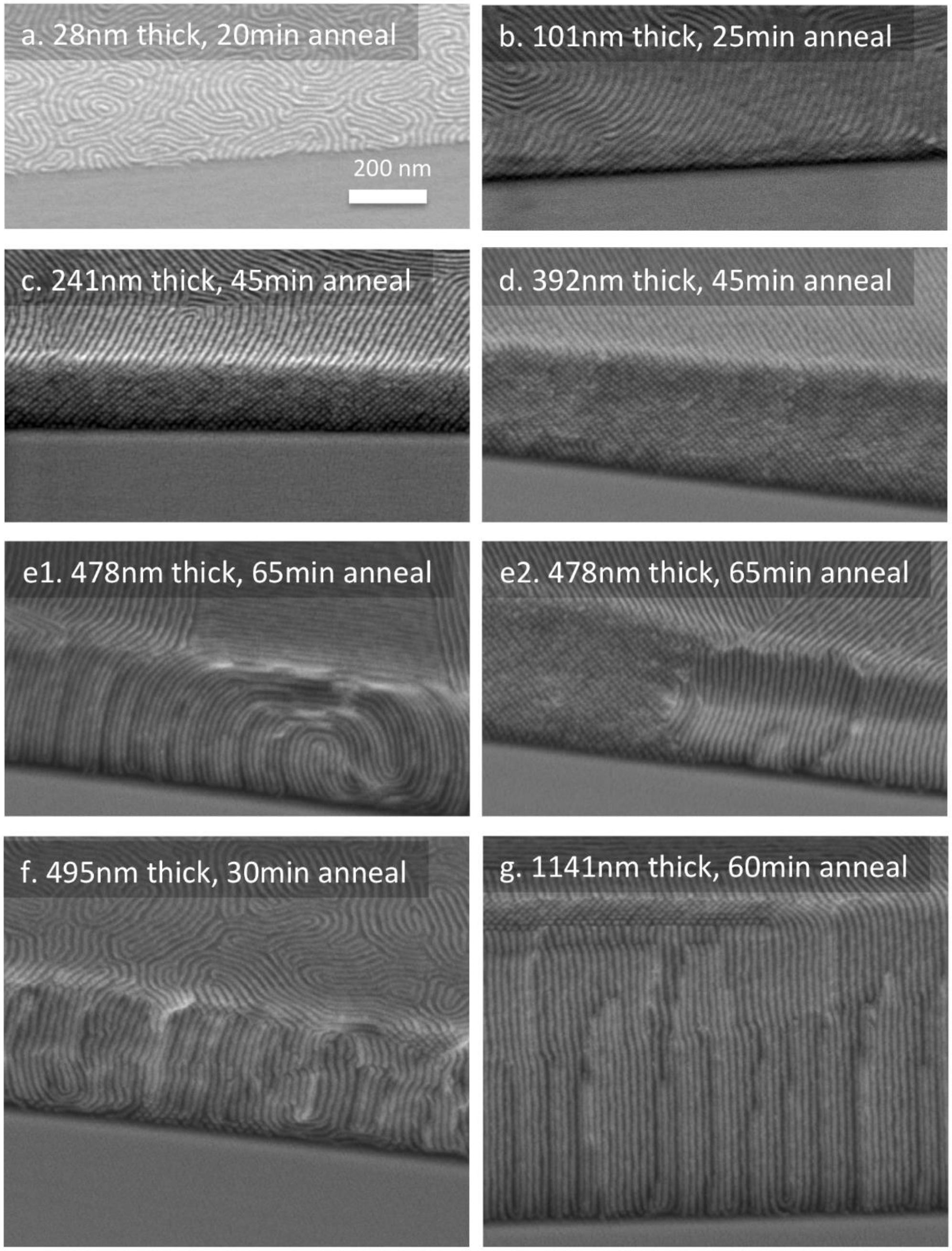

Figure 4.3. SEM of final etched morphologies of films with different thickness: (a) 28 nm as-cast thickness, 20 min anneal, same sample as described in Fig. 4.10; (b) 101 nm as-cast thickness, 25 min anneal, same sample as described in Fig. 4.4a; (c) 241 nm as-cast thickness, 45 min anneal, same sample as described in Fig. 4.1, Fig. 4.2a and Fig. 4.4b; (d) 392 nm as-cast thickness, 45 min anneal, same sample as described in Fig. 4.4c; (e1), (e2) are two pieces of the same film with 478 nm as-cast thickness and 65 min anneal, same sample as described in Fig. 4.4d; e1 shows typical defects in OP cylinders, and e2 shows the boundary between IP and OP cylinders. (f) 495 nm as-cast thickness, 30

min anneal, same sample as described in Fig. 4.11; (g) 1141 nm as-cast thickness, 60 min anneal, same sample as described in Fig. 4.4e.

Fig. 4.4 shows the calculated fractions of IP and OP cylinders for each film thickness as a function of time based on the GISAXS data. The 28 nm thick film (Figs. 4.3a and 4.10) and the 101 nm thick film (Figs. 4.3B and 4.4A) maintained IP cylinders throughout the anneal. However, for 241 nm and 392 nm films, the samples initially had an OP-dominated orientation and the IP orientation did not develop until part way through the anneal (Fig. 4.4b,c). For the even thicker films (Fig. 4.4d,e) the orientation remained OP throughout the anneal. These results are consistent with the SEM images, where the fraction of OP cylinders in the annealed films increased with thickness.

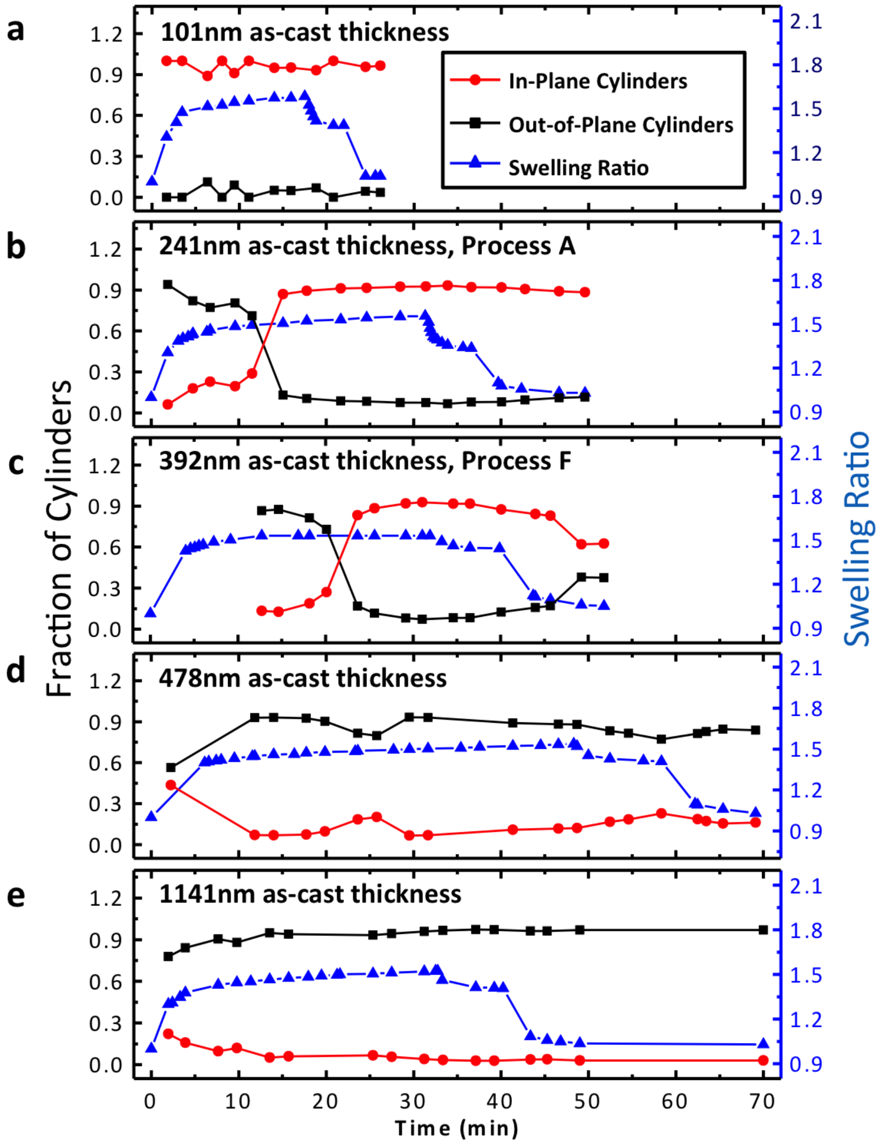

Figure 4.4. Evolution of the fractions of in-plane and out-of-plane oriented cylinders and the film swelling ratio with time in SD16 films with as-cast film thickness (a) 101 nm, (b) 241 nm, (c) 392 nm, (d) 478 nm, (e) 1141 nm. The samples were annealed under solvent vapor evaporated from a Toluene: Heptane 5:1 volumetric mixture. The in situ measurement and analysis were done with help from Dr. Kevin Yager.

The reorientation of the cylinders is assumed to proceed via curved intermediate structures as shown on Fig. 4.3e1 for the 478 nm film. A comparison of Figs. 4.3e2 and 4.3f, where films of similar thickness (~480nm) were annealed for different times, 65 and 30 min respectively, shows that the longer anneal produced straighter, less defective cylinders, and apparently an increase in the fraction of IP cylinders. Fig. 4.4d also shows a small increase in the fraction of IP cylinders between 30 min and 60 min. The GISAXS and swelling data for the sample of Fig. 4.3f is shown in Fig. 4.11.

These results can be explained if the IP orientation is favored by interface interactions. This is a result of the difference in surface energy between PDMS ($\gamma_{PDMS} \approx 20.4$ mN m^{-1}) and PS ($\gamma_{PS} \approx 40.7$ mN m^{-1}), which causes a thin PDMS wetting layer to be present at the top surface,[9] promoting in-plane cylinder alignment. Interface interactions are dominant in the thinnest films even in the early stages of annealing. However, initial formation of OP cylinders was more prevalent in thicker films, suggesting it may be kinetically determined by the solvent concentration gradient throughout the film thickness during the swelling.[45] On annealing, the OP orientation changed to IP, but for the annealing times studied here, this reorientation only occurred fully for the 241 nm and 392 nm films, and partly or not at all for the thickest films. For the 392 nm film, there is also evidence of a reverse IP to OP reorientation during deswelling (Fig. 4.4c), which may be a result of solvent gradients during that stage of the anneal. Conversely, the thicker films do not appear to reorient during deswelling, leading to a final dry-state dominated by OP cylinders. Prior work has shown that a solvent concentration gradient established during solvent desorption can facilitate OP cylinder formation,[45,58] including in films annealed with a topcoat.[50]

The rate of solvent desorption was also important in determining the final morphology and period of the films, the cylinder orientation and the sharpness of the microdomain interfaces. Fig. 4.5 shows the results of annealing a 241 nm thick film with different annealing times and solvent removal rates. Processes E, A, and D started from an ordered state with SR ~ 1.5. The films were swelled for 10 min, 30 min and 25 min for processes E, A, D respectively and similar morphologies (most cylinders oriented IP, with a small fraction OP) formed in the swollen state. Then nitrogen was introduced to deswell the film at different rates, with process E the fastest solvent removal (5 min) and process D, a two-step solvent removal process in which the film was held at SR = 1.35 for 4.5 hrs. In contrast, in process C the film was deswelled from a disordered state with SR > SR$_c$ after a 15 min anneal. The initial part of the annealing of process C was shown in Fig. 4.2.

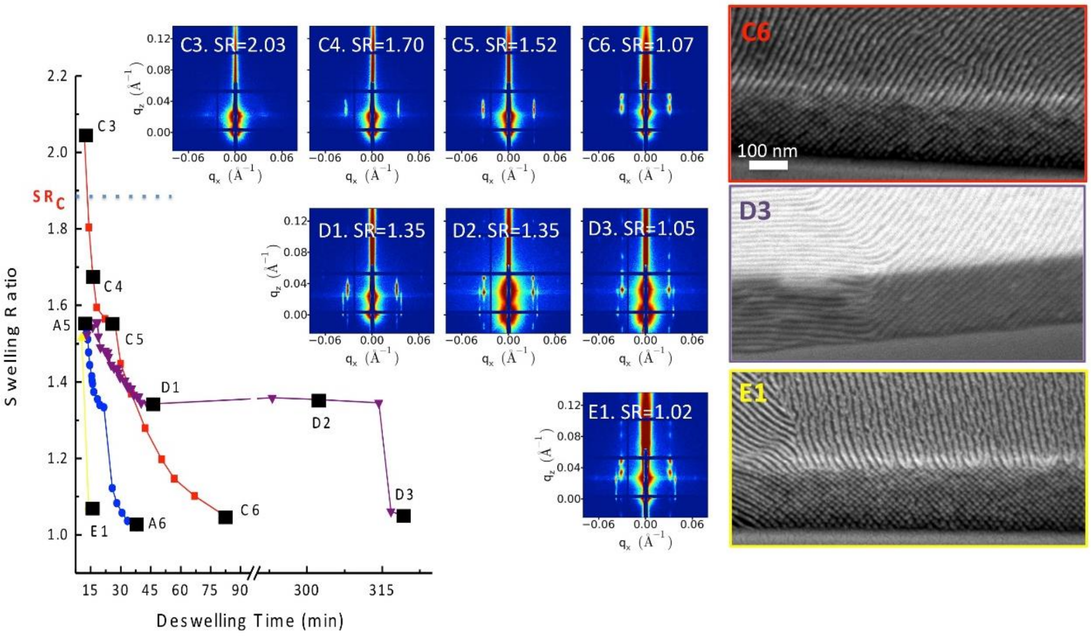

Figure 4.5. GISAXS measurements during solvent desorption for as-cast film thickness of 241 nm and solvent vapor evaporated from a Toluene: Heptane 5:1 volumetric mixture. In process C, the film was annealed at high solvent vapor pressure to give SR = 2.05 and quenched by 100 sccm nitrogen flow. The initial part of process C was shown in Fig. 4.2. The solvent desorption started after 15 min annealing. The purple-line, blue-line, and green-line processes D, A and E respectively were annealed at an intermediate solvent vapor pressure to give SR ~1.55 but quenched at different nitrogen flow rates: purple-line process D, 50 sccm for 5 h and then 200 sccm nitrogen; blue-line process A, 100 sccm for 5 mins and then 200 sccm for 15 mins; green-line process E, 200 sccm. For processes D, A, E, the initial part of the annealing was carried out the same as process A in fig. 4.2. Solvent desorption started after 25 min annealing for D, 30 min annealing for A, and 10 min annealing for E. This in situ measurement was done with the help from Dr. Kevin Yager.

Comparing the final morphologies, processes E, A, and D produced IP cylinders but the surface roughness of the cylinders was greater for process E with fastest solvent removal. In process C, deswelling from the disordered state, the cylinders appeared at SR ~1.7 with IP orientation. We assume IP cylinders appeared first at the top surface of the film as the ordering interface moved down through the film as the solvent dried slowly. Other studies have also showed a structural transition and reorientation due to solvent removal starting from the disordered swollen state.[38,59]

Figure 4.6 shows in detail the evolution of the geometry of the microdomain array during the three different annealing processes E, A and D of Fig. 4.5. The left column of panels in Fig. 4.6 shows the data corresponding to processes E and A of Fig. 4.5, while the right column of panels corresponds to the slower process D of Fig. 4.5. In all three, the state at SR = 1.5 consisted mainly of IP cylinders and a small fraction of OP cylinders. We can define a distortion factor $DF = 2H_z/(\sqrt{3}H_x) = 1$ for IP cylinders when the array is ideally close packed, > 1 when it is expanded out of plane, and < 1 when it is compressed in the OP direction. Prior to deswelling, the films had DF = 1.1, 1.0 and 0.95 for processes E, A, D respectively. Thus, in the swollen state, the BCP forms a nearly ideal close packed unit-cell symmetry, due to the high mobility of the chains in this state.

The in-plane spacing of the cylinders (H_x or P_x) in the swelled state was ~19 – 20 nm. At equilibrium the BCP period is expected to decrease slowly with increasing SR because the solvent, which is present in both blocks, effectively lowers χ and thus the period. These changes in period occur via a change in the number of domains. However, during transient swelling before the system has equilibrated, the addition of solvent increases the microdomain volume without changing the number of domains, and hence the periodicity increases. Both these factors contribute to the change in period throughout the SVA process, and the time-dependence of the period will depend on the timescale of volume changes vs. BCP rearrangement. The small (< 1 nm) increases in H_x and P_x as the SR decreased, Fig. 4.6(b) are attributed to the solvent-induced increase in χ. In contrast the dramatic decrease in H_z was dominated by volume reduction on deswelling.

The changes in H_z depended on the rate of solvent desorption. For process E with fastest deswelling, the solvent removal resulted in a ~4 nm decrease in H_z to a value of ~15 nm. For process A, deswelling resulted in a ~5 nm decrease in H_z to a value of ~14 nm. For process D with a 4 hour hold at SR = 1.35, deswelling resulted in a ~6 nm decrease in H_z to a value of ~11 nm. Notably the first, slow part of the deswelling in process E raised H_z slightly, then the second solvent removal step lowered H_z. The increase in H_z in the first part suggests coalescence of cylinders to reduce the total number of layers of cylinders as χ increased, which can occur because the block copolymer still has considerable mobility. In the second solvent removal step the mobility presumably became too low for appreciable domain rearrangement, and the change in H_z was dominated by volume reduction arising from solvent loss.

Swelling and deswelling caused much greater changes in H_z compared to those in H_x and P_x because changes in film volume can only be accommodated by vertical expansion or contraction of the film. The distortion factors in all three solvent removal processes dropped below 1, reaching 0.85, 0.78 and 0.62 in the dry state for processes E, A, D respectively. Therefore, all the IP cylinder arrays showed a compressive out-of-plane distortion such that the angle between the horizontal and tilted layers of cylinders, which would be 60° for an ideal close-packed array, was 56.3°, 52.6° and 48.0° for processes E, A, D respectively. Therefore in this experiment, slower drying led to greater collapse in the z-direction and a more distorted final array. In the case where the BCP chains still have enough mobility due to the remaining solvent in the film, extremely slow drying may lead to an increase in H_z due to the dominance of the increase of effective χ.[35]

The distorted unit-cell after final drying of the film therefore represents a non-equilibrium configuration formed by collapse of the film. In principle, sufficiently slow deswelling should give time for the BCP to rearrange and form an undistorted morphology at the new, unswollen period. What we instead observed is that the decrease in polymer mobility during solvent evaporation was too severe to allow for this reconfiguration. Instead, the films retained the in-plane periodicity of the swollen state, and collapsed in the out-of-plane direction, thus adopting a distorted unit-cell.

Finally, the correlation length (grain size) for IP cylinders was calculated using the scattering peak width. This increased during annealing at constant SR representing grain growth, but decreased during deswelling, presumably because the BCP rearrangement to accommodate film volume shrinkage degraded the long range order of the microdomains. For example, process A achieved a larger correlation length (1.6 μm) for the IP cylinders than process E during steady state swelling, because process A spent a longer time at SR = 1.5, but after deswelling, both samples had correlation lengths of 0.8 μm. Process D reached a correlation length of 2 μm during steady state swelling at SR = 1.35, but this decreased to 0.8 μm after deswelling. Previous studies[60–64] have found a power law behavior at equilibrium between the ordering grain size (correlation length) and annealing time in thermal annealing of e.g. a cylinder-forming PS-PI diblock copolymer, with exponents between 0.1 and 1. The SVA processes here do not represent equilibrium, but fitting the data for process A and process F (before the solvent removal) gave exponents of 0.8 ± 0.13 and 1.20 ± 0.15, respectively, for correlation length vs. time, shown in Fig. 4.6f.

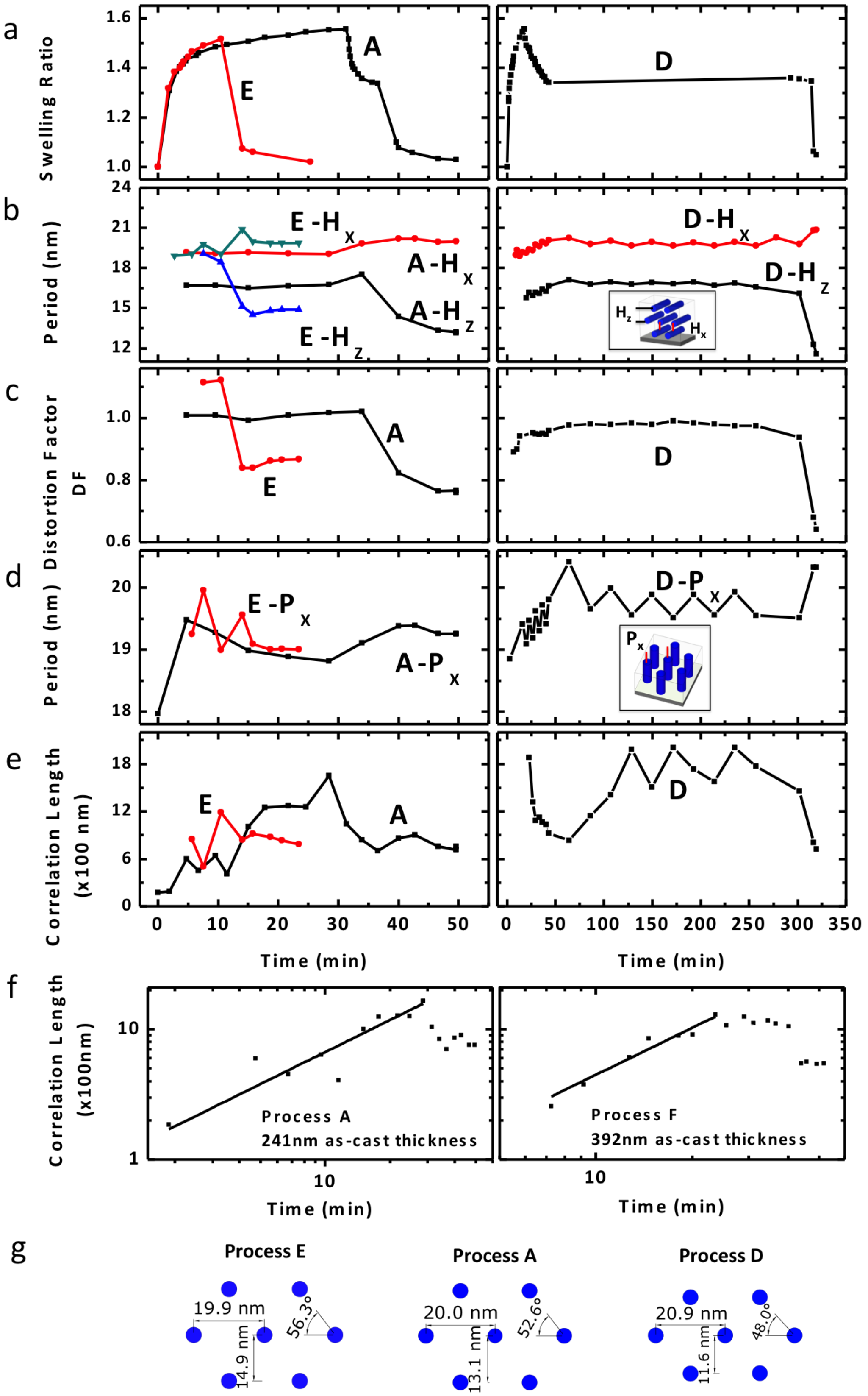
a
Swelling Ratio
1.0
1.2
1.4
1.6
A
E
D
b
Period (nm)
12
15
18
21
24
E -H_X
A -H_X
A -H_Z
E -H_Z
D -H_X
D -H_Z
H_z
H_x
c
Distortion Factor DF
0.6
0.8
1.0
A
E
D
d
Period (nm)
18
19
20
E -P_X
A -P_X
D -P_X
P_x
e
Correlation Length (x100 nm)
0
6
12
18
E
A
D
0
10
20
30
40
50
Time (min)
0
50
100
150
200
250
300
350
Time (min)
f
Correlation Length (x100nm)
1
10
Process A
241nm as-cast thickness
Process F
392nm as-cast thickness
10
Time (min)
10
Time (min)
g
Process E
19.9 nm
56.3°
14.9 nm
Process A
20.0 nm
52.6°
13.1 nm
Process D
20.9 nm
48.0°
11.6 nm

Figure 4.6. Quantitative analysis of evolution of swelling ratio, microdomain spacing, and correlation length or grain size as function of time. (a) In-situ swelling ratio measurement for processes E, A, D; (b) Evolution of period H_x and H_z of in-plane oriented cylinders for processes E, A, D; (c) Distortion factor for processes E, A, D; (d) Evolution of period P_x of out-of-plane oriented cylinders for processes E, A, D; (e) Correlation length as function of time for processes E, A, D; (f) Power law relation between correlation length and annealing time for process A; (g) Schematic plot of final distorted structure of in-plane cylinders for processes E, A, D. The in situ measurement and analysis were done with help from Dr. Kevin Yager.

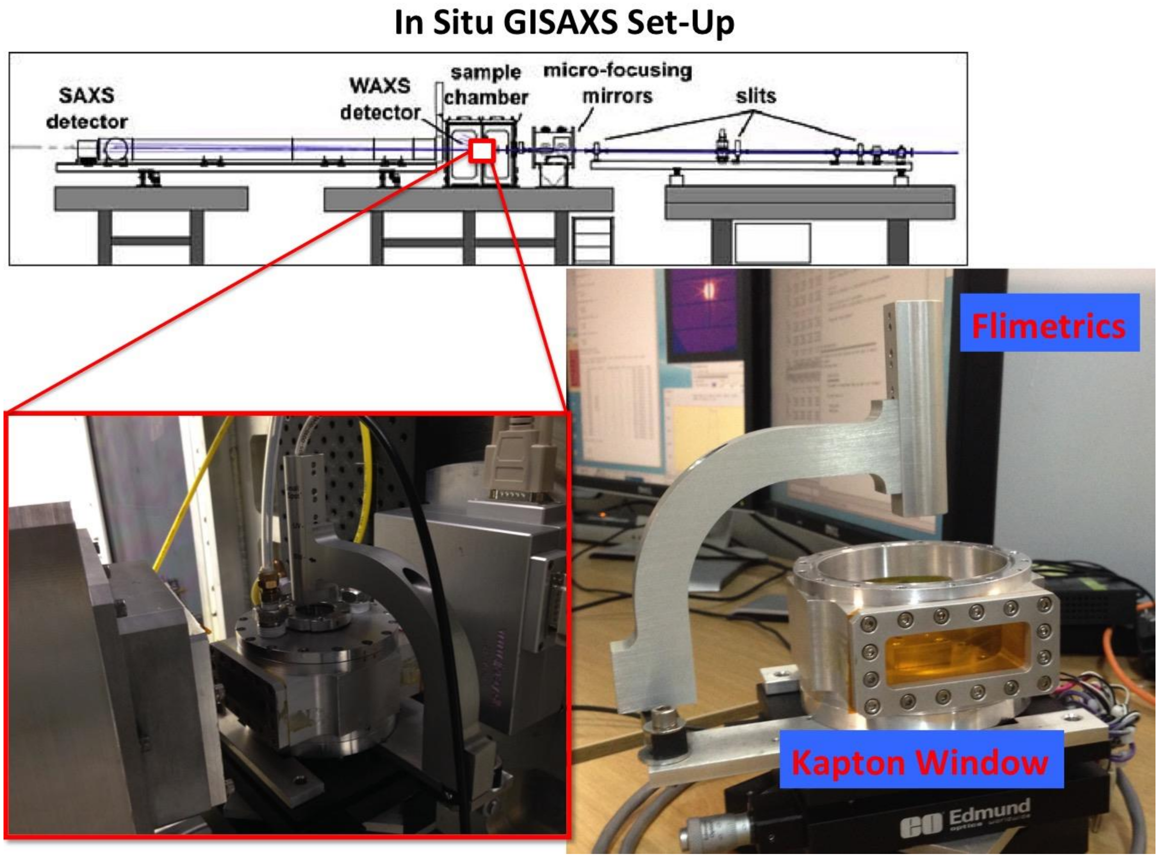

Figure 4.7. In Situ GISAXS experimental set-up for block copolymer solvent vapor annealing.

4.5 GISAXS data analysis

Grazing-incidence small-angle x-ray scattering (GISAXS) data were analyzed to obtain the lattice constants of the BCP hexagonal unit-cell, as well as the average grain size, and an estimate of the relative amounts of cylinder grains oriented in-plane vs. out-of-plane. GISAXS detector images were converted into reciprocal-space (q-space) using a standard sample with scattering rings at known q (silver behenate). To determine lattice constants, linecuts through the two-dimensional GISAXS images were taken. For the in-plane periodicity of the out-of-plane (vertically-oriented) cylinder population, a horizontal cut along the Yoneda, and through the 1st GISAXS peak, was used (the intensity along the Yoneda improves the signal-to-noise of this determination). The peak was fit using a Gaussian with a power-law background (to account for, e.g. diffuse scattering), in order to obtain the peak center position (q_x) and peak width (Δq). This peak arises from the out-of-plane (vertically-oriented) cylinder population, and its q-value can be used to compute the cylinder layering distance $L_x = 2\pi/q_x$. The corresponding cylinder-cylinder distance can be computed, for a hexagonal unit-cell, as $P_x = L_x \sqrt{3}/2$. For the in-plane cylinder population (horizontal orientation), the 1st peak above the Yoneda was used. This peak appears as a doublet in GISAXS, owing to the multiple possible scattering events, as described within the distorted-wave Born approximation (DWBA) framework.[66,67] We analyzed the peak centered about the direct-beam (rather than the reflected beam); i.e. the 'transmission channel'.[68] A horizontal linecut was used to determine the q_x position of this peak, which gives the in-plane periodicity H_x of this in-plane (horizontal cylinder) population. To determine the out-of-plane (film normal direction) spacing of this population, the q_z center of this same peak is obtained via a fit to a Gaussian function with a background. In this case, the peak position is corrected to account for the refraction-induced distortion to reciprocal-space, using the known incidence-angle and an estimate of the x-ray refractive index of the film (at 14.1 keV). The equations for this correction are well-known,[66,68–72] and ultimately result from the application of Snell's law to the grazing-incidence geometry. Note that solvent uptake by the film would be expected to modify the refractive index; however, this change is subtle since the refractive index of the polymer film and of a bulk organic solvent are similar (especially compared to the $n = 1.0$ refractive index of the ambient environment). The (corrected) q_z component of this 'diagonal' peak is exactly half the q_z value of the purely out-of-plane peak (which is hidden behind the beamstop/specular-rod). Thus, we compute the cylinder layering distance along the film-normal as $H_z = 2\pi/(2q_z)$.

The average in-plane grain sizes were estimated by extracting the correlation-length using a Scherrer peak-width analysis applied to the q_x linecut.[73] Heuristically, broad peaks correspond to short distances over which positional order is maintained in the hexagonal cylinder lattice, whereas sharp peaks indicate large distances. The Scherrer analysis was performed taking into account the peak-broadening contributions from instrumental effects (wavelength spread of incident radiation, divergence of microfocused beam, detector pixel size), as well as the geometric broadening resulting from the grazing-incidence geometry.[74]

The amounts of cylinders oriented in-plane vs. out-of-plane was estimated using the intensity of the corresponding scattering peaks. For each image, the full integrated intensity of the aforementioned peaks was computed, after the corresponding local background was subtracted. The q_x peak along the Yoneda arises purely from the out-of-plane population, whereas the peak above the Yoneda arises from the in-plane population. The scattering intensity of a peak is linearly proportional to the amount of material that contributes to it (strictly, proportional to the scattering volume; i.e. the intersection between the beam and the given sub-population). We assume that our samples resemble in-plane powders (no preferred in-plane direction, confirmed by SEM images). Owing to the intersection of the Ewald sphere with reciprocal-space, the scattering peaks we observe arise from rings in the full three-dimensional reciprocal-space. This applies to both peaks of interest; thus, to a first approximation, no correction of intensities is necessary. The relative integrated intensities of the scattering peaks can be used as an estimate of the relative amounts of the two populations. We note that a $\sin(\chi)$ factor, where χ is the angle with respect to the q_z axis, can be applied to account for the slightly different reciprocal-volume each peak represents.[75,76] This suggests a relative correction-factor (for out-of-plane population relative to in-plane) of $\sin(60\,^{\circ})/\sin(90^{\circ}) \approx 0.9$. Conversely, the q_x peak (vertical cylinders) arises from the in-plane averaging of 6 diffraction peaks, while the q_z peak (horizontal cylinders) arises from the in-plane averaging of 2 diffraction peaks, imposing a correction factor of 6/4 = 1.5. These two effects tend to offset one another: the combined correction is ~1.3. Finally, we note that the grazing-incidence intensity enhancement may not be strictly identical for the two peaks of interest. Despite performing a local background subtraction for each peak (and thus removing the baseline intensity of the Yoneda band), the q_x peak may have a somewhat higher intensity enhancement, owing to its lower exit angle (this would impose a correction <1.0). Thus, while we interpret the relative scattering intensities as fractions of the two corresponding cylinder populations, we acknowledge a small systematic bias in the reported values. As such, we only attempt to interpret these values in a relative sense, in order to establish trends, and do not claim that the absolute population fractions are known unambiguously.

4.6 The Swelling Behavior of PS-PDMS in vapor from a Toluene: Heptane 5:1 volumetric liquid mixture

In this work, 2500 cm^3 toluene: heptane 5:1 volumetric liquid mixture was used in the bubbler of the solvent flow system. A decrease of liquid level in the bubbler was not found in the 5-hour annealing test, which indicated that the amount of solvent that was evaporated from the bubbler was small and the composition of the vapor therefore remained constant. The mole fractions of toluene and heptane in the vapor phase generated from a Toluene: Heptane 5:1 volumetric solvent mixture are: [8]

$$y_{tol} = \frac{p_{tol}^*}{p_{total}}$$

$$y_{hep} = \frac{p_{hep}^*}{p_{total}}$$

where p_{tol}^* and p_{hep}^* are partial vapor pressures of tolune and heptane, and $p_{total} = p_{tol}^* + p_{hep}^*$.

Based on Raoult's Law for non-ideal mixing, the partial pressures of toluene and heptane are:

$$p_{tol}^* \phi_{tol} = p_{tol} \gamma_{tol} x_{tol}$$

$$p_{hep}^* \phi_{hep} = p_{hep} \gamma_{hep} x_{hep}$$

where ϕ_{tol} and ϕ_{hep} are fugacity coefficients of toluene and heptane; γ_{tol} and γ_{hep} are activity coefficients, and x_{tol} and x_{hep} are the mole fractions in the liquid solution. p_{tol} and p_{hep} are the vapor pressures of pure solvents.

For the situation of heptane diluted in toluene, $\gamma_{hep} \sim 1.4$ and $\gamma_{tol} \sim 1$,[77] and assuming ϕ_{tol} and ϕ_{hep} are equal,[78] a 5:1 volumetric ratio of toluene and heptane liquid mixture approximately corresponds to a mole ratio of 6.89: 1 toluene: heptane.

Therefore,

$$y_{tol} = \frac{p_{tol}^*}{p_{total}} \sim 0.73$$

This fraction of toluene in the vapor is close to the regime found in prior work where PS and PDMS homopolymers have equal swelling ratio for mixtures of saturated total vapor pressure, as shown in figure 4.8a which is reproduced here for convenience.[8]

In a computational approach based on the effective volume fraction in the BCP as a function of solvent vapor composition,[53] we found that a toluene mole fraction in the vapor of around 0.68 gave an effective volume fraction of PDMS equal to that in the bulk BCP (*f* = 0.33), as shown in figure 4.8b, reproduced here for convenience.

Based on these results, we see that the vapor generated from a toluene: heptane 5:1 volumetric mixture, which has a toluene mole fraction in the vapor of ~0.7, swells both blocks equally so that the effective volume fraction f in the swelled state is the same as the dry volume fraction.

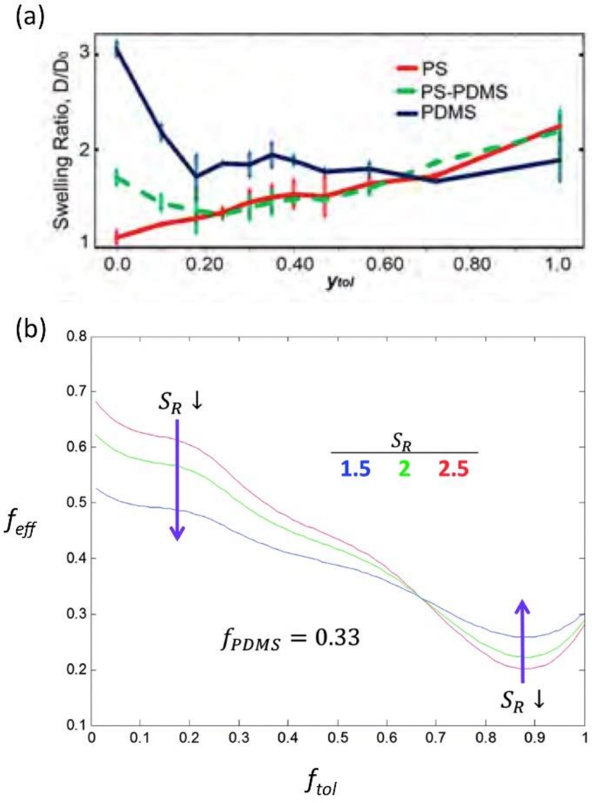

Figure 4.8. (a) Swelling ratios of PS, PS-PDMS, and PDMS for different mole fraction of toluene in a toluene and heptane vapor mixture. The plot is reproduced from [8]; (b) Plots of f_{eff} using fitted selectivity parameters for toluene and heptane solvents in PS-PDMS BCPs with given volume fraction of PDMS $f = 0.33$ for three values of swelling ratio S_R=1.5, 2, and 2.5. Plot is reproduced from [53].

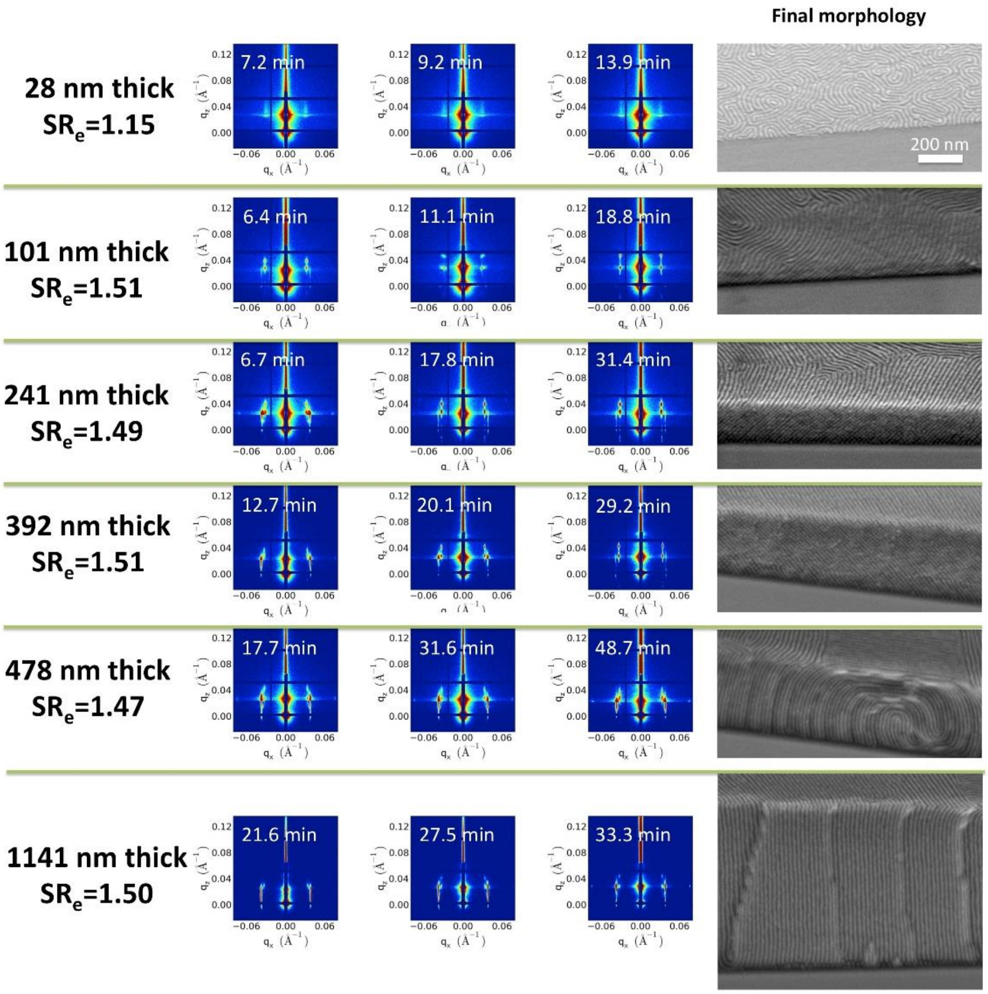

Figure 4.9. GISAXS at the solvent-BCP concentration equilibration stage, in PS-*b*-PDMS films with as-cast film thickness 28 nm, 101 nm, 241 nm, 392 nm, 478 nm, 1141 nm, annealed under solvent vapor from a reservoir of Toluene: Heptane 5:1 volumetric mixture. The equilibrium swelling ratio was recorded for each sample, and the final etched morphology was imaged by SEM. The in situ measurement was done with help from Dr. Kevin Yager.

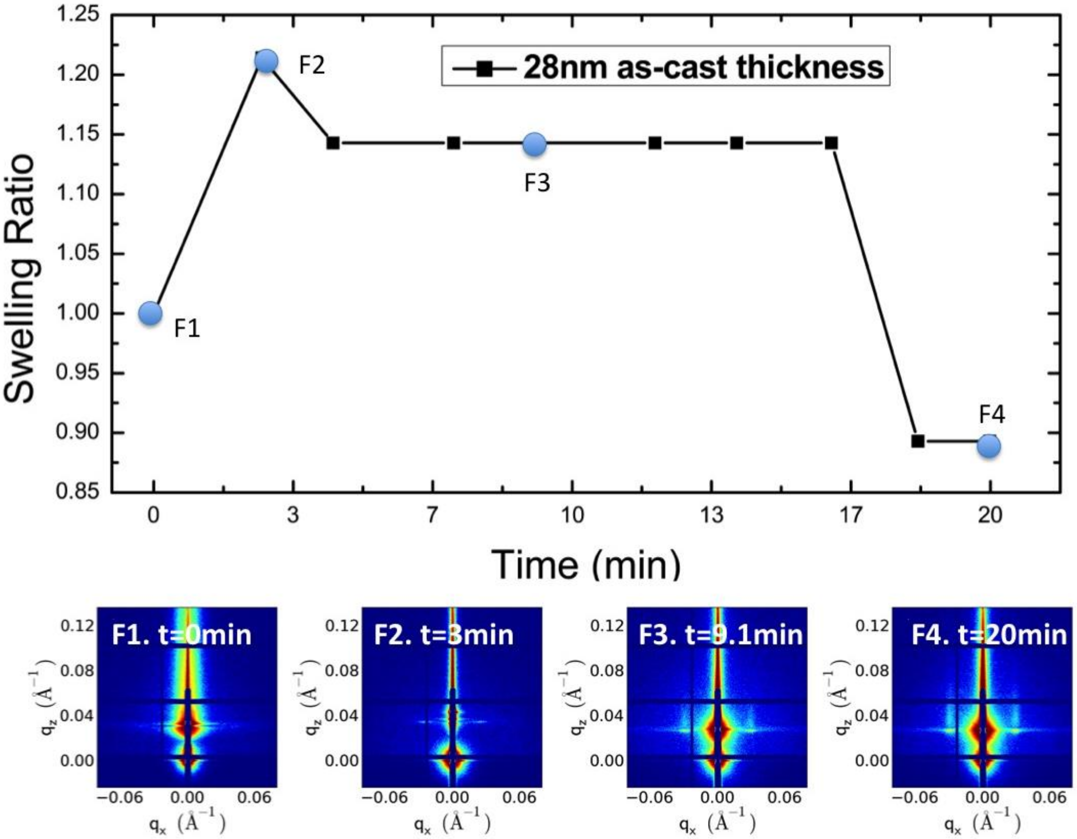

Figure 4.10. In Situ swelling ratio of SD16 PS-*b*-PDMS thin film with as-cast film thickness 28 nm (process F) under solvent vapor produced from Toluene:Heptane 5:1 volumetric mixture. F1, F2, F3, F4, in situ GISAXS measurements. The in situ measurement was done with help from Dr. Kevin Yager.

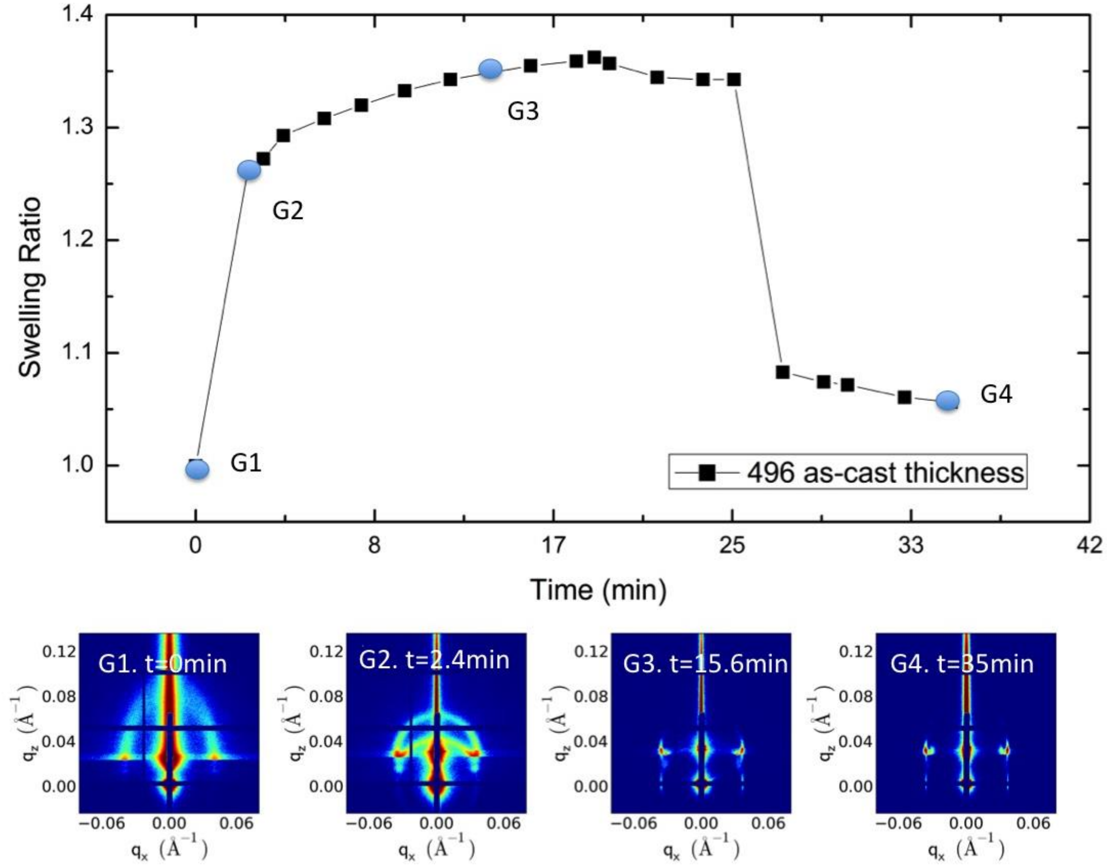

Figure 4.11. In situ swelling ratio of SD16 PS-*b*-PDMS thin film with as-cast film thickness 496 nm (process G) under solvent vapor produced from a Toluene:Heptane 5:1 volumetric mixture. G1, G2, G3, G4, show in situ GISAXS measurement data. The in situ measurement was done with help from Dr. Kevin Yager.

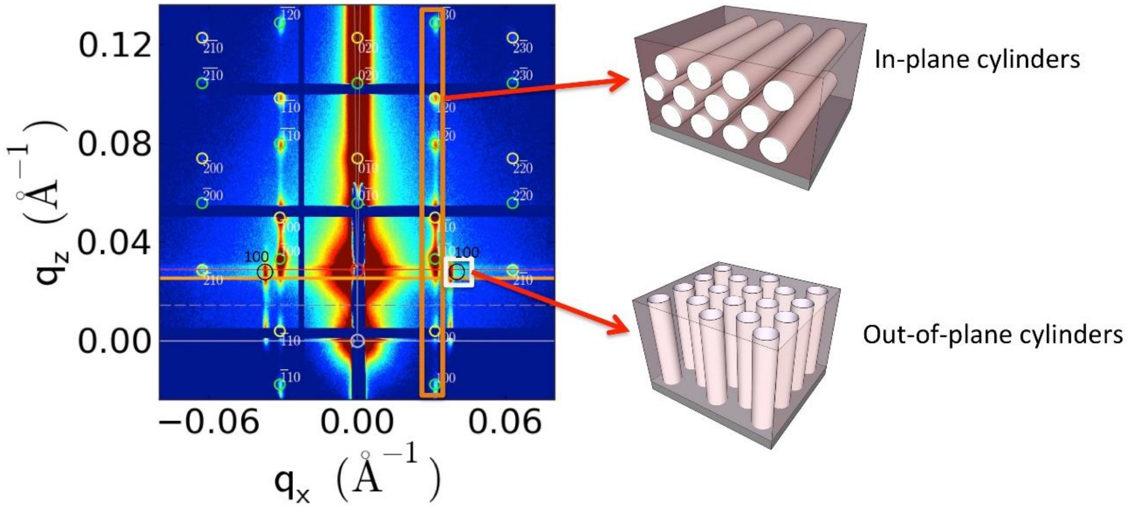

Figure 4.12. GISAXS of a solvent-annealed SD16 PS-PDMS block copolymer film with as-cast thickness 241 nm. Two groups of scattering peaks coexisted in the GISAXS data, corresponding to in-plane cylinders and out-of-plane cylinders, respectively. The in situ measurement was done with help from Dr. Kevin Yager.

4.7 Conclusion

in situ GISAXS has provided real-time observations of the progress of solvent vapor annealing in a high interaction parameter PS-*b*-PDMS block copolymer film with period ~18 nm, including characterization of the orientation and period of the microdomains. The 16 kg/mol PS-PDMS became disordered at a swelling ratio of SR_c=1.9 under the vapor of a toluene:heptane 5:1 volumetric mixture. Cylindrical microdomains formed during microphase separation at lower swelling ratios. The preference for PDMS to be present at the interfaces promoted in-plane cylinder orientation, whereas solvent gradients promoted perpendicular orientation. This led to the prevalence of in-plane cylinders for thinner films, and perpendicular cylinders for thicker films which reoriented in-plane during annealing. As found for other BCPs, the rate of swelling and deswelling influenced the structural orientation, deformation, and even reorganization. The swelled film formed close-packed cylinder arrays, but drying led to a decrease in correlation length and a collapse in the out-of-plane direction, so the close-packed array of in-plane cylinders became distorted. The amount of distortion of the in-plane cylinder array was greater for slower drying, and the angle between layers of cylinders reached 48˚ for the slowest drying process used here, compared to 60˚ in an ideal closepacked array. These results illustrate the multiple kinetic and thermodynamic factors which influence the final morphology, which is essential to the use of high-χ BCPs in sub-10nm nanolithography and other applications where control of microdomain morphology and orientation is required.

References

(1) Bai, W.; Yager, K. G.; Ross, C. A. In Situ Characterization of the Self-Assembly of a Polystyrene–Polydimethylsiloxane Block Copolymer during Solvent Vapor Annealing. *Macromolecules* **2015**, *48* (23), acs.macromol.5b02174.

(2) Ross, C. A.; Berggren, K. K.; Cheng, J. Y.; Jung, Y. S.; Chang, J.-B. Three-Dimensional Nanofabrication by Block Copolymer Self-Assembly. *Adv. Mater.* **2014**, *26* (25), 4386–4396.

(3) Darling, S. B. Block Copolymers for Photovoltaics. *Energy Environ. Sci.* **2009**, *2* (12), 1266.

(4) Phillip, W. A.; O'Neill, B.; Rodwogin, M.; Hillmyer, M. A.; Cussler, E. L. Self-Assembled Block Copolymer Thin Films as Water Filtration Membranes. *ACS Appl. Mater. Interfaces* **2010**, *2* (3), 847–853.

(5) Asquith, B. M.; Meier-Haack, J.; Vogel, C.; Butwilowski, W.; Ladewig, B. P. Side-Chain Sulfonated Copolymer Cation Exchange Membranes for Electro-Driven Desalination Applications. *Desalination* **2013**, *324*, 93–98.

(6) She, M.-S.; Lo, T.-Y.; Ho, R.-M. Controlled Ordering of Block Copolymer Gyroid Thin Films by Solvent Annealing. *Macromolecules* **2014**, *47* (1), 175–182.

(7) Campbell, I. P.; He, C.; Stoykovich, M. P. Topologically Distinct Lamellar Block Copolymer Morphologies Formed by Solvent and Thermal Annealing. *ACS Macro Lett.* **2013**, *2* (10), 918–923.

(8) Gotrik, K. W.; Hannon, A. F.; Son, J. G.; Keller, B.; Alexander-Katz, A.; Ross, C. A. Morphology Control in Block Copolymer Films Using Mixed Solvent Vapors. *ACS Nano* **2012**, *6* (9), 8052–8059.

(9) Bai, W.; Hannon, A. F.; Gotrik, K. W.; Choi, H. K.; Aissou, K.; Liontos, G.; Ntetsikas, K.; Alexander-Katz, A.; Avgeropoulos, A.; Ross, C. A. Thin Film Morphologies of Bulk-Gyroid Polystyrene- Block -Polydimethylsiloxane under Solvent Vapor Annealing. *Macromolecules* **2014**, *47* (17), 6000–6008.

(10) Kim, T. H.; Hwang, J.; Hwang, W. S.; Huh, J.; Kim, H.-C.; Kim, S. H.; Hong, J. M.; Thomas, E. L.; Park, C. Hierarchical Ordering of Block Copolymer Nanostructures by Solvent Annealing Combined with Controlled Dewetting. *Adv. Mater.* **2008**, *20* (3), 522–527.

(11) Gotrik, K. W.; Ross, C. A. Solvothermal Annealing of Block Copolymer Thin Films. *Nano Lett.* **2013**, *13* (11), 5117–5122.

(12) Jin, C.; Murphy, J. N.; Harris, K. D.; Buriak, J. M. Deconvoluting the Mechanism of Microwave Annealing of Block Copolymer Thin Films. *ACS Nano* **2014**, *8* (4), 3979–3991.

(13) Zhang, X.; Harris, K. D.; Wu, N. L. Y.; Murphy, J. N.; Buriak, J. M. Fast Assembly of Ordered Block Copolymer Nanostructures through Microwave Annealing. *ACS Nano* **2010**, *4* (11), 7021–7029.

(14) Borah, D.; Senthamaraikannan, R.; Rasappa, S.; Kosmala, B.; Holmes, J. D.; Morris, M. A. Swift Nanopattern Formation of PS-B-PMMA and PS-B-PDMS Block Copolymer Films Using a Microwave Assisted Technique. *ACS Nano* **2013**, *7* (8), 6583–6596.

(15) Park, W. I.; Kim, J. M.; Jeong, J. W.; Jung, Y. S. Deep-Nanoscale Pattern Engineering by Immersion-Induced Self-Assembly. *ACS Nano* **2014**, *8* (10), 10009–10018.

(16) Qiang, Z.; Zhang, Y.; Groff, J. A.; Cavicchi, K. A.; Vogt, B. D. A Generalized Method for Alignment of Block Copolymer Films: Solvent Vapor Annealing with Soft Shear. *Soft Matter* **2014**, *10* (32), 6068–6076.

(17) Yager, K. G.; Fredin, N. J.; Zhang, X.; Berry, B. C.; Karim, A.; Jones, R. L. Evolution of Block-Copolymer Order through a Moving Thermal Zone. *Soft Matter* **2009**, *6* (1), 92–99.

(18) Berry, B. C.; Bosse, A. W.; Douglas, J. F.; Jones, R. L.; Karim, A. Orientational Order in Block Copolymer Films Zone Annealed below the Order--Disorder Transition Temperature. *Nano Lett.* **2007**, *7* (9), 2789–2794.

(19) Hannon, A. F.; Ding, Y.; Bai, W.; Ross, C. A.; Alexander-Katz, A. Optimizing Topographical Templates for Directed Self-Assembly of Block Copolymers via Inverse Design Simulations. *Nano Lett.* **2014**, *14* (1), 318–325.

(20) Mickiewicz, R. A.; Yang, J. K. W.; Hannon, A. F.; Jung, Y.-S.; Alexander-Katz, A.; Berggren, K. K.; Ross, C. A. Enhancing the Potential of Block Copolymer Lithography with Polymer Self-Consistent Field Theory Simulations. *Macromolecules* **2010**, *43* (19), 8290–8295.

(21) Bates, C. M.; Seshimo, T.; Maher, M. J.; Durand, W. J.; Cushen, J. D.; Dean, L. M.; Blachut, G.; Ellison, C. J.; Willson, C. G. Polarity-Switching Top Coats Enable Orientation of Sub-10-Nm Block Copolymer Domains. *Science (80-.).* **2012**, *338*, 775–779.

(22) Verduzco, R.; Li, X.; Pesek, S. L.; Stein, G. E. Structure, Function, Self-Assembly, and Applications of Bottlebrush Copolymers. *Chem. Soc. Rev.* **2015**.

(23) Fenyves, R.; Schmutz, M.; Horner, I. J.; Bright, F. V; Rzayev, J. Aqueous Self-Assembly of Giant Bottlebrush Block Copolymer Surfactants as Shape-Tunable Building Blocks. *J. Am. Chem. Soc.* **2014**, *136* (21), 7762–7770.

(24) Hong, S. W.; Gu, W.; Huh, J.; Sveinbjornsson, B. R.; Jeong, G.; Grubbs, R. H.; Russell, T. P. On the Self-Assembly of Brush Block Copolymers in Thin Films. *ACS Nano* **2013**, *7* (11), 9684–9692.

(25) Olszowka, V.; Hund, M.; Kuntermann, V.; Scherdel, S.; Tsarkova, L.; Böker, A. Electric Field Alignment of a Block Copolymer Nanopattern: Direct Observation of the Microscopic Mechanism. *ACS Nano* **2009**, *3* (5), 1091–1096.

(26) Jeong, J. W.; Park, W. I.; Kim, M.; Ross, C. A.; Jung, Y. S. Highly Tunable Self-Assembled Nanostructures from a poly(2-Vinylpyridine-B-Dimethylsiloxane) Block Copolymer. *Nano Lett.* **2011**, *11*, 4095–4101.

(27) Park, W. I.; Kim, K.; Jang, H.-I.; Jeong, J. W.; Kim, J. M.; Choi, J.; Park, J. H.; Jung, Y. S. Directed Self-Assembly with Sub-100 Degrees Celsius Processing Temperature, Sub-10 Nanometer Resolution, and Sub-1 Minute Assembly Time. *Small* **2012**, *8* (24), 3762–3768.

(28) Zhang, J.; Posselt, D.; Smilgies, D.-M.; Perlich, J.; Kyriakos, K.; Jaksch, S.; Papadakis, C. M. Lamellar Diblock Copolymer Thin Films during Solvent Vapor Annealing Studied by GISAXS: Different Behavior of Parallel and Perpendicular Lamellae. *Macromolecules* **2014**, *47* (16), 5711–5718.

(29) Onses, M. S.; Song, C.; Williamson, L.; Sutanto, E.; Ferreira, P. M.; Alleyne, A. G.; Nealey, P. F.; Ahn, H.; Rogers, J. A. Hierarchical Patterns of Three-Dimensional Block-Copolymer Films Formed by Electrohydrodynamic Jet Printing and Self-Assembly. *Nat. Nanotechnol.* **2013**, *8* (9), 667–675.

(30) Kao, J.; Thorkelsson, K.; Bai, P.; Zhang, Z.; Sun, C.; Xu, T. Rapid Fabrication of Hierarchically Structured Supramolecular Nanocomposite Thin Films in One Minute. *Nat. Commun.* **2014**, *5*, 4053.

(31) Sinturel, C.; Vayer, M.; Morris, M.; Hillmyer, M. A. Solvent Vapor Annealing of Block Polymer Thin Films. *Macromolecules* **2013**, *46* (14), 5399–5415.

(32) Chremos, A.; Nikoubashman, A.; Panagiotopoulos, A. Z. Flory-Huggins Parameter χ, from Binary Mixtures of Lennard-Jones Particles to Block Copolymer Melts. *J. Chem. Phys.* **2014**, *140* (5), 054909.

(33) Nagarajan, R.; Ganesh, K. Block Copolymer Self-Assembly in Selective Solvents: Theory of Solubilization in Spherical Micelles. *Macromolecules* **1989**, *22* (11), 4312–4325.

(34) Gowd, E. B.; Böhme, M.; Stamm, M. In Situ GISAXS Study on Solvent Vapour Induced Orientation Switching in PS- B -P4VP Block Copolymer Thin Films. *IOP Conf. Ser. Mater. Sci. Eng.* **2010**, *14* (1), 012015.

(35) Gu, X.; Gunkel, I.; Hexemer, A.; Gu, W.; Russell, T. P. An in Situ Grazing Incidence X-Ray Scattering Study of Block Copolymer Thin Films during Solvent Vapor Annealing. *Adv. Mater.* **2014**, *26* (2), 273–281.

(36) Di, Z.; Posselt, D.; Smilgies, D.-M.; Papadakis, C. M. Structural Rearrangements in a Lamellar Diblock Copolymer Thin Film during Treatment with Saturated Solvent Vapor. *Macromolecules* **2010**, *43*, 418–427.

(37) Cui, G.; Fujikawa, M.; Nagano, S.; Shimokita, K.; Miyazaki, T.; Sakurai, S.; Yamamoto, K. Macroscopic Alignment of Cylinders via Directional Coalescence of Spheres along Annealing Solvent Permeation Directions in Block Copolymer Thick Films. *Macromolecules* **2014**, *47* (17), 5989–5999.

(38) Phillip, W. a; Hillmyer, M. a; Cussler, E. L. Cylinder Orientation Mechanism in Block Copolymer Thin Films Upon Solvent Evaporation. *Macromolecules* **2010**, *43*, 7763–7770.

(39) Paradiso, S. P.; Delaney, K. T.; García-Cervera, C. J.; Ceniceros, H. D.; Fredrickson, G. H. Block Copolymer Self Assembly during Rapid Solvent Evaporation: Insights into Cylinder Growth and Stability. *ACS Macro Lett.* **2014**, *3* (1), 16–20.

(40) Park, S.; Kim, B.; Xu, J.; Hofmann, T.; Ocko, B. M.; Russell, T. P. Lateral Ordering of Cylindrical Microdomains Under Solvent Vapor. *Macromolecules* **2009**, *42* (4), 1278–1284.

(41) Paik, M. Y.; Bosworth, J. K.; Smilges, D.-M.; Schwartz, E. L.; Andre, X.; Ober, C. K. Reversible Morphology Control in Block Copolymer Films via Solvent Vapor Processing: An In Situ GISAXS Study. *Macromolecules* **2010**, *43*, 4253–4260.

(42) Kim, S. H.; Misner, M. J.; Russell, T. P. Controlling Orientation and Order in Block Copolymer Thin Films. *Adv. Mater.* **2008**, *20* (24), 4851–4856.

(43) Park, S.; Wang, J.-Y.; Kim, B.; Chen, W.; Russell, T. P. Solvent-Induced Transition from Micelles in Solution to Cylindrical Microdomains in Diblock Copolymer Thin Films. *Macromolecules* **2007**, *40* (25), 9059–9063.

(44) Papadakis, C. M.; Di, Z.; Posselt, D.; Smilgies, D. M. Structural Instabilities in Lamellar Diblock Copolymer Thin Films during Solvent Vapor Uptake. *Langmuir* **2008**, *24* (24), 13815–13818.

(45) Kim, S. H.; Misner, M. J.; Xu, T.; Kimura, M.; Russell, T. P. Highly Oriented and Ordered Arrays from Block Copolymers via Solvent Evaporation. *Adv. Mater.* **2004**, *16* (3), 226–231.

(46) Cavicchi, K. A.; Berthiaume, K. J.; Russell, T. P. Solvent Annealing Thin Films of Poly(isoprene-B-Lactide). *Polymer (Guildf).* **2005**, *46*, 11635–11639.

(47) Cavicchi, K. A.; Russell, T. P. Solvent Annealed Thin Films of Asymmetric Polyisoprene−Polylactide Diblock Copolymers. *Macromolecules* **2007**, *40* (4), 1181–1186.

(48) Kim, S. H.; Misner, M. J.; Yang, L.; Gang, O.; Ocko, B. M.; Russell, T. P. Salt Complexation in Block Copolymer Thin Films. *Macromolecules* **2006**, *39* (24), 8473–8479.

(49) Marques, D. S.; Dorin, R. M.; Wiesner, U.; Smilgies, D.-M.; Behzad, A. R.; Vainio, U.; Peinemann, K.-V.; Nunes, S. P. Time-Resolved GISAXS and Cryo-Microscopy Characterization of Block Copolymer Membrane Formation. *Polymer (Guildf).* **2014**, *55* (6), 1327–1332.

(50) Kim, E.; Kim, W.; Lee, K. H.; Ross, C. A.; Son, J. G. A Top Coat with Solvent Annealing Enables Perpendicular Orientation of Sub-10 Nm Microdomains in Si-Containing Block Copolymer Thin Films. *Adv. Funct. Mater.* **2014**, 6981–6988.

(51) Cochran, E. W.; Morse, D. C.; Bates, F. S. Design of ABC Triblock Copolymers near the ODT with the Random Phase Approximation. *Macromolecules* **2003**, *36* (3), 782–792.

(52) Kennemur, J. G.; Yao, L.; Bates, F. S.; Hillmyer, M. A. Sub-5 Nm Domains in Ordered Poly(cyclohexylethylene)- Block -Poly(methyl Methacrylate) Block Polymers for Lithography.

Macromolecules **2014**, *47* (4), 1411–1418.

(53) Hannon, A. F.; Bai, W.; Alexander-Katz, A.; Ross, C. A. Simulation Methods for Solvent Vapor Annealing of Block Copolymer Thin Films. *Soft Matter* **2015**.

(54) Lodge, T. P.; Hanley, K. J.; Pudil, B.; Alahapperuma, V. Phase Behavior of Block Copolymers in a Neutral Solvent. *Macromolecules* **2003**, *36* (3), 816–822.

(55) Lodge, T. P.; Pan, C.; Jin, X.; Liu, Z.; Zhao, J.; Maurer, W. W.; Bates, F. S. Failure of the Dilution Approximation in Block Copolymer Solutions. *J. Polym. Sci. Part B Polym. Phys.* **1995**, *33* (16), 2289–2293.

(56) Sinturel, C.; Bates, F. S.; Hillmyer, M. A. High χ − Low N Block Polymers : How Far Can We Go ? *ACS Macro Lett.* **2015**.

(57) Bates, F. S.; Fredrickson, G. H. Block Copolymers—Designer Soft Materials. *Phys. Today* **1999**, *52* (2), 32.

(58) Son, J. G.; Gotrik, K. W.; Ross, C. A. High-Aspect-Ratio Perpendicular Orientation of PS- B - PDMS Thin Films under Solvent Annealing. *ACS Macro Lett.* **2012**, *1* (11), 1279–1284.

(59) Gowd, E. B.; Koga, T.; Endoh, M. K.; Kumar, K.; Stamm, M. Pathways of Cylindrical Orientations in PS-B-P4VP Diblock Copolymer Thin Films upon Solvent Vapor Annealing. *Soft Matter* **2014**, *10* (39), 7753–7761.

(60) Harrison, C. Mechanisms of Ordering in Striped Patterns. *Science (80-.).* **2000**, *290* (5496), 1558–1560.

(61) Ruiz, R.; Bosworth, J.; Black, C. Effect of Structural Anisotropy on the Coarsening Kinetics of Diblock Copolymer Striped Patterns. *Phys. Rev. B* **2008**, *77* (5), 054204.

(62) Vega, D.; Harrison, C.; Angelescu, D.; Trawick, M.; Huse, D.; Chaikin, P.; Register, R. Ordering Mechanisms in Two-Dimensional Sphere-Forming Block Copolymers. *Phys. Rev. E* **2005**, *71* (6), 061803.

(63) Boyer, D.; Viñals, J. Domain Coarsening of Stripe Patterns close to Onset. *Phys. Rev. E* **2001**, *64* (5), 050101.

(64) Boyer, D. Numerical Study of Domain Coarsening in Anisotropic Stripe Patterns. *Phys. Rev. E* **2004**, *69* (6), 066111.

(65) Byeongdu Lee, †; Insun Park; Jinhwan Yoon; Soojin Park; Jehan Kim; Kwang-Woo Kim; Taihyun Chang, * and; Ree*, M. Structural Analysis of Block Copolymer Thin Films with Grazing Incidence Small-Angle X-Ray Scattering. *Macromolecules* **2005**, *38* (10), 4311–4323.

(66) Lazzari, R.; Leroy, F.; Renaud, G. Grazing-Incidence Small-Angle X-Ray Scattering from Dense Packing of Islands on Surfaces: Development of Distorted Wave Born Approximation and Correlation between Particle Sizes and Spacing. *Phys. Rev. B* **2007**, *76* (12), 125411.

(67) Renaud, G.; Lazzari, R.; Leroy, F. Probing Surface and Interface Morphology with Grazing Incidence Small Angle X-Ray Scattering. *Surf. Sci. Rep.* **2009**, *64* (8), 255–380.

(68) Lee, B.; Park, I.; Yoon, J.; Park, S.; Kim, J.; Kim, K.-W.; Chang, T.; Ree, M. Structural Analysis of Block Copolymer Thin Films with Grazing Incidence Small-Angle X-Ray Scattering. *Macromolecules* **2005**, *38* (10), 4311–4323.

(69) Toney, M. F.; Brennan, S. Observation of the Effect of Refraction on X Rays Diffracted in a Grazing-Incidence Asymmetric Bragg Geometry. *Phys. Rev. B* **1989**, *39* (11), 7963–7966.

(70) Lu, X.; Yager, K. G.; Johnston, D.; Black, C. T.; Ocko, B. M. Grazing-Incidence Transmission X-Ray Scattering: Surface Scattering in the Born Approximation. *J. Appl. Crystallogr.* **2013**, *46* (1), 165–172.

(71) Busch, P.; Rauscher, M.; Smilgies, D.-M.; Posselt, D.; Papadakis, C. M. Grazing-Incidence Small-Angle X-Ray Scattering from Thin Polymer Films with Lamellar Structures – the Scattering Cross Section in the Distorted-Wave Born Approximation. *J. Appl. Crystallogr.* **2006**, *39* (3), 433–442.

(72) Dag W. Breiby, Oliver Bunk, Jens W. Andreasen, Henrik T. Lemked, M. M. N. Simulating X-ray diffraction of textured films http://journals.iucr.org/j/issues/2008/02/00/ce5029/ (accessed Apr 23, 2015).

(73) Langford, J. I.; Wilson, A. J. C. Scherrer after Sixty Years: A Survey and Some New Results in the Determination of Crystallite Size. *J. Appl. Crystallogr.* **1978**, *11* (2), 102–113.

(74) Smilgies, D.-M. Scherrer Grain-Size Analysis Adapted to Grazing-Incidence Scattering with Area Detectors. *J. Appl. Crystallogr.* **2009**, *42* (Pt 6), 1030–1034.

(75) Page, K. A.; Kusoglu, A.; Stafford, C. M.; Kim, S.; Kline, R. J.; Weber, A. Z. Confinement-Driven Increase in Ionomer Thin-Film Modulus. *Nano Lett.* **2014**, *14* (5), 2299–2304.

(76) Johnston, D. E.; Yager, K. G.; Hlaing, H.; Lu, X.; Ocko, B. M.; Black, C. T. Nanostructured Surfaces Frustrate Polymer Semiconductor Molecular Orientation. *ACS Nano* **2014**, *8* (1), 243–249.

(77) Wauquier, J. P. *Petroleum Refining. Vol....*; Editions OPHRYS, 2000.

(78) Matsoukas, T. *Fundamentals of Chemical Engineering Thermodynamics: With Applications to Chemical Processes*; Prentice Hall, 2013.

Chapter 5: Templating Strategies to enable Orientation Control of BCP Microdomains

5.1 Abstract

In this chapter, we investigate mainly on the effect of high aspect ratio templates to enable perpendicular orientation of block copolymer microdomains, and briefly on combining effects between graphoepitaxy and electric fields as well as effects of multiple trenches on selective area control of BCP thin film self-assembly. Perpendicular orientation of lamellar microdomains in a lamellar-forming PS-PDMS was obtained within high aspect ratio gratings functionalized with a preferential sidewall brush. The experiments used polystyrene-block-polydimethylsiloxane with molecular weight 43 kg/mol within trenches made using interference lithography. The perpendicular alignment was obtained for both thermal and solvent annealing, using three different solvent vapors, for a range of film thicknesses and trench widths. A Pt layer at the base of the trenches avoided the formation of a wetting layer, giving perpendicular orientation at the substrate surface. The results are interpreted using self-consistent field theory simulation to map the energies of lamellae of different orientations as a function of the grating aspect ratio and the surface energies of the sidewalls and top and bottom surfaces. The model results agree with the experiment and provide a set of guidelines for obtaining perpendicular microdomains within topographic features. Orientation control of cylindrical microdomains in a cylinder-forming PS-PDMS self-assembly was enhanced using a combined directing effect of simultaneously applied graphoepitaxy and electric field. And selective area control of 3D self-assembled nanostructure was achieved by using multiple trenches with various dimension and arrangements. Part of this work was published in Ref. [1], [2].

5.2 Introduction

Perpendicular (vertical) orientation of block copolymer microdomains can be produced by several methods, including i) a neutral top coating and neutral substrate brush that minimize the interfacial energy difference between the blocks at the air and substrate interfaces respectively; [3–5] ii) a specifically designed molecular architecture [6–8] such as a brush or multi-arm BCP that can form microdomains oriented out-of-plane without modification of the underlying substrate, due to the entropic penalty associated with the packing of the side chains;[8] and iii) modifying the annealing process to use a solvent concentration gradient, [3,9] temperature gradient,[10,11] electric [12] or magnetic field[13] , chemoepitaxy and/or graphoepitaxy,[14] and electrospray deposition[15] to induce out-of-plane alignment of self-assembled microdomains. These methods have been used successfully in various BCP systems, but become more challenging as the blocks become more incompatible and the alignment method has to overcome a greater surface energy difference. In this article, perpendicular alignment of a high-χ lamellar BCP is demonstrated, not by minimizing the differences in surface energy of the blocks, but instead taking advantage of preferential wetting at the vertical sidewalls of high aspect-ratio templates. There have been examples of lamellar BCP microphase separation in high aspect ratio pores[16,17] but the effects of varying aspect ratio and surface chemistry have not been quantified.

5.3 Experimental Methods

A lamella-forming polystyrene-*block*-polydimethylsiloxane (PS-*b*-PDMS) with molecular weight $M_w = 43$ kg/mol, volume fraction $f_{PDMS} = 49\%$, PDI = 1.08, designated SD43, was used to demonstrate orientation control in high aspect-ratio gratings. The room-temperature χ of PS-*b*-PDMS is reported as 0.14 - 0.27[31], and its high etch selectivity and the etch resistance of the PDMS makes it useful in nanolithography. After annealing, the PS block is removed by an oxygen plasma which oxidizes the PDMS, making a stable silica-rich nanostructure.

Laser interference lithography was used to fabricate the high aspect-ratio gratings. An interference pattern between two coherent laser beams (wavelength 350 nm) produced a grating pattern with period of ~200 nm and above in resist over a large substrate area without the use of a photomask.[20] The exposed and developed grating pattern was transferred from the photoresist into an underlying thick anti-reflective coating (ARC) layer, making trenches with width and depth ≥100 nm. To obtain a preferential surface, a PDMS brush polymer was grafted on the sidewalls and the trench floor. The surface affinity of the trench floor was modified by coating the substrate with electron-beam evaporated Pt prior to making the ARC grating. The brush layer did not graft well to the Pt, which does not bond to the hydroxyl group of the brush.[21] This led to a surface that was considerably less attractive to PDMS than the brush-coated sidewall was. A process flow showing the fabrication method is described in the supplementary material.

5.3.1 High Aspect ratio Trench Fabrication

Anti-reflective coating (ARC) was first spin coated on a Si wafer and then baked on a hotplate at 175°C for 60 s to induce crosslinking. Then 20nm SiO_2 was deposited by electron beam evaporation. A 200 nm PFI 88 photoresist was spin coated on top of the SiO_2 layer and baked on a hotplate at 90°C for 60s. The sample was exposed by an interference pattern that was generated from 2-beam coherent laser for several minutes using a Lloyds Mirror system. A post-exposure development was used to produce the photoresist grating. Then CF$_4$ plasma etching transferred the photoresist pattern into the SiO$_2$ layer, and an O$_2$ plasma transferred the pattern into the ARC layer to make high aspect ratio trenches. A schematic is shown in figure 5.1.

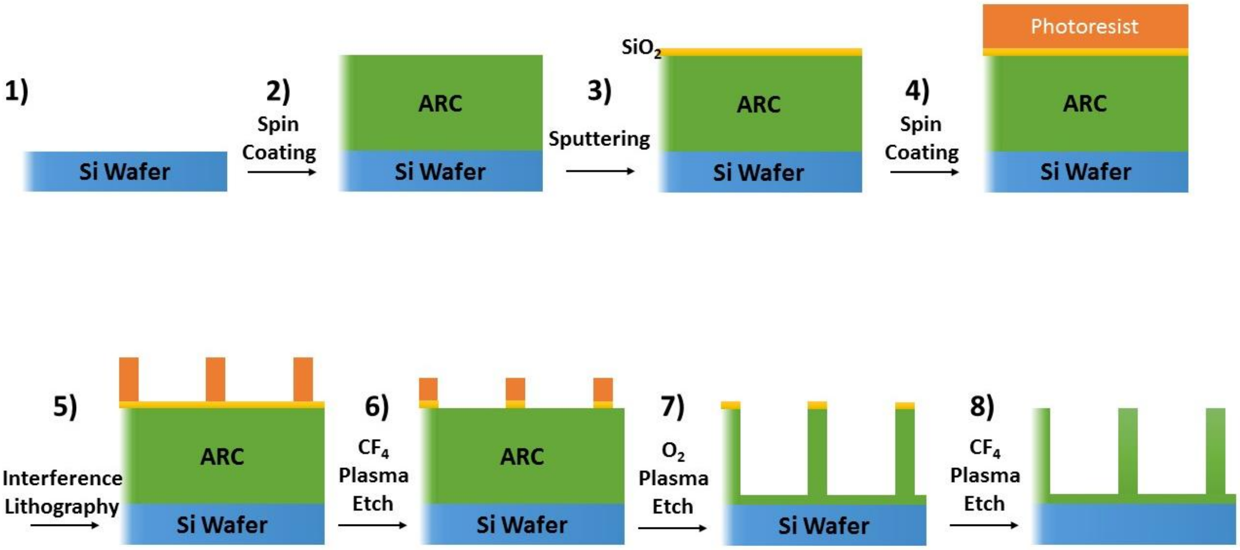

Figure 5.1. High Aspect-ratio Trenches Fabrication Process Flow. 1) Si wafer; 2) spin coat anti-reflective coating (ARC); 3) sputter SiO2; 4) spin coat photoresist; 5) Laser Interference lithography; 6) CF$_4$ plasma etch of SiO$_2$; 7) O$_2$ plasma etch of ARC; 8) CF$_4$ plasma etch of SiO$_2$.

5.3.2 Brush treatment and Block Copolymer solution preparation

The hydroxyl-terminated polydimethylsiloxane (0.8 kg mol^{-1}, PolymerSource, Inc) was dissolved 5 wt.% in toluene and then spin coated on high aspect ratio templates at a spin speed of 2000 rpm. Then the samples were baked in a vacuum oven for 16 hr at a pressure of 2600 Pa (20 Torr) and temperature of 170 ^{o}C. After baking, the samples were rinsed with toluene to remove unreacted brush and then dried using N$_2$ gas. 43 kg mol^{-1} PS-*b*-PDMS (PolymerSource, Inc. f_{PDMS} = 0.5) as 5 wt.% in toluene solution was spin coated onto the brush-treated templates at spin speed 3500 rpm.

5.3.3 Solvent Vapor Annealing

Solvent vapor annealing has been described in previous work.[22,23] Briefly, liquid toluene-heptane mixture, or cyclohexane, or acetone of 3 ml was placed in a glass annealing chamber of volume ~ 70 cm^3 with a lid. The sample was placed on a small stage above the liquid. The generated solvent vapor was absorbed by the polymer film and the degree of swelling (measured by a Filmetrics reflectometer) was tuned by altering the leakage of solvent vapor from the chamber. For three hour anneals there was remaining liquid solvent in the chamber, and the sample was deswelled within a few seconds by removing the lid of the chamber. For 24 hr anneals the solvent had fully evaporated so the condition corresponds to a slow deswelling.

5.3.4 Thermal Annealing

Samples were placed into a vacuum oven and annealed in 20 Torr at 150°C for 16 hr.

5.3.5 Reactive Ion Etching

To reveal the self-assembled nanostructure, a two-step reactive ion etching was applied. First, a 30 CF_4 and O_2 plasma with power 450 W and pressure 15 mTorr was performed to planarize the polymer film for 30s. Then, an O_2 plasma with power 90 W and pressure 6 mTorr was performed to selectively remove the PS block and partially oxidize the PDMS block into robust SiO_x.

5.3.6 Helium Ion Microscope

In this work, the cross section of some samples was imaged by helium ion microscope (HIM), which has higher resolution and greater depth of field than a typical scanning electron microscope (SEM). HIM is similar to SEM, but uses He^+ ions instead of electrons to image. Before imaging, the samples were coated with a 3-nm thin layer of Au-Pd alloy in order to make the surface conductive. During imaging, helium ions interact with the sample surface and generate secondary electrons, which were collected by the Everhardt-Thornley detector to provide image information. Due to the picometer wavelength of helium ions and high collimation of the beam, the diffraction limit and lens aberrations are negligible. However, for the polymer film, beam damage is possible if the exposure time is too long.

5.4 Results and Discussion

Interfacial interactions have a very important influence on the final equilibrium morphology of BCP self-assembly,[24,25] and form the basis of templating strategies.[26,27] In a high aspect-ratio template we consider three pairs of interfacial energies with respect to a lamellar-forming *A-B* diblock copolymer: γ_{Top}, γ_{Bot}, γ_{Side}, where γ is the interfacial energy and “Top”, “Bot”, and “Side” refer to the top (i.e. air surface), bottom and sidewall surface, respectively, as shown in figure 5.2a. The interfacial energy difference for each surface is defined as $\Delta\gamma = |\gamma_A - \gamma_B|$, i.e. a neutral surface has $\Delta\gamma = 0$ and a preferential surface has non-zero $\Delta\gamma$. The aspect ratio of the slab of BCP in the trench is defined as $R = t/w$ with t the thickness of the film and w the trench width. A perpendicular lamellar orientation is expected when the interaction energy with the sidewalls dominates, i.e. $\Delta\gamma_{Side}.t >> \Delta\gamma_{Top}.w$, $\Delta\gamma_{Bot}.w$, i.e. $\Delta\gamma_{Side} >> \Delta\gamma_{Top}/R$, $\Delta\gamma_{Bot}/R$. Therefore perpendicular self-assembled microdomains are promoted by large R and large $\Delta\gamma_{Side}$. In our experiment, we examine the effects of the surface energy of the grating walls (indicated in figure 5.2a) and the aspect ratio of the BCP in the trench. The fabricated trench depth was fixed at 450 nm, while the trench width varied from 150 nm to 500 nm, exemplified in Figs. 5.2b and 4b. To vary $\Delta\gamma_{Bot}$, a 20 nm thick platinum layer was inserted underneath the ARC, shown in Fig. 5.3. The surface tension of PS and PDMS on platinum has been reported as 33 mJ m^{-2} and 25 mJ m^{-2} respectively.[28,29] Therefore the platinum surface has a slight preference to the PDMS block, but this is much smaller than the surface affinity of a PDMS-grafted surface.

We first describe the effect of aspect ratio R when the surface energy of the sidewall and bottom surfaces are equal. The ARC sidewalls and base of the trenches were made preferential to PDMS by grafting a hydroxy-terminated PDMS layer onto the template. The SD43 film thickness was varied from 100 nm to 550 nm. The samples of Figs. 5.2 and 5.3 were processed by solvent vapor annealing at room temperature,[23] and the depth of the trenches was 550 nm. Previous studies reported that the choice of solvent composition and partial pressure, the swelling rate and solvent removal rate affect the final morphology and the microdomain orientation.[30,31] We examined three different solvents: a selective solvent mixture (toluene: heptane vapor from a 3:1 volumetric ratio, in which heptane preferentially swells PDMS and toluene is weakly preferential), a selective solvent (cyclohexane) which preferentially swells PDMS, and a selective solvent (acetone) which preferentially swells PS (Table S1). For each solvent the final morphology depended primarily on the aspect ratio and surface chemistry, except that cyclohexane led to a morphological transition which will be described later (Fig. 5.2f).

TABLE S1. Solubility Parameters of the Solvents and Polymers Investigated.

Material	Solubility Parameter ($MPa^{1/2}$)
PDMS	15.5
PS	18.5
Heptane	15.3
Toluene	18.3
Acetone	19.7
Cyclohexane	16.8

The relevant Hildebrand solubility parameters (δ) are summarized in Table S1.[32] The compatibility of nonpolar materials can be roughly estimated by comparing $|\delta_{polymer} - \delta_{solvent}|$, where a lower value represents more miscibility.

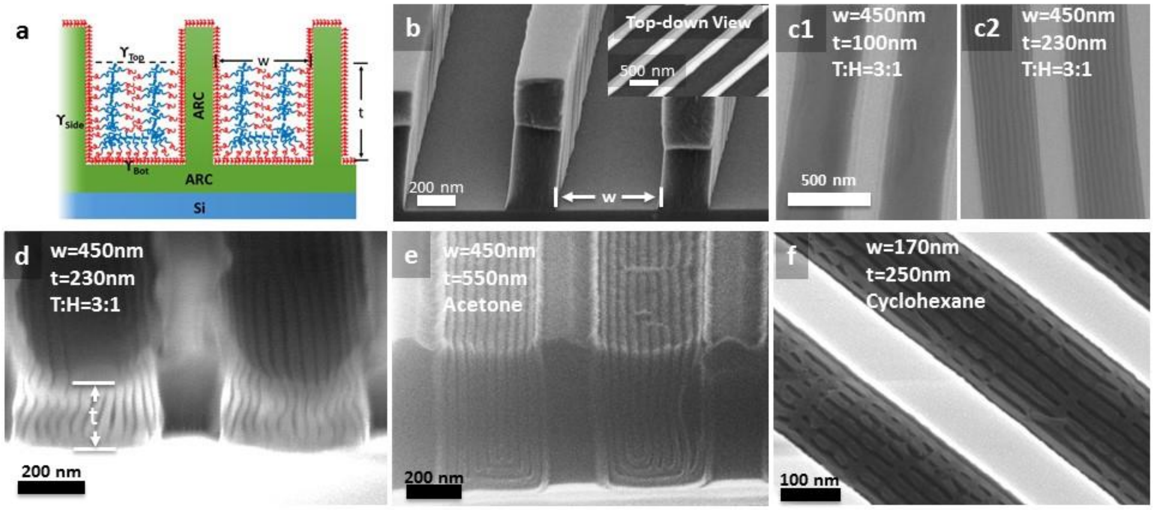

Figure 5.2. PDMS-brushed templates, solvent anneal. (a). A schematic of lamella-forming block copolymer film in a high aspect-ratio grating. γ_{Side}, γ_{Top}, γ_{Bot} are the interfacial energy at the sidewall, bottom and top surface. w is the width of the trench, t is the thickness of the film. Blue indicates the PDMS, red the PS blocks; (b). 75^{o} SEM tilted view of a cross-section of a high-aspect ratio grating; inset shows top-down SEM of high-aspect ratio gratings; (c1). Top-down SEM view of a 100nm thick SD43 film showing in-plane lamellae after reactive ion etching (RIE). (c2). Top-down SEM view of a 230nm thick SD43 film showing out-of-plane lamellae after RIE; (d, e, f). Cross-section SEM of self-assembled perpendicular SD43 lamellae inside high aspect-ratio trench; 75^{o} SEM tilted view. The lamella-forming SD43 PS-PDMS films were spin-cast with thickness (d)

230nm; (e) 550nm; (f) 250nm; (d), annealed under solvent vapor produced from toluene: heptane 3:1 volumetric mixture for 3 hr, showing a meniscus; (e), annealed under acetone solvent vapor for 3 hr. (f), annealed under cyclohexane solvent vapor for 3 hr; b-e, Trench width 450nm, depth 550nm. f, Trench width 170nm, depth 550nm. T: Toluene; H: Heptane.

In a trench width of 450 nm, a 100 nm thick BCP film formed in-plane (horizontal) lamellae (Fig. 5.2c1) in a toluene:heptane anneal. Perpendicular lamellae were observed in a 230 nm thick film (Fig. 5.3 and 5.2d). We believe that the perpendicular orientation in the 230 nm film, where the aspect ratio < 1, is aided by the swelling of the film and by solvent concentration gradients during the anneal. A 500 nm thick film in a 450 nm wide trench (Fig. 5.4d) formed lamellae with straighter interfaces and with a PDMS wetting layer at the bottom surface, due to the PDMS-brush. A 550 nm thick film in a 450 nm trench (Fig. 5.2e) in an acetone anneal produced highly oriented perpendicular lamellae parallel to the sidewalls. In general, acetone anneals produced more wetting and interconnections between lamellae at the base of the trench than toluene:heptane anneals. The top air/film interface always favored a PDMS wetting layer, due to its low surface energy,[23] but in these images this top in-plane layer was removed by the reactive ion etch and is usually not visible. Regions of an in-plane lamella at the top are visible in Fig. 5.2d and 4c.

In comparison, when the trench width was narrowed down to 170 nm and the sample was processed by cyclohexane solvent vapor annealing, the effective increase in PDMS volume fraction led to a transition to a perforated lamella structure standing perpendicular to the substrate, in which the PDMS lamellae are connected by bridges through the PS (Fig. 5.2f).

A high aspect ratio trench with PDMS-preferential sidewalls therefore favors perpendicular lamellae, except at the top and bottom surfaces. To avoid a wetting layer at the bottom surface, a thin layer of Pt was deposited on the substrate prior to forming the grating (Fig. 5.3a, schematic of sample; Fig. 5.4b, tilted SEM image). The PDMS brush is not expected to graft to the Pt surface, in contrast to its grafting to the ARC sidewall during the brush treatment process, making the sidewall surface more preferential to the PDMS block than bottom surface. The importance of the topography and surface chemistry can be seen in a 2 μm-thick SD43 film shown in cross-section in figure 5.3b. Excellent perpendicular alignment of the lamellae was achieved within the trench, but above the patterned area the polymer self-assembled into its expected lamellar structure parallel to the substrate. The figure clearly shows the ability of the polymer to switch between two orthogonal orientations to satisfy the imposed boundary conditions, and shows that the perpendicular structure is not a metastable state due to directional evaporation of the solvent.

Fig. 5.3c shows a similar sample with 400 nm thick SD43 in which several layers of parallel lamellae are present at the air surface. Fig. 5.3d shows the same film in which the top parallel lamellae were removed by applying high power (450 W) CF_4 and O_2 plasma for 50 s, planarizing the structure down to t_r = 150 nm thickness, and demonstrating how smaller aspect ratio perpendicular lamellae can be produced. In Fig. 5.3b-d the lamellae form perpendicular to the Pt producing little or no PDMS wetting at the bottom. Fig. 5.4a and 5.4c show further examples of vertical lamellae in trenches with a Pt base. In Fig. 5.4a the vertical orientation was produced in a film 150 nm thick in 300 nm wide trenches. This sample was not processed with the high power etch to better preserve the top layer morphology, showing a tilting of the PDMS lamellae at the top surface to form the thin wetting layer.

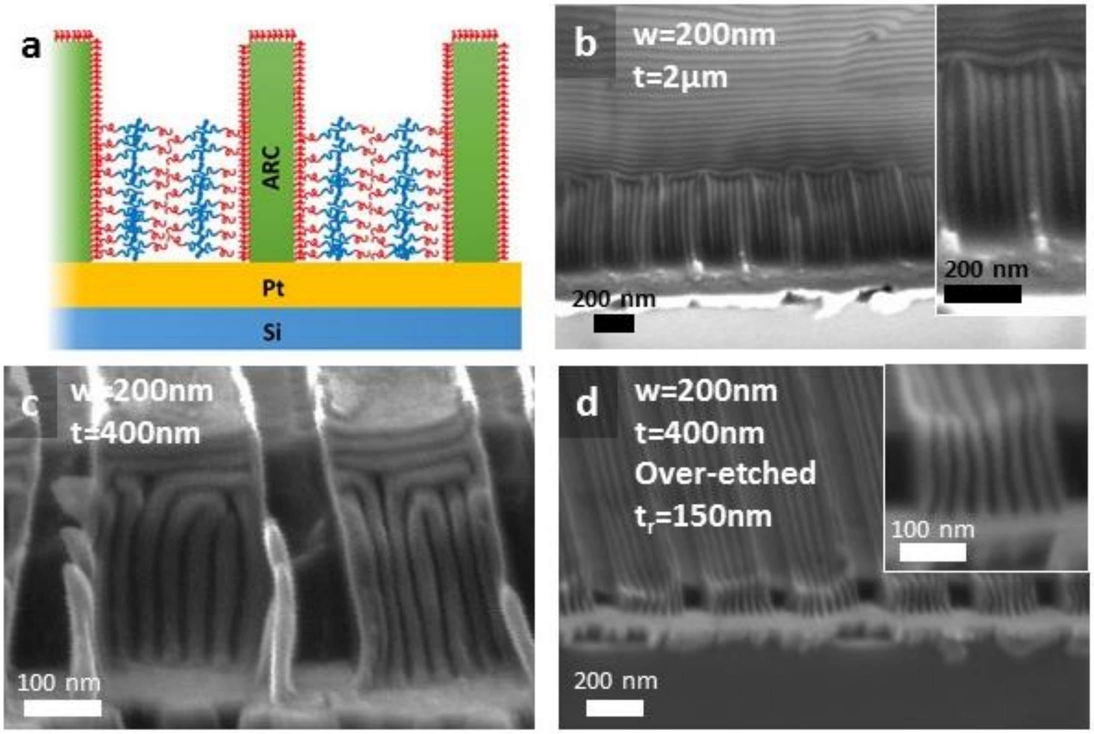

Figure 5.3. Templates with Pt base, solvent anneal. Lamella-forming block copolymer film in high aspect-ratio gratings with sidewall made of ARC and bottom surface made of Pt. Sidewall surface is attractive to PDMS; Bottom surface is more neutral. (a). Schematic of sample; (b). 85° tilted-view cross-section Helium Ion Microscope (HIM) image of 2μm thick lamella-forming PS-PDMS (SD43) film on the high aspect-ratio gratings after anneal; inset: magnified view; (c). 75° tilted-view cross-section HIM. 400 nm thick SD43 film in high aspect ratio trenches after anneal; (d). 75° tilted-view cross-section SEM. The same 400 nm thick annealed SD43 film was processed by a 30s, 450W

CF_4/O_2 plasma etch, planarizing the structure down to $t_r = 150$ nm thickness. (b-d) were annealed under solvent vapor produced from a toluene: heptane 3:1 volumetric mixture for 5hr. *w*: width of the trench. *t*: thickness of SD43 film inside trench.

Fig. 5.5 shows that thermal annealing can also produce perpendicular lamellae in high aspect-ratio gratings. Samples with a SD43 thickness of 445 nm (Fig. 5.5a) and 311 nm (Fig. 5.5b) in 350 nm deep, 200 nm wide gratings with a Pt base were annealed at 150 ^{o}C for 24 hr in vacuum. In Fig. 5.5a, lamellae within the gratings were aligned along the grating, but the film just above the grating showed a transition to in plane orientation. Thinner films (Fig. 5.5b) were well aligned through the thickness, after removing the PDMS layer at the air interface. Figs. 5.5c and 5.5d show thermal annealing for a 450 nm wide trench with both sidewall and bottom layer made of ARC. Perpendicular lamellae were found for SD43 thickness of 227 nm and 394 nm, but a thin PDMS wetting layer at the bottom connected the lamellae, due to the grafted PDMS brush at the base.

The ARC sidewalls in Figs. 5.5a,b,c showed a slight taper such that the trench width was smaller at the base than the top. This led to formation of an extra lamella in nearly all the trenches, i.e. one lamella branched into two, indicated in Fig. 5.5a.

To explain the experimental results, a self-consistent field theoretic (SCFT) simulation was employed to study the equilibrium morphology of a diblock copolymer inside a trench confinement as a function of aspect ratio and surface affinity. A detailed description of the simulation method is given in the supplementary material. Here we consider a 2D rectangular volume of width $L_x = 30R_g$ (where R_g is the radius of gyration) and a varying height L_z. This represents a cross-sectional view of the trench-confined BCP self-assembly. The geometry of the trench is varied to consider a range of aspect ratios $R \equiv L_z/L_x \epsilon$ [0.8, 1.0, 1.2, 1.4, 1.6, 1.8]. The four boundaries of the computational cell are made attractive to block *A*. The top surface has an independent strength of attraction w_{Top} to simulate the low surface energy of PDMS,[23] while the three remaining surfaces have equal affinity w_{Surr} to *A* simulating a brush layer coating on the trench sidewalls and substrate. Hence, by modulating the strength of attraction in the model, we modify the interfacial interactions at the boundaries. The volume fraction *f* of the block copolymer is set to 0.5, and the degree of incompatibility (= χN, where N is degree of polymerization) to 14 in order to represent the lamella-forming PS-PDMS block. In this 2D simulation, the effect of aspect ratio, free top surface affinity, and surrounding walls affinities on the alignment of the lamellar structure are investigated.

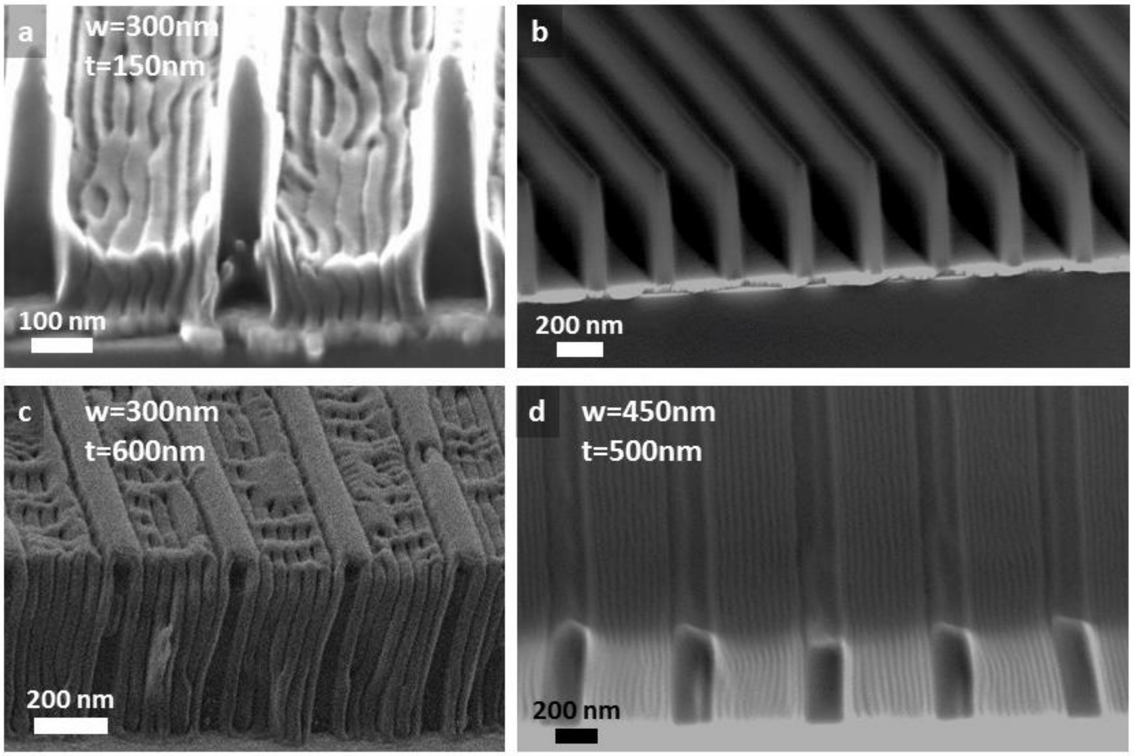

Figure 5.4. (a) SD43 film with thickness 150 nm in 300 nm wide trenches, processed without high power CF_4 etch to better preserve the morphology of the top layer. Due to the capillary forces, a meniscus formed at the top surface of the SD43 film, which led to the bending of the perpendicular lamellae at the top surface; (b) tilted SEM view of high-aspect ratio trenches with Pt layer underneath. Trench width 300 nm, trench depth 550 nm; (c) SD43 film with thickness 600 nm; When the SD43 filled the trench, the meniscus effect was avoided. (d) SD43 film with thickness 500 nm. (a), (c), (d) were annealed under the solvent vapor generated from Toluene: Heptane 3:1 volumetric mixture for 3 h. All sidewalls are PDMS-brush treated. (a), (c) with Pt base layer; (d) without Pt base layer. A PDMS wetting layer at the base was observed at a few locations in (c). (d) achieved excellent perpendicular-oriented lamellae throughout the film, assisted by the solvent concentration gradient during solvent annealing and the high aspect ratio of the SD43 film in the trench, but still shows a PDMS layer at the base of each trench in contrast with c).

To compare the relative stabilities of perpendicular and in plane orientations, the analysis is first performed by seeding a vertical or a horizontal self-assembled lamellar structure to the SCFT simulation. The structure is allowed to relax by evolving the fields at varying surface attraction strengths, w_{Top} and w_{Surr}. This led to parallel lamellae with a PDMS wetting layer at each surface. The free energies of both vertical F_V and horizontal F_H aligned lamellar structures are calculated following eq. S1 of Ref[1]. Figure 5.6 shows the corresponding free energy difference F_V-F_H calculated for R values 0.8, 1.0 and 1.2 (the free energy difference for larger R values is shown in ref [1]). For R less than unity ($R = 0.8$) the free energy surface is predominantly positive. The horizontal lamellar structure is stable (white markers) when the surface attraction field is small and positive, $w_{Top} \geq 2$. Vertical lamellae (black markers) can be attained with small w_{Top} and wall attraction $w_{Surr} > w_{Top}$. Increasing both w_{Top} and w_{Surr} favors the horizontal lamellae. The behavior is switched when $R \geq 1$; the free energy difference is predominantly negative. The vertical structure becomes stable for smaller w_{Surr} while larger w_{Top} is needed to realize a horizontal structure. The vertical structure is favored when increasing both w_{Top} and w_{Surr}. Increasing R raises the free energy difference between both morphologies, giving more stability to the vertical morphology.

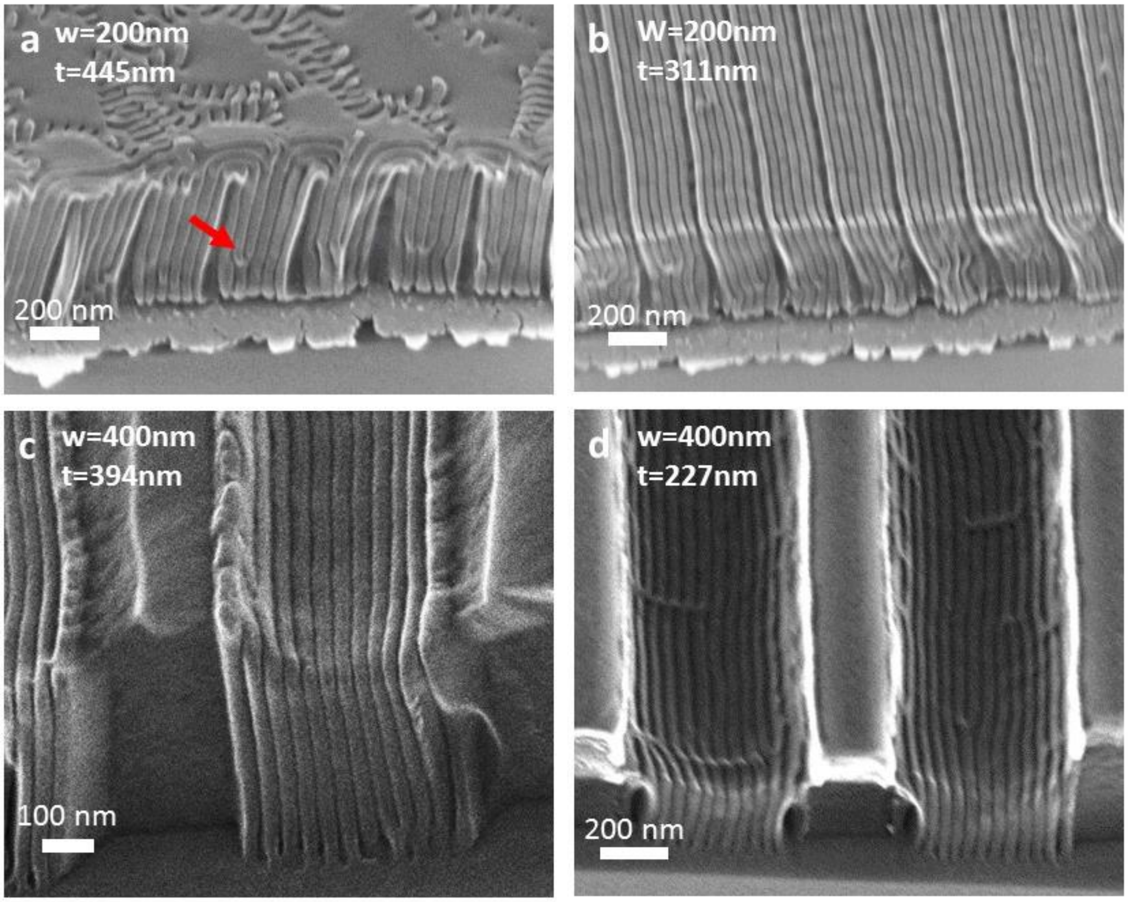

Figure 5.5. Thermal annealing. 70° tilted helium ion microscope of self-assembled lamella of PS-PDMS. All samples were annealed at 150 °C for 24 hr. a, b, sidewall is ARC, the bottom surface is platinum, ARC grating depth 350 nm, trench width 250 nm; Arrow: one lamella branched into two, a typical defect in perpendicular self-assembled

lamellae. c, d. both sidewall and bottom surface are ARC, depth 450 nm, trench width 400 nm; SD43 thickness: a. 445 nm; b. 311 nm; c. 394 nm; d. 227 nm.

While the free energy analysis aligns with the experimental work, there are regions in the parameter space where the free energy differences are quite small in magnitude, ~ 0.01 nVk_bT where V is the volume of the block copolymer and n the number of molecules per unit volume. These regions are primarily when w_{Top} and w_{Surr} are comparable and R is closer to unity. These almost degenerate situations would produce structures having mixed morphologies. It is insightful to observe the resulting polymer structure under these conditions.

To allow for the formation of kinetically trapped morphologies, SCFT simulations were also conducted under the surface conditions previously investigated in Fig. 5.6, but instead, the structure was self consistently evolved from random fields, simulating polymer phase separation from the disordered state. The final structures obtained from the simulation can be divided into three main categories: Horizontal lamellae, Mixed lamellae, and Vertical lamellae (representative results for R = 1.4 are shown in Fig. 5.7b). A 4D plot summarizes the results of the SCFT simulations in Fig. 5.7a. The scale of the x and y axes are the surface field strengths for the walls w_{Surr} and top surface w_{Top}, respectively. For each pair of (w_{Surr}, w_{Top}), a set of six color bars represents results for the six values of R. The color indicates Horizontal (white), Mixed (gray), or Vertical (black) lamellar orientations. To objectively classify each structure, a vertical and a horizontal defect-free structure were employed as references for every R, and the characteristics of the self-assembly are then calculated using a correlation function between the reference and the model result. A polymer structure is considered vertical or horizontal when it has a correlation function higher than 0.7 with the corresponding reference structure (the density profiles of the SCFT simulations are provided in the supplementary information). The final structures agree very well with the free energy map in Fig. 5.6, except for the presence of mixed orientations which were not considered in Fig. 5.6 and which, once formed, could not anneal into parallel lamellae. However, the majority of the high-R simulations reached a defect-free equilibrium structure consisting of parallel lamellae with PDMS at each surface, and the overall order is improved by increasing the boundary attraction.

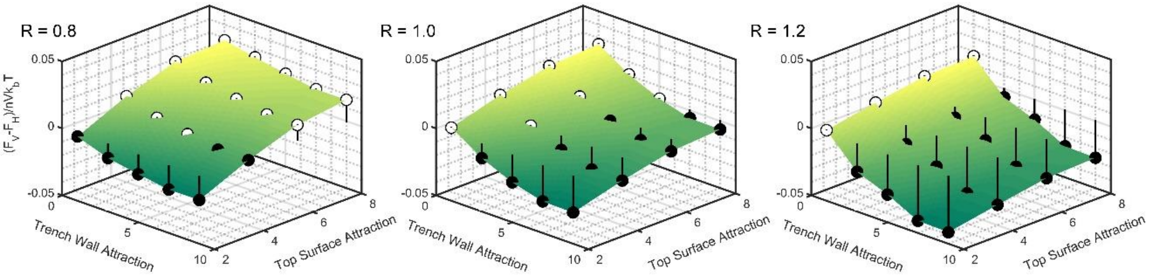

Figure 5.6. Free energy difference between vertical and horizontal lamellae subjected to trench confinement as a function of top surface attraction field and surrounding trench walls, from SCFT. Free energies are evaluated at surface attractions marked by circular markers. Black filled markers have negative free energy difference indicating stable vertical lamellar structure, while white markers are for stable horizontal lamellae. Aspect ratio *R* is indicated for every plot. Figure 5.6 data was provided by Karim Gadelrab and Professor Alfredo Alexander-Katz.

Mixed morphology (blue rectangles) prevails at low trench wall attraction w_{Surr} particularly at $R \sim 1$. The defect patterns demonstrate right angle bends mimicking the confining walls. The right angle bends create interlocked structures that are difficult to anneal. Additional structural characteristics are noticed in SCFT density maps. At low surface attraction strength, periodic short microdomains protrude from the surface towards the bulk of the polymer. These short microdomains become the seeds of a structure that is perpendicular to the surface. The short microdomains can merge to form arches at corners and even on the same surface, generating nonequilibrium defects. On the other hand, increasing surface attraction strength suppresses the extent of short microdomains and creates a uniform wetting layer on the surface. A propagating front from the surface then generates a structure parallel to it. For a defect-free structure surrounded by strong fields on all surfaces, the structure becomes disconnected from the surrounding surfaces as a flat wetting layer encapsulates the polymer domains. A circular cap is observed at both ends of every lamella.[1]

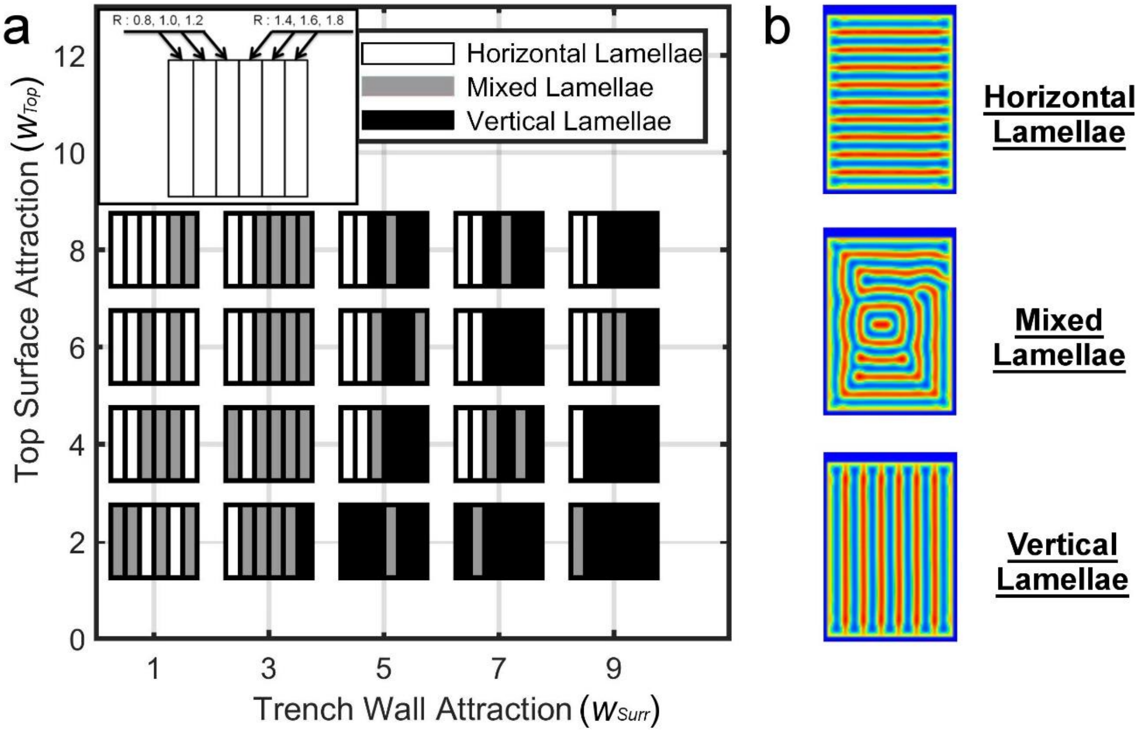

Figure 5.7. SCFT results. (a) Summary of the equilibrium morphology for simulations evolving from random fields ($\chi N = 14, f = 0.5$). Stripes represent different aspect ratios as explained in the top right corner. The walls are attractive to the red block. At a combination of trench wall and top surface attraction fields, three final structures are obtained: Horizontal lamellae, Mixed lamellae, Vertical lamellae. (b) A representation of the final structures that might emerge from SCFT simulations (R = 1.4). Figure 5.7 data was provided by Karim Gadelrab and Professor Alfredo Alexander-Katz.

The formation of mixed orientation lamellae was also observed experimentally. For example, a concentric structure of rectangular tubes was observed after prolonged annealing (24 hr, fig. 5.8a,b) while with the same toluene/heptane solvent anneal condition, a 3-hr anneal resulted in perpendicular lamellae (Fig. 5.2d). This sample had a final thickness of 240 nm, but based on the swelling ratio, this corresponded to a thickness of 400 nm during annealing, similar to the trench width. The transformation of parallel to concentric lamellae is interpreted as a change in the wetting conditions of the confining surfaces, and we employ SCFT to understand the conditions under which such a structure might emerge. A concentric tubular structure was seeded to a SCFT simulation and allowed to evolve under varying surface conditions (see Fig. 5.8b). The free energy of the structure is compared to a fully vertical or a fully horizontal morphology for a given trench aspect ratio R = [0.8, 1.0, 1.2] and surface conditions. In plane lamellae are stable for $R = 0.8$, whereas vertical lamellae are stable for $R = 1.2$.[1] While the free energy difference decreases as the surface fields are increased, the horizontal and vertical structures remain stable even when surface fields are doubled. The case of $R = 1$ on the other hand is particularly interesting. The vertical lamellae remain favorable at high surface fields but the free energy difference between the concentric structure and vertical one practically vanishes at $w_{Top} = 20$ and $w_{Surr} = 19$ reaching a value of ~ $10^{-3} nVk_bT$. The asymptotic behavior of the plot asserts that the concentric structure can only be stable at very high fields, compared to the vertical morphology. This means that for $R = 1$, low surface fields would result in a stable vertical structure that would become degenerate with a concentric structure when surface fields grow in magnitude. This would explain the experimental observation where the slow evaporation of solvent over the 24 hr anneal amplifies the surface fields confining the polymer and generates the concentric structure. In contrast, the shorter anneals are terminated by a rapid deswelling in air which preserves the morphology developed in the swelled state as it collapses in the out-of-plane direction.[33]

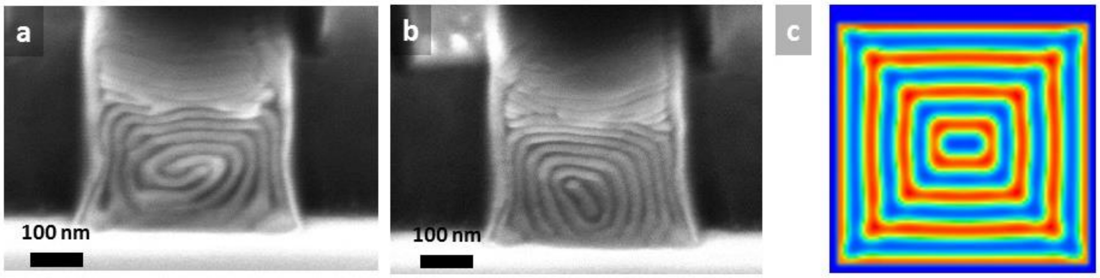

Figure 5.8. Self-assembled concentric BCP nanotubes. (a), (b) Representative SEM of self-assembled concentric structure. SD43 film with thickness 250 nm in a trench with width 400 nm was processed under solvent vapor from 3 ml toluene: heptane 3:1 volumetric mixture for 24 hr. (c) SCFT results of the density map of polymer A ($R = 1$) under confinement. A concentric structure is seeded to the simulation and allowed to evolve under varying boundary conditions. Figure 5.8c data was provided by Karim Gadelrab and Professor Alfredo Alexander-Katz.

5.5 Other templating strategies

5.5.1 Combining Graphoepitaxy and Electric Fields toward Uniaxial Alignment of Solvent-Annealed PS-PDMS BCP

A combination of graphoepitaxy for pattern registration and electric field-induced alignment to enhance the correlation length of the resulting microdomains is envisaged as a promising approach toward the directed self-assembly of BCP. The driving force for the alignment under an electric field is the reduced electrostatic energy of the microdomain interfaces oriented parallel to the electric field vector compared to those oriented perpendicular to the electric field vector.[34] The energy difference between the orientations is proportional to the square of the dielectric contrast $(\Delta\epsilon)^2$ between the blocks of the block copolymer and to the square of the electric field strength E^2. Since the difference in dielectric permittivity between PS and PDMS merely amounts to $\Delta\epsilon = \epsilon_{PS} - \epsilon_{PDMS} \approx 0.17$,[35,36] pure electric field induced alignment is not expected to provide a strong driving force, to promote a defect-free ordering of microdomains. In this work, we used a cylinder-forming PS-PDMS (M_W=53 kg/mol, f_{PDMS}=30%), which was synthesized and provided by Professor Apostolos Avgeropoulos and his group members. More experimental details can be found from Ref. [2].

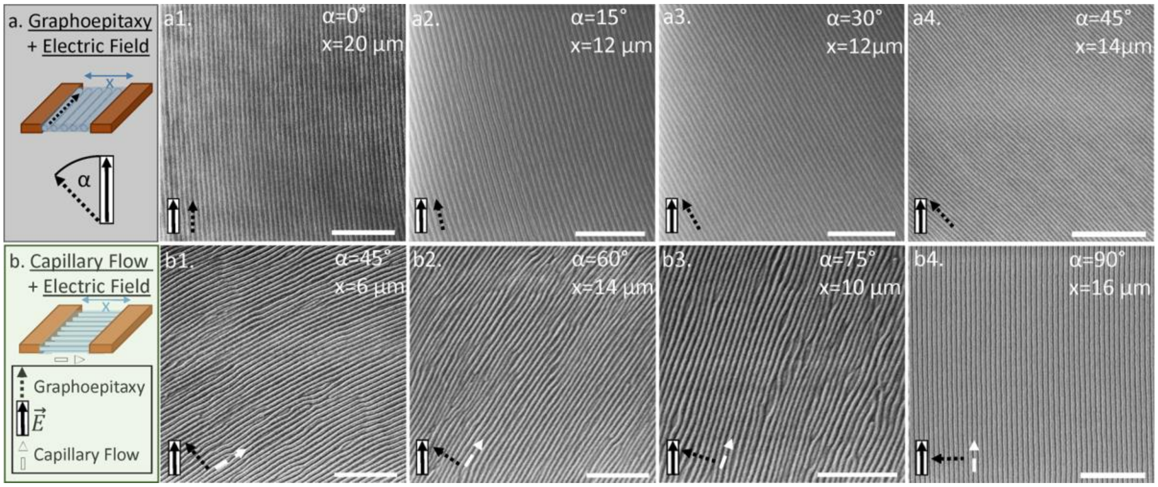

Figure 5.9. He-Ion microscope images of PS-b-PDMS after solvent vapor annealing. The samples were annealed for 4 h in vapor from a 2:1 toluene/heptane mixture at an electric field strength of 12.5 V/µm. α indicates the angle between the electric field vector and the sidewalls, and x is the trench width. The direction in which the BCP is guided due to graphoepitaxy, flow, and electric field are indicated by the black and white arrows as indicated. (a1-a4) Aligned parallel to the topographic features; (b1-b4) cylinders oriented perpendicular to the trench walls. The scale bars display 500 nm. The figure was reproduced from Ref. [2].

In trenched substrates, the preferential wetting of one block of the BCP at the trench sidewall can induce the parallel alignment of the BCP cylinders, while the capillary motion of polymer at the edge of the trench possibly can result in vertical alignment. These two factors produce two opposite results so the directed self-assembly in trenches is highly sensitive to annealing process. To facilitate the uniaxial alignment of the self-assembled cylinders, another external force, the electrical field, was added in order to lock in the alignment and produce long range ordering. Figure 5.9 shows the alignment of the self-assembled cylinders determined by the combining effects from the trench confinement and the electric field. Results have shown that with electric field pointing parallel or perpendicular to the trench, the self-assembled cylinders pointed the same direction with long range ordering.

5.5.1 Selective area control of 3D BCP thin film self-assembly induced by multiple trenches

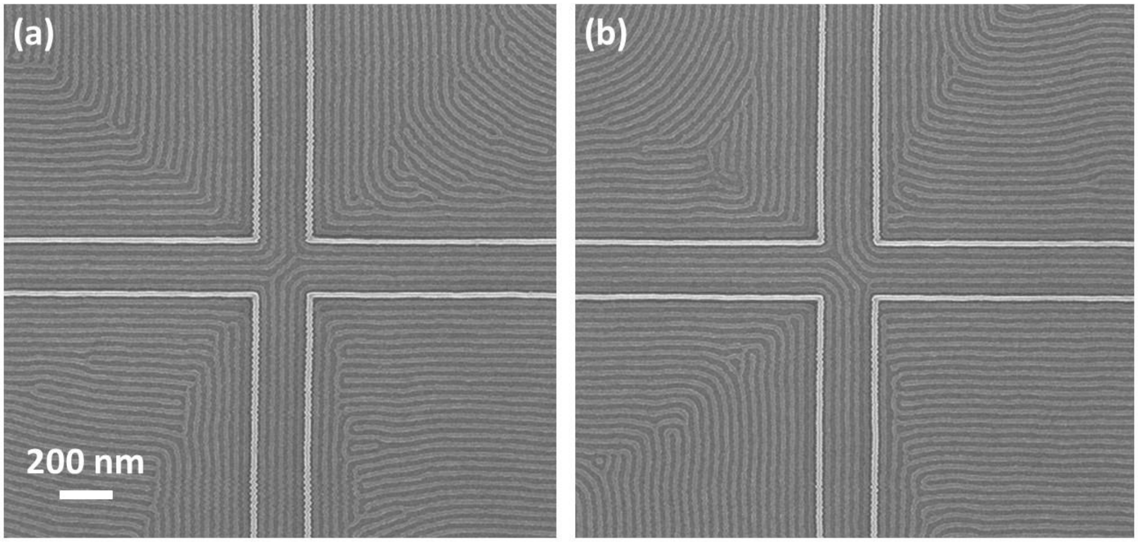

Figure 5.10. Directed Self-assembly of cylinder-forming BCP on cross-shape trenches. (a), (b) self-assembled cylinders were aligned parallel to each trench, but bended 45 degree at the cross region. Sample was processed by solvent vapor annealing with solvent vapor generated from toluene heptane 5:1 volumetric mixture.

Graphoepitaxy is a local effect, in which the commensurability between template dimension and BCP radius of gyration is a key factor for BCP ordering, templating effect become weaker as confinement become wider or the region of BCP was relatively distant from templating feature. However, when multiple confinement effects applied to the region of BCP, competition between those effects is expected to occur to determine the self-assembled orientation. Figure 5.10 demonstrated the competing behavior from the confinement effects of two trenches with orientations orthogonal to each other. In the cross region, the self-assembled cylinders were found to be bended 45 degree to each trenches in response to the two competing confinement effects with equal influence on the cross region.

The influences become asymmetrical when the two orthogonal trenches have different dimensions. As shown in Figure 5.11a, several rods with periodicity 63 nm was positioned perpendicularly inside each wider trenches, and 36-nm thin film of cylinder-forming PS-PDMS with M_W=53 kg/mol, f_{PDMS}=30%, synthesized and provided by Professor Apostolos Avgeropoulos and his group members, was spin cast on the templates from 1% toluene solution at spin speed 4000 rpm. After solvent vapor annealing using solvent vapor generated from toluene: heptane 5:1 volumetric mixture, a monolayer of self-assembled cylinders were synthesized and graphoepitaxy effect was observed. For self-assembled cylinders located right next to the HSQ rods, the orientation of cylinders were strongly rendered by the orientation of HSQ rods. However, for other regions, the self-assembly cylinders still followed the alignment of wide trench. Then a 42-nm thin film was spin cast on the same templates, which produced a double-layer cylindrical structure (Figure 5.11b,c). The bottom-layer cylinders followed the same alignment with the monlayer-layer thin film of Figure 5.11a. Interestingly, upper-layer cylinders were aligned following the orientation of wide trenches, even on the regions where the HSQ rods were, in order to form a localized 3D mesh structure. The mesh structure was induced by the different confinement effect between the bottom layer and the upper layer. For the upper-layer cylinders, the alignment was mostly determined by the hexagonal packing symmetry of the BCP itself, since the height of HSQ template is around 30 nm, which has very little interfacing interaction with upper-layer cylinders during swelling state of solvent vapor annealing.

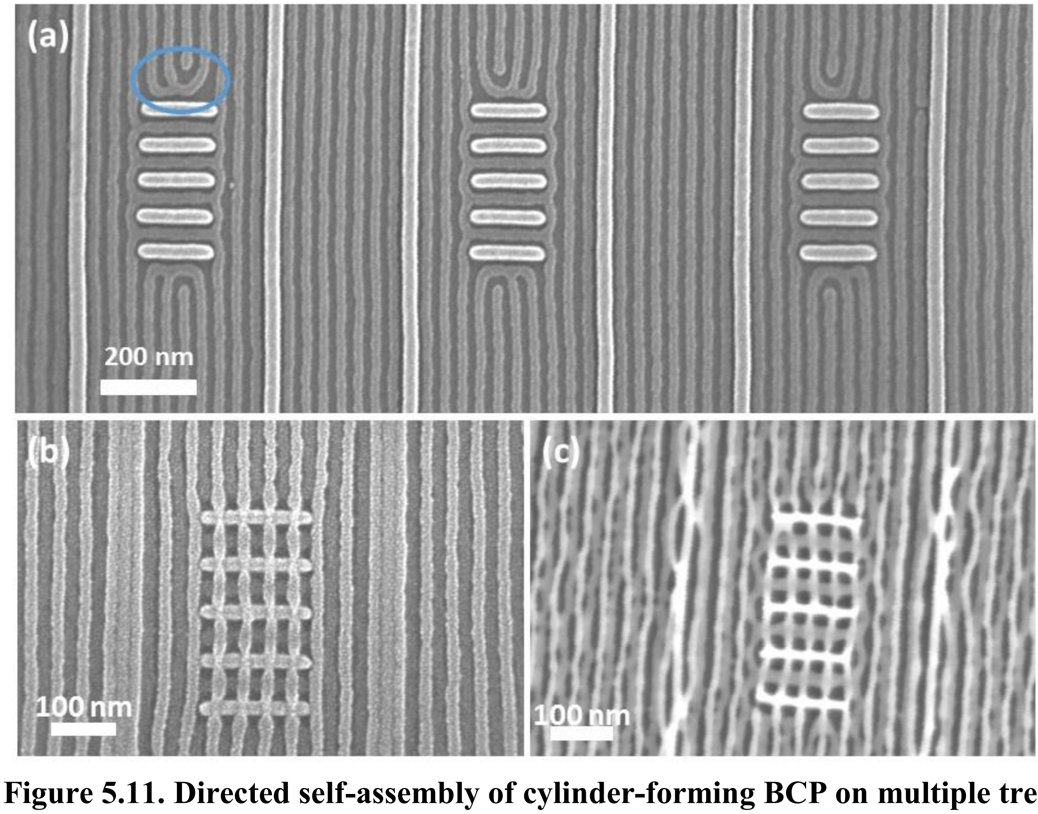

Figure 5.11. Directed self-assembly of cylinder-forming BCP on multiple trenches. (a) monolayer cylinders with 22s Oxygen plasma etching (10 mTorr, 90W); (b) double layer cylinders with 22s Oxygen plasma etching (10 mTorr, 90W); (c) double layer cylinders with 32s Oxygen plasma etching (10 mTorr, 90W).

5.6 Conclusion

To summarize, we have introduced a simple fabrication protocol to create vertically standing lamellar structure from high-χ BCPs within high aspect ratio trenches that guide the self-assembly. The trench aspect ratio R and the surface energy difference between the sidewalls and the top and bottom surfaces were found to determine the lamellar orientation. Through free energy analysis, SCFT simulations were employed to determine the morphological stability under varying confinements and surface attraction strengths. A horizontal lamellar structure prevails at low R even for a low top surface attraction strength, while vertical structures prevail when $R > 1$ for a small trench wall attraction. Ginzburg-Landau free energy analysis further demonstrates the importance of commensurability between film height and natural polymer periodicity. In addition, a concentric tubular structure was fabricated by allowing the lamellae to fuse at top and bottom surfaces. SCFT free energy analysis suggests that the change of surface affinity is responsible for such a structural evolution. The self-assembled perpendicular lamellae are expected to be useful for pattern transfer in nanolithography applications, and can also be functionalized by processes such as sequential filtration synthesis, nanoparticle incorporation, and salt complexation. The development of concentric tubes opens the door to fabricate 3D BCP nanostructures by design of substrate and annealing process. Besides, we also showed that the uniaxial alignment of solvent-annealed PS-PDMS BCP was achieved by combining graphoepitaxy and electric fields. Depending on the graphoepitaxy along, a rule-based design of 3D nanostructure synthesis was realized by the design of the multiple trench dimension and arrangement.

References:

(1) Bai, W.; Gadelrab, K.; Alexander-Katz, A.; Ross, C. A. Perpendicular Block Copolymer Microdomains in High Aspect Ratio Templates. *Nano Lett.* **2015**, *15*, 6901–6908.

(2) Kathrein, C. C.; Bai, W.; Currivan-Incorvia, J. A.; Liontos, G.; Ntetsikas, K.; Avgeropoulos, A.; Böker, A.; Tsarkova, L.; Ross, C. A. Combining Graphoepitaxy and Electric Fields toward Uniaxial Alignment of Solvent-Annealed Polystyrene–B –Poly(dimethylsiloxane) Block Copolymers. *Chem. Mater.* **2015**, *27*, 6890–6898.

(3) Kim, E.; Kim, W.; Lee, K. H.; Ross, C. A.; Son, J. G. A Top Coat with Solvent Annealing Enables Perpendicular Orientation of Sub-10 Nm Microdomains in Si-Containing Block Copolymer Thin Films. *Adv. Funct. Mater.* **2014**, 6981–6988.

(4) Bates, C. M.; Seshimo, T.; Maher, M. J.; Durand, W. J.; Cushen, J. D.; Dean, L. M.; Blachut, G.; Ellison, C. J.; Willson, C. G. Polarity-Switching Top Coats Enable Orientation of Sub-10-Nm Block Copolymer Domains. *Science (80-.).* **2012**, *338*, 775–779.

(5) Han, E.; Stuen, K. O.; Leolukman, M.; Liu, C.-C.; Nealey, P. F.; Gopalan, P. Perpendicular Orientation of Domains in Cylinder-Forming Block Copolymer Thick Films by Controlled Interfacial Interactions. *Macromolecules* **2009**, *42*, 4896–4901.

(6) Verduzco, R.; Li, X.; Pesek, S. L.; Stein, G. E. Structure, Function, Self-Assembly, and Applications of Bottlebrush Copolymers. *Chem. Soc. Rev.* **2015**.

(7) Fenyves, R.; Schmutz, M.; Horner, I. J.; Bright, F. V; Rzayev, J. Aqueous Self-Assembly of Giant Bottlebrush Block Copolymer Surfactants as Shape-Tunable Building Blocks. *J. Am. Chem. Soc.* **2014**, *136*, 7762–7770.

(8) Hong, S. W.; Gu, W.; Huh, J.; Sveinbjornsson, B. R.; Jeong, G.; Grubbs, R. H.; Russell, T. P. On the Self-Assembly of Brush Block Copolymers in Thin Films. *ACS Nano* **2013**, *7*, 9684–9692.

(9) Son, J. G.; Gotrik, K. W.; Ross, C. A. High-Aspect-Ratio Perpendicular Orientation of PS- B -PDMS Thin Films under Solvent Annealing. *ACS Macro Lett.* **2012**, *1*, 1279–1284.

(10) Bodycomb, J.; Funaki, Y.; Kimishima, K.; Hashimoto, T. Single-Grain Lamellar Microdomain from a Diblock Copolymer. *Macromolecules* **1999**, *32*, 2075–2077.

(11) Singh, G.; Yager, K. G.; Berry, B.; Kim, H.-C.; Karim, A. Dynamic Thermal Field-Induced Gradient Soft-Shear for Highly Oriented Block Copolymer Thin Films. *ACS Nano* **2012**, *6*, 10335–10342.

(12) Olszowka, V.; Hund, M.; Kuntermann, V.; Scherdel, S.; Tsarkova, L.; Böker, A. Electric Field Alignment of a Block Copolymer Nanopattern: Direct Observation of the Microscopic Mechanism. *ACS Nano* **2009**, *3*, 1091–1096.

(13) Majewski, P. W.; Gopinadhan, M.; Osuji, C. O. Magnetic Field Alignment of Block Copolymers and Polymer Nanocomposites: Scalable Microstructure Control in Functional Soft Materials. *J. Polym. Sci. Part B Polym. Phys.* **2012**, *50*, 2–8.

(14) Park, S.-M.; Stoykovich, M. P.; Ruiz, R.; Zhang, Y.; Black, C. T.; Nealey, P. F. Directed Assembly of Lamellae- Forming Block Copolymers by Using Chemically and Topographically Patterned Substrates. *Adv. Mater.* **2007**, *19*, 607–611.

(15) Hu, H.; Choo, Y.; Feng, X.; Osuji, C. O. Physical Continuity and Vertical Alignment of Block Copolymer Domains by Kinetically Controlled Electrospray Deposition. *Macromol. Rapid Commun.* **2015**, *36*, 1290–1296.

(16) Xiang, H.; Shin, K.; Kim, T.; Moon, S.; Mccarthy, T. J.; Russell, T. P. The Influence of Confinement and Curvature on the Morphology of Block Copolymers. *J. Polym. Sci. Part B Polym. Phys.* **2005**, *43*, 3377–3383.

(17) Shin, K.; Xiang, H.; Moon, S. I.; Kim, T.; McCarthy, T. J.; Russell, T. P. Curving and Frustrating Flatland. *Science* **2004**, *306*, 76.

(18) Nose, T. Coexistence Curves of Polystyrene/ Poly(dirnethylsiloxane) Blends. *Polymer (Guildf).* **1995**, *36*, 2243–2248.

(19) Kennemur, J. G.; Yao, L.; Bates, F. S.; Hillmyer, M. A. Sub-5 Nm Domains in Ordered Poly(cyclohexylethylene)- Block -Poly(methyl Methacrylate) Block Polymers for Lithography. *Macromolecules* **2014**, *47*, 1411–1418.

(20) Mojarad, N.; Gobrecht, J.; Ekinci, Y. Beyond EUV Lithography: A Comparative Study of Efficient Photoresists' Performance. *Sci. Rep.* **2015**, *5*, 9235.

(21) Chibani, S.; Michel, C.; Delbecq, F.; Pinel, C.; Besson, M. On the Key Role of Hydroxyl Groups in Platinum-Catalysed Alcohol Oxidation in Aqueous Medium. *Catal. Sci. Technol.* **2013**, *3*, 339–350.

(22) Gotrik, K. W.; Hannon, A. F.; Son, J. G.; Keller, B.; Alexander-Katz, A.; Ross, C. A. Morphology Control in Block Copolymer Films Using Mixed Solvent Vapors. *ACS Nano* **2012**, *6*, 8052–8059.

(23) Bai, W.; Hannon, A. F.; Gotrik, K. W.; Choi, H. K.; Aissou, K.; Liontos, G.; Ntetsikas, K.; Alexander-Katz, A.; Avgeropoulos, A.; Ross, C. A. Thin Film Morphologies of Bulk-Gyroid Polystyrene- Block -Polydimethylsiloxane under Solvent Vapor Annealing. *Macromolecules* **2014**, *47*, 6000–6008.

(24) Edwards, E. W.; Montague, M. F.; Solak, H. H.; Hawker, C. J.; Nealey, P. F. Precise Control over Molecular Dimensions of Block-Copolymer Domains Using the Interfacial Energy of Chemically Nanopatterned Substrates. *Adv. Mater.* **2004**, *16*, 1315–1319.

(25) Xu, T.; Hawker, C. J.; Russell, T. P. Interfacial Interaction Dependence of Microdomain Orientation in Diblock Copolymer Thin Films. *Macromolecules* **2005**, *38*, 2802–2805.

(26) Ross, C. A.; Berggren, K. K.; Cheng, J. Y.; Jung, Y. S.; Chang, J.-B. Three-Dimensional Nanofabrication by Block Copolymer Self-Assembly. *Adv. Mater.* **2014**, *26*, 4386–4396.

(27) Stoykovich, M. P.; Müller, M.; Kim, S. O.; Solak, H. H.; Edwards, E. W.; de Pablo, J. J.; Nealey, P. F. Directed Assembly of Block Copolymer Blends into Nonregular Device-Oriented Structures. *Science (80-.).* **2005**, *308*, 1442–1446.

(28) Chaudhury, M. K. Interfacial Interaction between Low-Energy Surfaces. *Mater. Sci. Eng. R Reports* **1996**, *16*, 97–159.

(29) Kobayashi, H.; Owen, M. J. Surface Tension of Liquid Polysiloxanes Having Fluorinated Alkyl Side-chains. *Die Makromol. Chemie* **1993**, *194*, 1785–1792.

(30) Paik, M. Y.; Bosworth, J. K.; Smilges, D.-M.; Schwartz, E. L.; Andre, X.; Ober, C. K. Reversible Morphology Control in Block Copolymer Films via Solvent Vapor Processing: An In Situ GISAXS Study. *Macromolecules* **2010**, *43*, 4253–4260.

(31) Di, Z.; Posselt, D.; Smilgies, D.-M.; Papadakis, C. M. Structural Rearrangements in a Lamellar Diblock Copolymer Thin Film during Treatment with Saturated

Solvent Vapor. *Macromolecules* **2010**, *43,* 418–427.

(32) Hansen, C. M. *Hansen Solubility Parameters: A User's Handbook, Second Edition*; CRC Press, 2007; Vol. 2.

(33) Gu, X.; Gunkel, I.; Hexemer, A.; Gu, W.; Russell, T. P. An in Situ Grazing Incidence X-Ray Scattering Study of Block Copolymer Thin Films during Solvent Vapor Annealing. *Adv. Mater.* **2014**, *26*, 273–281.

(34) Schoberth, H. G.; Pester, C. W.; Ruppel, M.; Urban, V. S.; Böker, A. Orientation-Dependent Order–Disorder Transition of Block Copolymer Lamellae in Electric Fields. *ACS Macro Lett.* **2013**, *2*, 469–473.

(35) Kathrein, C. C.; Kipnusu, W. K.; Kremer, F.; Böker, A. Birefringence Analysis of the Effect of Electric Fields on the Order–Disorder Transition Temperature of Lamellae Forming Block Copolymers. *Macromolecules* **2015**, *48*, 3354–3359.

(36) Tsori, Y. Colloquium : Phase Transitions in Polymers and Liquids in Electric Fields. *Rev. Mod. Phys.* **2009**, *81*, 1471–1494.

Chapter 6: Conclusions and Future Works

6.1 Conclusions

Self-assembly is an elegant process for nanostructure fabrication, and block copolymers provide a great model to study self-assembly, a promising material in engineering nanotechnology, and a possible solution to answer today's or future nanofabrication challenges. This thesis started from a study of the thin film morphology control of a specific Si-containing block copolymer, PS-PDMS, with a bulk morphology consisting of a gyroid. Its high etch resistance and etch selectivity are attractive in applications such as nanolithography and sensors. The high Flory-Huggins interaction parameter between the PS block and PDMS block promotes a sharp interfacial dividing surface and, the formation of feature sizes below 10 nm. Its thin film morphologies include hexagonal packed perforated lamellae, cylinders, lamellar and spheres depending on the control of solvent annealing conditions and film thickness in both as-cast and swelled state. The selective solvent mixture (toluene and heptane) used in solvent vapor annealing is able to tune the effective volume fraction of the self-assembled system and kinetically trap the self-assembled BCP morphology in which toluene and heptane ratio, as-cast film thickness, swelling film thickness are key factors to obtain well-ordered morphology. A universal block copolymer pattern transfer method was demonstrated to produce Co nanostructures consisting of arrays of lines or dots from the gyroid-forming PS-PDMS.

We used synchrotron Grazing Incidence Small Angle X-ray Scattering (GISAXS) to observe the self-assembly in situ during solvent vapor annealing. In this specific solvent vapor annealing process, solvent absorption facilitates out-of-plane microdomain orientation, while surface interactions favor in-plane microdomain orientation. Microdomain orientation behavior in thin films is dominated by surface interaction, while in thick films solvent interaction is dominant factor. Therefore microdomain orientation can be engineered by tuning the annealing conditions (solvents, time, temperature, etc) and film thickness.

Lastly we applied several templating strategies to the PS-PDMS system to program its self-assembly including electric field, trenched substrates and e-beam-fabricated posts or lines. A high aspect-ratio trench substrate was fabricated to increase the influence from the interface of trench sidewall. To optimize the orientation control, an inert metal (here, platinum) was deposited on the base of the trench, making PDMS brush preferentially bonded to the sidewall in order to make the sidewall much more preferential to PDMS block than the base of the trench. This led to perpendicular lamellar formation throughout the film, propagating from trench sidewall. In the high aspect-ratio templating system, the competition between interfacial interactions of sidewall and bottom surface was utilized to control the orientation of self-assembled microdomains, especially to enable the formation of perpendicular-oriented lamellae, which is essential in pattern transfer and other lithographical applications. This method is universal for general BCP systems, and more suitable for BCPs with extremely high interaction parameter, which is a key parameter to make extremely small features. The experimental findings are consistent with results of self-consistent mean field simulation. It enabled the possibility of a range of device fabrication such as sensors, filtration memory, magnetic storage media, and photonic crystal.

6.2 Future works

A study of diblock copolymer self-assembly is a great model towards understanding the beauty of natural self-assembly. I imagine in the future “machines” can be “grown” instead of “built”.

Within the field of block copolymer self-assembly, many challenges still remain to be studied. These include:

1) A lack of fundamental understanding of the BCP self-assembly mechanisms that are associated with specific processing. Examples are solvent vapor annealing where additional components (solvents) are included in the system, and the process follows a nonequilibrium kinetic path; incorporation of nanoparticles and other nanostructures; and shear annealing where shear introduces residual strain into the BCP that influences subsequent BCP self-assembly. These require in situ observation methods such as Grazing Incidence Small Angle X-ray Scattering (GISAXS),[1] and Atomic Force Microscope,[2] etc, to track the progress of the BCP self-assembly in response to solvent vapor, laser beam, shear, or thermal treatment, etc. For solvent vapor annealing, solvent vapor is absorbed by the BCP film from top air/film interface, in which self-assembly is dramatically enhanced first and propagate towards the bottom of the film. It is interesting to study the depth profile of self-assembly using in situ GISAXS with varying incident angle in response to choice of solvent and its partial vapor pressure.

2) The ability to precisely control self-assembly to make 3-dimensional structures. Most directed self-assembly processes can be controlled well on planar substrates, but the precise registration of BCP self-assembly along the perpendicular direction is still challenging in terms of both fabrication and characterization. For graphoepitaxy, if complexity increases in z-direction of the templates, making uniform BCP film or filing BCP into templates would be challenging. However, imprinting technique is able to allow making a uniform BCP film first, and then templates come from top to provide additional interfacial interactions that affect the self-assembly behavior. The proposed experiments includes the traditional graphoepitaxy that uses a templated substrate with aspect ratio of template below certain degree in order to make sure a uniform BCP film can form on top, and an imprint mold also with certain degree of aspect ratio to confine BCP film from top. Therefore 3-dimensional self-assembled nanostructure can be controlled from both sides: top surface and bottom substrate. While demolding process is challenging to maintain a uniform film, back etching or UV curing can be utilized to improve the demolding process.

3) Defectivity of the self-assembled morphology still requires further work, in particular how to eliminate metastable defects. Novel annealing processes still remain to be found. One proposed experiment is to combine solvent vapor annealing and polymerization in order to obtain more controllability of the final self-assembled morphology from a given BCP. In this experiment, a thermal or UV crosslinkable solvent is used in the solvent vapor annealing. As a certain amount of crosslinkable solvent absorbed by the BCP film while the whole solvent/BCP system are still within the strong segregation limit regime, the solvent is expected to have asymmetric distribution between microdomains of each block. While at the swelling state, thermal treatment or UV irradiation is applied to induce the polymerization of solvent itself and/or solvent with BCP, the self-assembled morphology at swelling state is trapped through crosslinking. Therefore, solvent-drying induced structure collapse, high aspect-ratio swelling feature, or certain chemistry from solvents can be effective preserved through the polymerizing solvent vapor annealing.

4) Novel molecular architectures or compositions are needed to realize greater control over the self-assembled morphology and functionality. Experiments such as the thin film morphology of a (AB:CD, AA:BB, or AB:AB, etc) Tetrablock bottlebrush copolymer are interesting to explore (A, B, C, and D represents chemically distinct sidechains). The disentanglement of the brush sidechains may result in a fast annealing of the high molecular weight BCP, preferential ordering or orientation due to its high entropy penalty to folding brush sidechains.

List of Publications

1. **Wubin Bai**, Kevin G. Yager, Caroline A. Ross, "In Situ GISAXS Study on a Si-containing block copolymer under solvent vapor annealing: effects of molecular weight and selective solvents mixture ratio", in preparation, 2016

2. Keehong Lee, Melissa Kreider, **Wubin Bai**, Melissa Kreider, Li-Chen Cheng, Kun-Hua Tu, Tao Huang, Ntetsikas Konstantinos, George Liontos, Apostolos Avgeropoulos, Caroline Ross, "Nanochannels fabricated by self-assembly of Polystyrene-block-Polydimethysiloxane block copolymer", submitted, 2016.

3. Christine C. Kathrein, **Wubin Bai**, Jessica Gwyther, Ian Manners, Alexander Boker, Larisa Tsarkova, and Caroline Ross, "Electric Field induced Phasetransitions in Iron Containing 3-Miktoarm Star Terpolymers", submitted, 2016

4. **Wubin Bai,** Caroline Ross, "Functional Nanostructured Materials Based on Self-assembly of Block Copolymers", MRS Bulletin, 2016, Vol. 41 Issue 02

5. **Wubin Bai,** Karim Gadelrab, Alfredo Alexander-Katz, Caroline Ross, " Perpendicular Block Copolymer Microdomains in High Aspect-Ratio Templates", Nano Letters, 2015, 15 (10), pp 6901–6908

6. **Wubin Bai**, Kevin Yager, Caroline Ross, " In Situ Real-time Characterization of PS-PDMS block copolymer self-assembly during solvent vapor annealing", Macromolecule, 2015, Accepted.

7. Christine C. Kathrein, **Wubin Bai**, Jean Anne Currivan Incorvia, George Liontos, Konstantinos Ntetsikas, Apostolos Avgeropoulos, Alexander Böker, Larisa Tsarkova, and Caroline A. Ross, "Combining Graphoepitaxy and Electric Fields towards Uniaxial Alignment of Solvent-annealed Poly(styrene)-b-Poly(dimethylsiloxane) Block Copolymer", Chemistry of Materials, 2015, 27 (19), pp 6890–6898

8. Kun-Hua Tu, **Wubin Bai**, George Liontos, Konstantinos Ntetsikas, Apostolos Avgeropoulos, Caroline Ross, "Universal Pattern Transfer Methods for Metal Nanostructures by Block Copolymer Lithography", Nanotechnology, 2015.

9. Saman Safari Dinachali, **Wubin Bai**, Kun-Hua Tu, Hong Kyoon, Choi, Jinshuo Zhang, Melissa Kreider, Li-Chen Cheng, Caroline Ross, "Thermo-Solvent Annealing of Polystyrene-Polydimethylsiloxane Block Copolymer Thin Films", ACS Macro Lett., 2015, 4, pp 500–504.

10. Adam F. Hannon, **Wubin Bai**, Alfredo Alexander-Katz and Caroline A. Ross, " Simulation Methods for Solvent Vapor Annealing of Block Copolymer Thin Films", Soft Matter, 2015, DOI: 10.1039/C5SM00324E

11. Kevin Gotrik, Thomas Lam, Adam Hannon, **Wubin Bai**, Yi Ding, Jonathan Winterstein, Alfredo Alexander-Katz, J. Alexander Liddle, Caroline Ross, "3D TEM Tomography of Templated Bilayer Films of Block Copolymers", Advanced Functional Materials, 2014, DOI: 10.1002/adfm.201402457

12. **Wubin Bai**, Adam Hannon, Kevin Gotrik, Hong Kyoon Choi, Karim Aissou, George Liontos, Konstantinos Ntetsikas, Alfredo Alexander-Katz, Apostolos Avgeropoulos, Caroline A. Ross, "Thin Film Morphology of Bulk-Gyroid Polystyrene-block-polydimethylsiloxane under Solvent Vapor Annealing", Macromolecules, 2014, 47 (17), pp 6000–6008

13. Adam Hannon, Yi Ding, **Wubin Bai**, Caroline Ross, Alfredo Alexander-Katz, "Optimizing Topographical Templates for Directed Self-Assembly of Block Copolymer via Inverse Design Simulations", Nano Lett., 2014, 14 (1), pp 318–325

14. Caroline Ross, Kevin Gotrik, Hong Kyoon Choi, Karim Aissou, Adam Hannon and **Wubin Bai**, " Self-assembling polymer patterns could shrink lithographic limits", SPIE Newsroom, 30, January 2013

15. **Wubin Bai**, Yen-Chih Lin, Tzon-Kun Hou, and Tzay-Ming, Hong, "Scaling Relation for a compact crumpled thin sheet", Phys. Rev. E. 82.066112 (2010)